FAULT ANALYSIS AND CONTROL OF DFIGS FOR GRID CODE COMPLIANCE AND PROTECTION OF POWER SYSTEM

HASSAN MOHAMMADPOUR

A DISSERTATION SUBMITTED TO
THE FACULTY OF GRADUATE STUDIES
IN PARTIAL FULFILMENT OF THE REQUIREMENTS
FOR THE DEGREE OF
DOCTOR OF PHILOSOPHY

GRADUATE PROGRAM IN
ELECTRICAL ENGINEERING AND COMPUTER SCIENCE
YORK UNIVERSITY
TORONTO, ONTARIO

July 2022

© Hassan Mohammadpour, 2022

Abstract

Inverter-based resources (IBRs) are growing at exponential rates in today's power systems. Therefore, a sizable portion of the measurements of relays is expected to come from IBRs. However, the fault current characteristics of IBRs put the operation of the relays in jeopardy as they are different than that of synchronous generators' (SGs) based on which the relays' operating principles are developed. Therefore, different countries have progressively revised their grid codes (GCs) to reduce the likelihood of protection malfunctions and ensure stable and continuous operation of power systems.

Similar to emerging regional GCs, the recently approved IEEE 2800 Standard mandates that IBRs generate negative-sequence current during low-voltage ride-through (LVRT) conditions. The 2800 Standard requires that the IBRs' negative-sequence current lead the negative-sequence voltage by 90°–100° to emulate SGs and reduce the likelihood of protection malfunction. However, the limitations of existing doubly-fed induction generators (DFIGs) led the Standard to exempt the DFIGs from this requirement and allow a wider range for their negative-sequence current angle. Meanwhile, the 2800 Standard also acknowledged that this exemption had unidentified and potentially negative impacts on protective relays. This dissertation, for the first time, (i) sheds light on several so-far-unknown DFIG characteristics that impact the angle of the negative-sequence current during LVRT, (ii) reveals the impacts of the above DFIG exemption on industrial relays, and (iii) develops a solution to prevent the need for this exemption in the future revisions of the IEEE 2800 Standard.

This dissertation also investigates the challenges brought about by the DFIGs during the crowbar

connection and rectification mode of operation, i.e., interrupted control of the DFIG's converters, now affecting the performance of distance relays that are installed at a DFIG-based wind farm substation. The focus is on the relays implemented using the apparent impedance approach and the commercially developed reactance method. It is revealed that the phase elements of a distance relay that uses these methods are prone to under-/over-reach in the systems with DFIGs. The exclusive fault behavior of DFIGs along with different units of a distance relay is scrutinized to identify the root causes. To address the relay problems, a communication-assisted method with minimal bandwidth requirement is developed, which provides non-delayed fast tripping over the entire length of the line.

To all eternal companions in the journey of my life.

Acknowledgements

I would like to express my sincere gratitude to my supervisor Dr. Ali Hooshyar, for his guidance throughout the process of my research. It has been an honor to work under him the last few years. He taught me how think out-of-box while having an acute attention to details, and how to combine science with industry. This endeavor would not have been possible without his invaluable guidance, encouragement and strong technical insights.

I am honored that this dissertation has been examined by Dr. Amirnaser Yazdani, Dr. Afshin Rezaei-Zare, Dr. John Lam, and Dr. Baoxin Hu. I would like to express my gratitude for taking the time to review my dissertation and provide valuable feedback.

I would like to thank my office-mates at York University for their help and companionship throughout the course of this work. I am also grateful for my fellows at the Centre for Applied Power Electronics (CAPE) at the ECE department of the University of Toronto for many productive discussions during my visit over the past few years. Special thanks to Dr. Amin Banaiemoqadam who provided me with his priceless help and expertise for the work presented in this dissertation.

Special thanks go to my friend, soon-to-be Dr. Abolfazl Seifi, for his dedicated presence and help in the most needed times.

I would like to thank all of my family members and friends, who supported me through out this work. I am deeply indebted to my brother Dr. Ali Mohammadpour for his continuous encouragement and dedicated support that gave me enough confidence to start this journey and end it today.

Words cannot express my gratitude to the special person of my life, Macy, who stood by my side in difficult times and helped me stay positive and strong throughout the course of this work.

Contents

List of Tables

List of Figures

Abbreviations

IBR Inverter-based Resource

RES Renewable Energy Source

PV Photovoltaic

DFIG Doubly-Fed Induction Generator

WF Wind Farm

WT Wind Turbine

WRIG Wound Rotor Induction Generator

LVRT Low-Voltage Ride-Through

GC Grid Code

POC Point of Connection

POM Point of Measurement

RSC Rotor Side Converter

GSC Grid Side Converter

SCIGs Squirrel-Cage Induction Generator

ETP Electromagnetic Torque Pulsation

CVC Conventional Vector Control

DCC Dual Current Control

SG Synchronous Generator

PWM Pulse Width Modulation

HV High Voltage

LV Low Voltage

PF Power Factor

PMU Phasor Measurements Unit

AG Phase-A-to-Ground

IF Instantaneous Frequency

BCG Phase-B-to-Phase-C-to-Ground

SLG Single-Line-to-Ground

LLG Line-to-Line-to-ground

LL Line-to-Line

DD Disturbance Detector

FDI Fault Direction Identification

Chapter 1

Introduction

The determination to reduced burning of fossil fuels in electric power stations due to the green house gases has led to increasing share of renewable sources in the global electric market. According to international renewable energy agency (IRENA) report, renewable resources constitute 38% of global installed capacity by the end of 2021 [10]. Renewable inverter based resources (IBRs), such as solar and wind, are the fastest growing types of renewable resources as they participated in an unprecedented 88% of global renewable additions in 2021 [10].

Doubly fed induction generator (DFIG)-based wind turbines (WTs) constitute a significant share of IBRs. While other types of IBRs have the similar fault behaviour owing to interface similarities, DFIGs possess unique fault current characteristics due to deployment of a wound rotor induction generator (WRIG), crowbar and chopper circuits, and partially rated back-to-back power electronics converters in their structure. The unique structure, limitations, and complexity of the DFIG control sometimes resulted in exceptions and/or different definitions of low voltage

ride-through requirements (LVRT) for DFIGs mandated by grid codes (GCs). For example, various GCs, such as [11], exempt the DFIG from regulating negative-sequence current during LVRT.

Another example is the recently approved IEEE 2800 Standard that mandates the IBRs' negative-sequence current lead the negative-sequence voltage by 90°–100° to emulate synchronous generators (SGs) and reduce the likelihood of protection malfunction [12]. However, the limitations of existing DFIGs led the Standard to exempt them from this requirement and allow a wider range for their negative-sequence current angle. Meanwhile, the 2800 Standard also acknowledged that this exemption had unidentified and potentially negative impacts on protective relays. Therefore, it is critical to comprehensively investigate the operation and control of DFIGs during LVRT to identify the reason for large deviation of the angle between the negative-sequence current and voltage from 90°–100° as well as reveal the impacts of the above exemption on protective relays. Such study not only helps protection engineers to design new protection schemes for DFIGs, but it also gives an insight to control engineers to come up with new control schemes to eliminate the need for the exemptions made for DFIGs.

The DFIGs' unique structure and control during LVRT introduces some other challenges to the protective relays that protect their tie-line, especially distance relays. Distance relays are used as the main and backup protection in transmission lines, and are considered as the backbone of transmission line protection [13]. Distance relays are designed assuming that SGs are the only generating units, where the fault signals and sequence circuits have their characteristics. Such assumption makes these relays prone to maloperation in the presence of DFIGs, especially during the crowbar connection or rectification mode of operation. Therefore, it is important to study

the fault behaviour of DFIGs to realize their differences with that of SGs, and analyze distance relays behaviour protecting their tie-line. Such a study would help protection engineers to design a tailor-made protection for DFIGs.

The following defines the problems and reviews the existing solutions with the LVRT and distance relaying of DFIGs.

1.1 Problem Statement

Due to the rapid growth of IBRs, such as solar photovoltaic (PV), Type III WTs or DFIG-based WTs, and Type IV WTs, they have become an important part of today's power systems. Non-negligible portion of power generation from IBRs has led different countries to progressively revise their GCs to ensure the stable and reliable operation of power systems. One of the main and basic requirements of the GCs is that the IBRs have to remain connected to the utility grid during grid faults or low voltage events—known as LVRT requirement. For example, Fig. 1.1 shows the LVRT requirements of the VDE GC for IBRs [2]. In this figure, V_{pm}^{+} is the positive-sequence line-to-line voltage at the point of measurement (POM). According to this GC, the IBRs must stay connected to the network as long as V_{pm}^{+} is above the limit curves represented in Fig. 1.1. In addition to the mandate for remaining connected to the grid, modern GCs, such as [2] and [11], also require that IBRs generate positive- and negative-sequence reactive currents at the point of connection (POC). A common approach to determine the magnitude of sequence currents at the POC is to use the K-factor diagram of [2]. In this method, the incremental positive- and negative-sequence reactive currents at the POC, $\Delta I_{Q,\mathrm{pc}}^{\pm}$, are determined based on the respective incremental sequence voltages, $\Delta V_{\mathrm{pc}}^{\pm}$, using

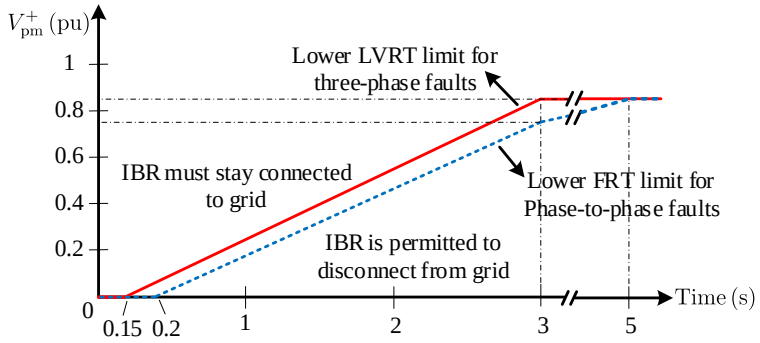

Figure 1.1: LVRT limit curve at the POM for IBRs.

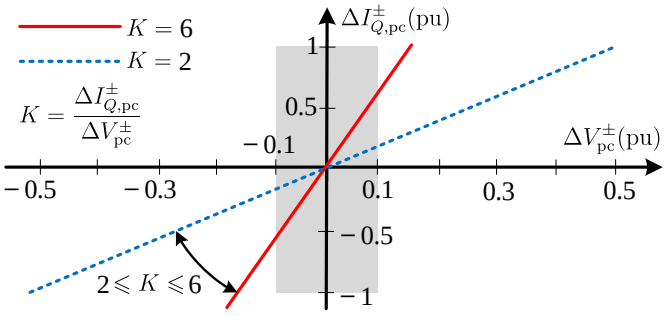

Figure 1.2: Reactive current requirements of the VDE GC for IBRs during LVRT [2].

the diagram in Fig. 1.2. The recently approved IEEE 2800 Standard additionally requires that the IBRs' negative-sequence current lead the negative-sequence voltage by 90°–100° to emulate synchronous generators and reduce the likelihood of protection malfunction. Such an angle imitates the negative-sequence current angle of synchronous generators and decreases the probability of malfunction of protective relays—which rely on the negative-sequence components for various functions [14].

While the PV and Type IV WTs have similar control systems and fault current characteristics owing to the interface similarities, DFIGs possess unique fault current characteristics and complicated control system due to deployment of a WRIG, partially rated back-to-back power electronics converters, namely the rotor side converter (RSC) and the grid side converter (GSC), and limitations

of the DFIG structure. Optimizing the control of the RSC with the aim of addressing reactive current requirements of GCs and keeping the angle between the negative-sequence current and voltage within 90°–100°, as required by IEEE 2800 Standard, makes the control structure of the DFIG complicated further. The complicated control structure and limitations of existing DFIGs led the IEEE 2800 Standard to exempt the DFIGs from having a 90°–100° angle between the negative-sequence current and voltage and allow a wider range. With the 2800 Standard exemption, DFIGs are permitted to have a phase difference within the [90°, 150°] range between the negative-sequence current and voltage during LVRT. Meanwhile, the 2800 Standard acknowledged that this exemption had unidentified and potentially negative impacts on protective relays. The lack of clarity about the impacts of this DFIG exemption on protection systems will cause uncertainty about the operation of relays in the proximity of DFIG-based wind plants. Therefore, the 2800 Standard calls for the protection engineers to investigate the impacts of the specific angle range of [90°, 150°] on protective relays. It also requests to consider specifying a more precise control of the angle if it is not acceptable for proper operation of the protective relays.

Based on engineering judgement, protection functions dependent on negative sequence quantities may be negatively impacted by the wide range of the angle between the negative-sequence current and voltage. For example, protective relays include faulty phase selection elements for various functions, e.g., using the correct distance element and single-pole tripping [15]. Fig. 1.3 illustrates the operating principle of the widely used current angle-based phase selection method. This method uses the angle difference between the negative- and positive-sequence currents, i.e. $\delta^+ = \measuredangle I^- - \measuredangle I^+$, and the angle between the negative- and zero-sequence currents, i.e. $\delta^0 = \measuredangle I^- - \measuredangle I^0$, to identify

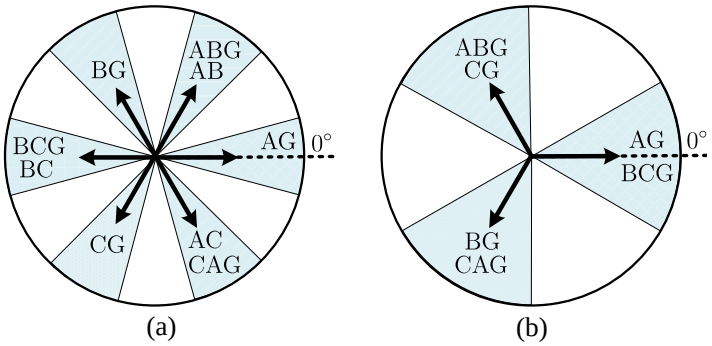

Figure 1.3: Fault type zones for (a) δ^+, (b) δ^0 [3].

the fault type [3]. Superscripts $+$, $-$, and 0 denote the positive-, negative-, and zero-sequence components. This method identifies a certain fault type when δ^+ and δ^0 fall in the respective zones of that fault type in Fig. 1.3. Each zone of δ^+ and δ^0 for a fault type are normally $\pm 30^\circ$ and $\pm 60^\circ$, respectively. The zones shown for δ^0 and δ^- in Fig. 1.3 are derived based on the negative- and zero-sequence equivalent circuits of synchronous generators (SGs). Since each of these circuits consists of a single highly inductive impedance, the angle between the negative-sequence current and voltage, $\alpha^- = \measuredangle(I^-/V^-)$, and the angle between the zero-sequence current and voltage, $\alpha^0 = \measuredangle(I^0/V^0)$, at the relay location are both around 90° to 100°. For IBRs, α^0 is impacted only by the impedance of the interface transformer, and so it follows the same pattern. However, the impact of different DFIG control schemes and wide range of [90°, 150°] between the negative-sequence current and voltage during LVRT on α^- needs to be investigated.

The specific features of the DFIG mentioned earlier in this section creates more problems to the protective relays, especially distance relays. The partially rated converters makes DFIGs susceptible to the voltage dips caused by grid faults. An abrupt voltage dip in the DFIG terminals causes overcurrents in the rotor winding and overvoltages in the dc-link capacitor. Therefore, if no countermeasure is taken, the overcurrents and overvoltages can damage the RSC and the dc-link

capacitor [16], causing WT tripping and failing to comply with the LVRT requirements mentioned earlier. In practice, DFIGs are equipped with a crowbar and/or a braking chopper that protects the RSC and the dc-link capacitor from overcurrents and overvoltages [17–19]. A crowbar shorts the rotor winding through some resistors and so limits the overcurrents in the rotor circuit. The crowbar is deactivated in a few cycles and the control of the converters is resumed to full-fill the GC reactive current requirements. Although the crowbar effectively protects and enhances LVRT capability of the DFIGs, its operation converts the DFIGs to squirrel-cage induction generators (SCIGs) with unique fault current characteristics that can cause misoperation of the distance relays that protect their tie-lines [20].

Through closed-form solutions, [21] and [22] show that an off-nominal frequency component, whose frequency is similar to the mechanical speed of the rotor, ω_m, appears in the SCIG's fault current and decays over time. The off-nominal frequency depends on the slip of the machine. As SCIGs work with a small slip, the off-nominal frequency is very close to the power system's rated frequency. However, since the DFIG slip varies in the range of $\pm 30\%$, ω_m adds a frequency component in the range of 42$\sim$78 Hz to the fault current of a DFIG in a 60 Hz system [20, 23]. Several closed-form solutions for the fault current of the DFIG during the crowbar connection is derived in the literature that verifies the existence of the off-nominal frequency component in the DFIG fault currents [22–25]. It is unveiled in [20] that the DFIGs's off-nominal frequency components during balanced faults can cause misoperation of the distance relays that protect their tie-lines.

1.2 Existing Solutions

Multiple studies have developed control schemes for the positive- and/or negative-sequence current of DFIGs. An optimized reactive power flow of the DFIG converters is proposed in [26]. The proposed method in [27] attempts to reduce the stator and rotor currants as well as the rotor voltage, allowing the generator to ride-through the grid disturbances and inject reactive current during grid faults. However, this method needs a series voltage compensation to be added to the structure of the existing DFIGs, which makes it costly. A comprehensive control strategy to enhance the LVRT and reactive power support capability of the DFIG by installing the energy storage system (ESS) in parallel with the dc-link capacitor is proposed in [28]. Nevertheless, the ESS adds complexity and cost to the DFIG control and structure. An online dynamic coordination control strategy for DFIG converters considering the RSC and GSC limits to comply with GCs is proposed in [29]. A dynamic coordinated control strategy to enhance the reactive power capability of DFIGs is presented in [30]. An adaptive reactive current control scheme for both the RSC and the grid side converter (GSC) is proposed in [31]. However, these studies do not consider compliance with the negative-sequence current requirements of the 2800 standard or GCs. A coordinated control of the RSC and the GSC is proposed in [32] to meet the GCs. However, this study achieves a 90° phase difference between the negative-sequence current and voltage of the GSC, not the negative-sequence current and voltage at the DFIG's terminal, where compliance with the 2800 standard and GCs is checked. Another control method for the RSC and GSC is proposed in [33] to comply with the positive-and negative-sequence current requirements of GCs. The method proposed in [33] meets the GCs'

reactive current requirement. However, this method does not suppress the electromagnetic torque pulsations (ETPs) of the DFIG.

Several studies have been reported on the effect of DFIGs on negative-sequence quantity-based protection functions, and some solutions are proposed in the literature. The fault current of DCC-based DFIGs is investigated through realistic case studies in [34]. The case studies show that during LVRT of DFIGs the angle between the negative-sequence current and voltage at the DFIG terminal is not fixed and keeps changing. It is shown that this unconventional angle can result in maloperation of negative-sequence current-based protection relays. On this basis, the author suggests that the relays operate based on the zero-sequence quantities of the fault current as they are not affected by the WF. However, the results suffer from an analytical study, and the operation of the protection system during phase faults is neglected. It is unveiled in [35] that IBRs can hinder correct operation of negative-sequence quantity-based protection elements. The conclusions made in this paper are based on the assumption that DFIGs are controlled based on traditional vector control, i.e., CVC scheme. Most of the existing papers assess the effect of DFIGs on negative-sequence quantity-based protection functions through simulation analysis. However, understanding the reasons behind maloperation of negative-sequence quantity-based protection elements in the presence of DFIGs needs a more detailed analysis.

To address the misoperation of the phase-selection element in the presence of IBRs, several publications propose voltage-dependent phase selection methods [36–39]. For example, the method in [36] operates based on the voltage magnitudes and distinctive zones for the phase difference between the fault sequence voltages. However, voltage-dependent phase selection methods require

several changes to the algorithms implemented by currently installed relays. In addition, these methods cannot be used during severe faults where the magnitude of the voltage is low and voltage measurements are not reliable.

There are only a handful of publications addressing the misoperation of distance relays protecting the lines connected to DFIGs. An adaptive distance relay setting is proposed in [40], considering the effect of the operating points of DFIGs and the number of WTs at the instant of the fault. However, the WTs are modeled as voltage sources in the same way that conventional SGs are modeled. Such modeling is not precise for relaying purposes. Another adaptive approach considering the effect of the crowbar on the relay operation is proposed in [41]. Nevertheless, the effect of the DFIGs off-nominal frequency components on the relay behavior is neglected. One study investigates the effects of the DFIG off-nominal frequency component on distance relays during balanced faults and the crowbar connection [20]. It is demonstrated in [20] that the off-nominal frequency component of the fault current results in rotation of the measured impedance in the impedance plane of a distance relay. The maloperation of distance relays is alleviated using a modified permissive over-reaching transfer trip (POTT). However, this study only considers the passive crowbar, i.e., long-time connection of the crowbar, while, nowadays, the active crowbar is used in practice, where the crowbar becomes active only for several cycles. Further, the impact of the off-nominal frequency component in the DFIG fault signals on the frequency tracking and phasor measurement units of protective relays during unbalanced faults remains unknown.

1.3 Research Scope and Objectives

The reviewed research papers have unveiled some problems associated with the DFIGs during LVRT conditions and operation of protective relays in the presence of DFIGs. Several solutions have also been proposed to address these problems. However, many aspects of problem identification and solution developments have been left unidentified. The following highlights the main objectives of this dissertation to contribute to this topic.

1. The first objective is to unveil why/how does the phase difference between the negative-sequence current and voltage deviate considerably from 90° when a DFIG uses the control methods applied by DFIG manufacturers. It is also intended to find all possible ranges for the angle of the DFIG negative-sequence current. The results of this work sheds light on several so-far-unknown and critical aspects of this problem that are not discussed in the literature, including the 2800 Standard.

2. The second objective is to reveal how can the protection systems be impacted by the exemption made by IEEE 2800 Standard during LVRT of DFIGs, i.e., 90°–150° phase difference between the negative-sequence current and voltage at the DFIG terminals. An answer to this question resolves the uncertainty about the operation of relays in the proximity of DFIG-based wind plants acknowledged by the 2800 Standard. However, it is not possible to investigate all protection functions that depend on negative-sequence quantities in this work. Therefore, the focus of this dissertation will be on the relays' phase selection elements, which are sensitive to variations of the negative-sequence current angle.

3. The third objective is to come up with a solution to obviate the need for the DFIG exemption in future revisions of the 2800 Standard without imposing a prohibitive cost on DFIG manufacturers. The solution should be comprehensive and capable of addressing both positive- and negative-sequence current requirements of the GCs. It should not require a hardware upgrade either.

4. The forth objective is to investigate how the frequency tracking and phasor measurement units of commercial relays are impacted by the off-nominal frequency components in the DFIG fault signals during the crowbar and/or chopper connection. As reliable operation of protective relays is closely tied with correct operation of the frequency tracking and phasor measurement unit, this objective is a foundation for the study of protective relays' operation in the presence of DFIGs.

5. As the existing literature have investigated the operation of distance relays during the crowbar connection for balanced faults, the fifth objective is to analyze how they operate during unbalanced faults. This dissertation focuses on distance relays that operate based on the apparent impedance approach and the reactance method, as a common method used by state-of-the-art commercial relays.

6. Finally, this dissertation aims to propose a new method for correct operation of distance relays protecting DFIG-based WTs' tie-line during the crowbar and/or chopper connection.

1.4 Dissertation Outline

The rest of this dissertation is organized as follows:

Chapter 2 describes the control of DFIGs with CVC and DCC schemes applied by DFIG manufacturers. This chapter also describes the LVRT of DFIGs during uninterrupted and interrupted control of the RSC considering the crowbar and braking chopper operations. Moreover, it is described how the current references during LVRT of DFIGs are determined for widely used DFIGs.

Chapter 3 (i) sheds light on several so-far-unknown DFIG characteristics that impact the angle of the negative-sequence current during LVRT, (ii) reveals the impacts of the previously mentioned DFIG exemption on relays, and (iii) develops a solution to prevent the need for this exemption in the future revisions of the IEEE 2800 Standard.

Chapter 4 (i) investigates the fault current characteristics of DFIGs during unbalance faults and the crowbar connection, (ii) shows how the DFIG fault signals impact frequency tracking and phasor measurement units of commercial relays, (iii) investigates operation of distance relays that operate based on the apparent impedance approach and the reactance method, and (iv) proposes a solution for correct operation of distance relays during unbalanced faults and interrupted control of the RSC.

Chapter 5 concludes this dissertation, highlights its contributions, and provides an insight into possible future works.

Chapter 2

DFIG-based WT Dynamics and Control

In DFIGs, the stator is directly connected to the grid whereas the rotor is integrated into the grid by partially rated back-to-back converters. These converters provide independent control of active and reactive powers and variable speed operation of DFIGs. There are numerous control techniques for DFIGs [7], and research on new DFIG control schemes is ongoing. This study focuses on the mainstream established control strategies used by DFIG manufacturers, i.e., CVC and DCC schemes. This chapter first reviews the DFIG dynamics during normal operation and during voltage dips. Afterwards, it studied the control of the DFIG during normal operation and LVRT condition.

2.1 DFIG Dynamics

The dynamic forth-order model of a DFIG in the static stator-oriented reference frame is given by (2.1) (2.2) (2.3) (2.4) [42].

$$\vec{v}_s^s = R_s \vec{i}_s^s + \frac{d}{dt}\vec{\psi}_s^s \tag{2.1}$$

$$\vec{v}_r^s = R_s\vec{i}_r^s + \frac{d}{dt}\vec{\psi}_r^s - j\omega_m\vec{\psi}_r^s \tag{2.2}$$

$$\vec{\psi}_s^s = L_s\vec{i}_s^s + L_m\vec{i}_r^s \tag{2.3}$$

$$\vec{\psi}_r^s = L_s\vec{i}_r^s + L_m\vec{i}_s^s \tag{2.4}$$

In these equations, $(\vec{\cdot})$ is the space vector of a component; L denotes inductance; subscripts s, r, and m indicate the quantities of the DFIG's stator, rotor, and magnetizing branch; superscript s indicates the stator reference frames; ψ denotes flux; ω is the grid frequency; and ω_m is the rotor speed.

Using (2.2), (2.3), and (2.4), the rotor voltage can be expressed as a function of the stator flux at the stator static frame as in (2.5) [7].

$$\vec{v}_r^s = \left(R_r + \sigma L_r\left(\frac{d}{dt} - j\omega_m\right)\right)\vec{i}_r^s + \underbrace{\frac{L_m}{L_s}\left(\frac{d}{dt} - j\omega_m\right)\vec{\psi}_s^s}_{\vec{e}_{r,\text{ind}}^s} \tag{2.5}$$

In this equation, $\sigma = 1 - L_m^2/L_sL_r$ is the leakage coefficient of the machine. $\vec{v}_r^s$ in (2.5) consists of two terms. The first term is the voltage drop due to the rotor resistance and the rotor transient inductance. This term appears only if a current flows through the rotor winding. The second term, $\vec{e}_{r,\text{ind}}^s$, is the induced voltage by the stator flux. If the stator resistance is neglected, the stator flux is a space vector rotating at the synchronous speed given by

$$\vec{\psi}_s^s = \frac{V_s}{j\omega_s}e^{j\omega_s t} \tag{2.6}$$

where V_s is the nominal stator voltage. Using (2.6) in (2.5), $\vec{e}^s_{r,\text{ind}}$ is obtained as

$$\vec{e}^s_{r,\text{ind}} = \frac{L_m}{L_s} s V_s e^{j\omega_s t} \tag{2.7}$$

Since the rotor resistance and transient inductance are small, the voltage at the rotor terminals is approximately equal to $\vec{e}^s_{r,\text{ind}}$. The controllability of the DFIG depends on whether the RSC can generated a voltage equal to $\vec{e}^s_{r,\text{ind}}$. In a DFIG with the nominal slip range of $\pm 30\%$, the converters are rated at about 35% of the nominal power. Therefore, the RSC can provide the required voltage and control the DFIG during normal operation. The following finds the induced rotor voltage during balance and unbalanced voltage dips.

2.1.1 Balanced Dips

When a symmetrical voltage dip with the depth of d occurs in the network, the flux linkage of the stator is divided into two components, namely, forced flux and dc flux. Using (2.1) and (2.6), the stator flux is expressed as

$$\vec{\psi}^s_{s,\text{fault}}(t) = \vec{\psi}^s_{sf}(t) + \vec{\psi}^s_{s,\text{dc}}(t) = \frac{V_s(1-d)}{j\omega} e^{j\omega t} + \frac{V_s d}{j\omega} e^{-t/T_s} \tag{2.8}$$

where $\vec{\psi}^s_{sf}(t)$ and $\vec{\psi}^s_{s,\text{dc}}(t)$ are the stator forced flux and dc flux, respectively; T_s is the stator time constant; $d = V_s - V_{\text{fault}}$; and V_{fault} is the stator voltage during the voltage dip. The forced flux is the positive-sequence rotating flux and appears due to the stator fault voltage. The dc flux is a transient flux that guaranties the continuity of the stator flux before and after the fault. This flux decays with

the stator time constant [16]. Each flux induces a voltage in the rotor winding. Using (2.5), (2.6), and (2.8), the induced rotor voltage during balanced voltage dips in the stator reference frame can be obtained. Transferring it to the rotor reference frame yields (2.9) [16].

$$\vec{e}^{\,r}_{r,\text{ind}} = \frac{L_m}{L_s} V_s \left((1-d) s e^{js\omega_s t} - d(1-s) e^{j\omega_m t} e^{-t/T_s} \right) \tag{2.9}$$

In this equation, superscript r indicates the rotor reference frame. The first term on the right hand side of (2.9) is due to the stator forced flux. It is proportional to the slip ,s, and thus, has a small amplitude. The second term is due to the stator dc flux and is a function of (1-s) and the depth of voltage dip. Therefore, its magnitude can be high during severe voltage dips and/or high speed operation of the DFIG. If a DFIG operates with a slip in the range of $\pm 30\%$, the initial value of $\vec{e}^{\,r}_{r,\text{ind}}$ can reach to several times of the RSC maximum voltage capacity [43].

Fig. 2.1 shows the equivalent circuit of a DFIG seen from the rotor side [44]. According to this figure, the rotor current is determined by the voltage difference between the RSC and the induced rotor voltage. If the induced voltage in the rotor winding is higher than the maximum voltage of the RSC, which occurs during low impedance faults or faults that happen close to the DFIG terminals, the converter will be saturated and the control of the rotor current will be lost transitory. Therefore, if no counter measurement is taken, inrush currents in the rotor will flow, which can damage the RSC switches and the dc-link capacitor.

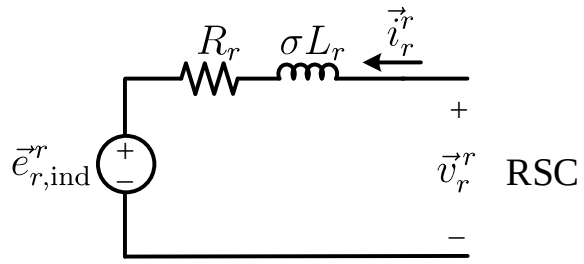

Figure 2.1: Equivalent circuit of a DFIG seen from the rotor side.

2.1.2 Unbalanced Dips

The stator flux during unbalanced voltage dips in the stator reference frame is given by (2.10) [16].

$$\vec{\psi}_{s,\mathrm{fault}}^s = \vec{\psi}_s^{s+} + \vec{\psi}_s^{s-} + \vec{\psi}_s^{s0} = \frac{V_s^+}{j\omega_s} e^{j\omega_s t} + \frac{V_s^-}{-j\omega_s} e^{-j\omega_s t} + \psi_{s,\mathrm{dc0}} e^{-t/T_s} \tag{2.10}$$

In this equation, $\vec{\psi}_s^{s+}$ is the stator positive-sequence flux which is caused by the stator positive-sequence voltage V_s^+; $\vec{\psi}_s^{s-}$ is the stator negative-sequence flux which is caused by the stator negative-sequence voltage V_s^-; $\vec{\psi}_s^{s0}$ is the stator dc flux which appears to guaranties the continuity of the stator flux before and after the voltage dip; and $\psi_{s,\mathrm{dc0}}$ is the initial value of the dc flux. During unbalanced faults, the magnitude of $\psi_{s,\mathrm{dc0}}$ depends on the phase shift between the stator positive- and negative-sequence fluxes at the fault instant. If the two fluxes are aligned, $\psi_{s,\mathrm{dc0}}$ will be zero. The magnitude of $\psi_{s,\mathrm{dc0}}$ increases commensurate with the phase shift between positive- and negative-sequence fluxes. The maximum dc flux occurs when the two sequence fluxes are 180° out of phase [16].

Each flux induces a voltage in the rotor winding. Using (2.5) and (2.10), the induced rotor voltage during unbalanced voltage dips in the stator reference frame can be obtained. Transferring

it to the rotor reference frame yields

$$\vec{e}^{\,r}_{r,\text{ind}} = \vec{e}^{\,r+}_{r,\text{ind}} + \vec{e}^{\,r-}_{r,\text{ind}} + \vec{e}^{\,r0}_{r,\text{ind}} = \frac{L_m}{L_s}\left(sV_s^{+}e^{js\omega_s t} + (2-s)V_s^{-}e^{-j(2-s)\omega_s t} - j\omega_m \psi_{s,\text{dc0}} e^{-j\omega_m t} e^{-t/T_s}\right) \tag{2.11}$$

in which $\vec{e}^{\,r+}_{r,\text{ind}}$, $\vec{e}^{\,r-}_{r,\text{ind}}$, and $\vec{e}^{\,r0}_{r,\text{ind}}$ are the positive-sequence, negative-sequence, and the dc components of the induced rotor voltage, respectively. As it is evident from (2.11), the induced rotor voltage during unbalanced voltage dips is composed of three terms which correspond to the sequence fluxes in (2.10). Similar to the case of symmetrical faults, $\vec{e}^{\,r}_{r,\text{ind}}$ in (2.11) can reach multiple times of the RSC maximum voltage capacity. While $\vec{e}^{\,r0}_{r,\text{ind}}$ decays with the stator time constant, $\vec{e}^{\,r+}_{r,\text{ind}}$ and $\vec{e}^{\,r-}_{r,\text{ind}}$ sustain till the end of the fault. If no counter measurement is taken, inrush currents in the rotor will flow which can damage the RSC switches and the dc-link capacitor.

2.2 CVC-based DFIG control

This widely used conventional control scheme for DFIGs is detailed in [45]. The following briefly reviews the RSC and the GSC control system in the CVC scheme.

2.2.1 RSC Control

This control is implemented by referring all ac quantities to the dq SRF whose q axis is aligned with the stator's positive-sequence voltage. The RSC controller aims to regulate only the positive-sequence current of the stator. The RSC control has two outer q and d axis control loops that control the stator active and reactive powers, respectively. The active power reference, denoted by P_s^*, is

typically determined by the maximum power point tracking technique [46]. The reactive power reference, indicated by Q_s^*, is constant and determines the power factor (PF) of the DFIG. Neglecting the small stator resistance, the active and reactive powers generated at the DFIG terminals in the space vector notation are given by (2.12) and (2.13), respectively [7].

$$P_s = -\frac{3}{2} V_{sq} \frac{L_m}{L_s} i_{rq} \tag{2.12}$$

$$Q_s = \frac{3}{2} \left(\frac{V_{sq}^2}{\omega L_s} - V_{sq} \frac{L_m}{L_s} i_{rd} \right) \tag{2.13}$$

In these equations, subscripts d and q indicate the d and q axis components, respectively. Equations (2.12) and (2.13) indicate that the active and reactive powers of the DFIG are independently controlled by the q and d axis components of the rotor current, respectively. (2.12) and (2.13) also yields the rotor q and d axis reference currents, denoted by i_{rd}^* and i_{rq}^*.

Each axis has one inner current control loop that controls the rotor currents to generate the current references obtained from (2.12) and (2.13). The rotor currents are controlled using the RSC by adjusting the voltage at the rotor terminals. The relation between the rotor voltages and currents in the dq SRF during the steady state condition are as in (2.14) and (2.15) [7].

$$v_{rd} = R_r i_{rd} - s\,\omega\,\sigma L_r i_{rq} + \sigma L_r \frac{d}{dt} i_{rd} + \frac{L_m}{L_s} \frac{d}{dt} \psi_{sd} \tag{2.14}$$

$$v_{rq} = R_r i_{rq} + s\,\omega\,\sigma L_r i_{rd} + \sigma L_r \frac{d}{dt} i_{rq} + s\omega \frac{L_m}{L_s} \psi_{sd} \tag{2.15}$$

From the control perspective, $s\,\omega\,\sigma L_r i_{rq}$ and $s\,\omega\,\sigma L_r i_{rd}$ are cross coupling terms that relate the d

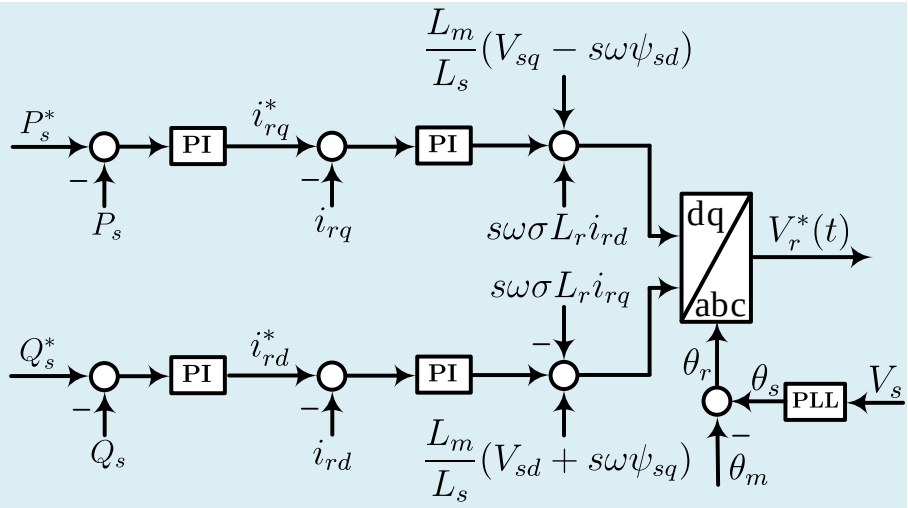

Figure 2.2: Overall structure of the RSC control system.

and q axis loops. These terms appear due to the difference between the rotor speed and the SRF. To decouple the d and q axis loops, these terms are feed-forwarded into their respective control loops. The terms multiplied by L_m/L_s are perturbations as they depend on the stator variables that are independent of the loops. These terms are the induced voltages by the stator flux at the rotor winding. These terms are constant during normal operation of the DFIG and do not affect the control system [7]. However, the are frequently estimated and feed-forwarded to the control loop to reduce their negative effects on the control system during transients.

Fig. 2.2 shows the overall structure of the RSC control system obtained from (2.12), (2.13), (2.14), and (2.15). In this figure, superscript * indicates the setpoint of a quantity; θ_s is the position of the stator positive-sequence voltage, θ_s, which is detected by the phase locked loop (PLL); θ_m is the angular position of the rotor, which in practice is estimated by means of an encoder coupled to the rotor [7]; and θ_r is the angle required for the Park's inverse transformation.

2.2.2 GSC Control

This control is implemented by referring all ac quantities to the dq SRF whose d axis is aligned with the GSC's positive-sequence voltage. The GSC control has two outer d and q axis control loops that control the dc-link voltage, V_{dc}, and the GSC reactive power, Q_g, respectively. These outer control loops determine the reference currents of the GSC. The GSC reactive power is normally set to zero during normal operations.

Each axis has one inner current control loop that controls the GSC currents to generate the current references determined by the outer control loops, denoted by i_{gd}^* and i_{gq}^* for d and q axis currents, respectively. The GSC currents are controlled by adjusting the voltage at the GSC terminals. The relation between the GSC voltages and currents in the dq SRF during the steady state condition are as in (2.16) and (2.17) [47].

$$v_{gd} = R_g i_{gd} - \omega L_{gf} i_{gq} + L_{gf} \frac{d}{dt} i_{gd} + v_{sd} \tag{2.16}$$

$$v_{gq} = R_g i_{gq} + \omega L_{gf} i_{gd} + L_{gf} \frac{d}{dt} i_{gq} + v_{sq} \tag{2.17}$$

In (2.16) and (2.17), L_{gf} is the inductance of the GSC filter. Subscripts g indicates the GSC quantities. The d and q axis loops are cross coupled by $\omega L_{gf} i_{gq}$ and $\omega L_{gf} i_{gd}$, respectively. These terms are feed-forwarded in the GSC control system to decouple the d and q axis control loops. The overall structure of the GSC is shown in Fig. 2.2.

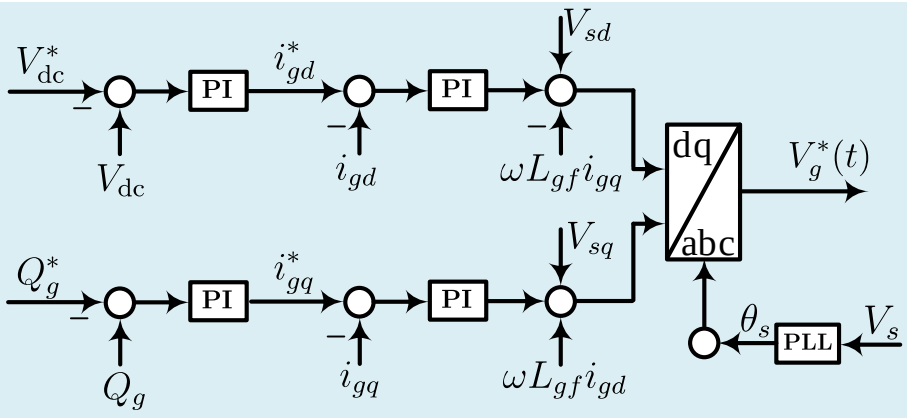

Figure 2.3: Overall structure of the GSC control system.

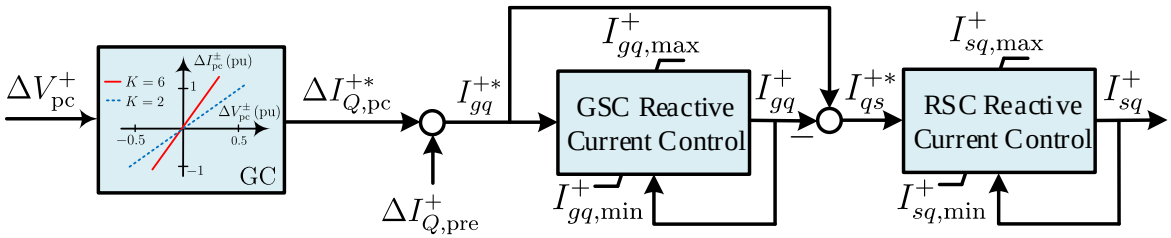

Figure 2.4: Coordinated control of positive-sequence reactive current at the POC.

2.2.3 LVRT of the DFIG with CVC scheme

As mentioned in Section 1.1, almost all GCs require that IBRs generate positive-sequence reactive current at the POC to support the grid during LVRT condition. In this study, the magnitude of the positive-sequence current at the POC is determined using the *K*-factor diagram of Fig. 1.2. There is no control over negative-sequence current is the CVC scheme, and it is assumed that the DFIG generates negative-sequence reactive current [11].

Fig. 2.4 shows the coordinated control of the GSC and the RSC. In this figure, $\Delta I_{\rm Q,pre}^+$ is the pre-fault reactive current of the DFIG; I_{qs}^+ is the reactive current of the stator; the parameters with min and max subscripts designate the minimum and maximum current thresholds of the RSC and

the GSC. In Fig. 2.4, the priority of the positive-sequence reactive current generation is given to the GSC. In Fig. 2.4, $\Delta I^{+*}_{Q,\text{pc}} + I^{+}_{Q,\text{pre}}$ is given as a reference the GSC. While keeping a constant dc-link voltage level is the GSCs' main control objective, it generates a reactive current only if any capacity is left in the converter. The reactive current of the GSC, I^{+}_{qg}, is subtracted from the reference current, and the error, i.e., I^{+*}_{sq}, is given as a reference to the RSC. Therefore, the RSC will generate a positive-sequence reactive current only if the GSC is unable to provide the demanded value. The remaining capacity of the RSC is used to generate positive-sequence active current. With the control scheme of Fig. 2.4, while the maximum available current of the GSC is used, the demanded reactive current is automatically distributed between the two converters.

2.3 DCC Scheme

This control scheme is one of the mainstream established control strategies, and is detailed in [4] and [48]. The following briefly reviews the RSC and the GSC control systems in the DCC scheme.

2.3.1 RSC control

The RSC in the DCC scheme is consists of a main and an auxiliary control loop. The main control loop aligns the q axis of the positive-sequence SRF, dq^{+}, for the RSC controller with the stator's positive-sequence voltage. The auxiliary control or negative-sequence control aligns the q axis of the negative-sequence SRF, dq^{-}, for the RSC controller with the stator's negative-sequence voltage [4]. During normal operation, only the positive-sequence control loop is active for the RSC. Therefore, the operation of the RSC in DCC is similar to the CVC scheme discussed in Section

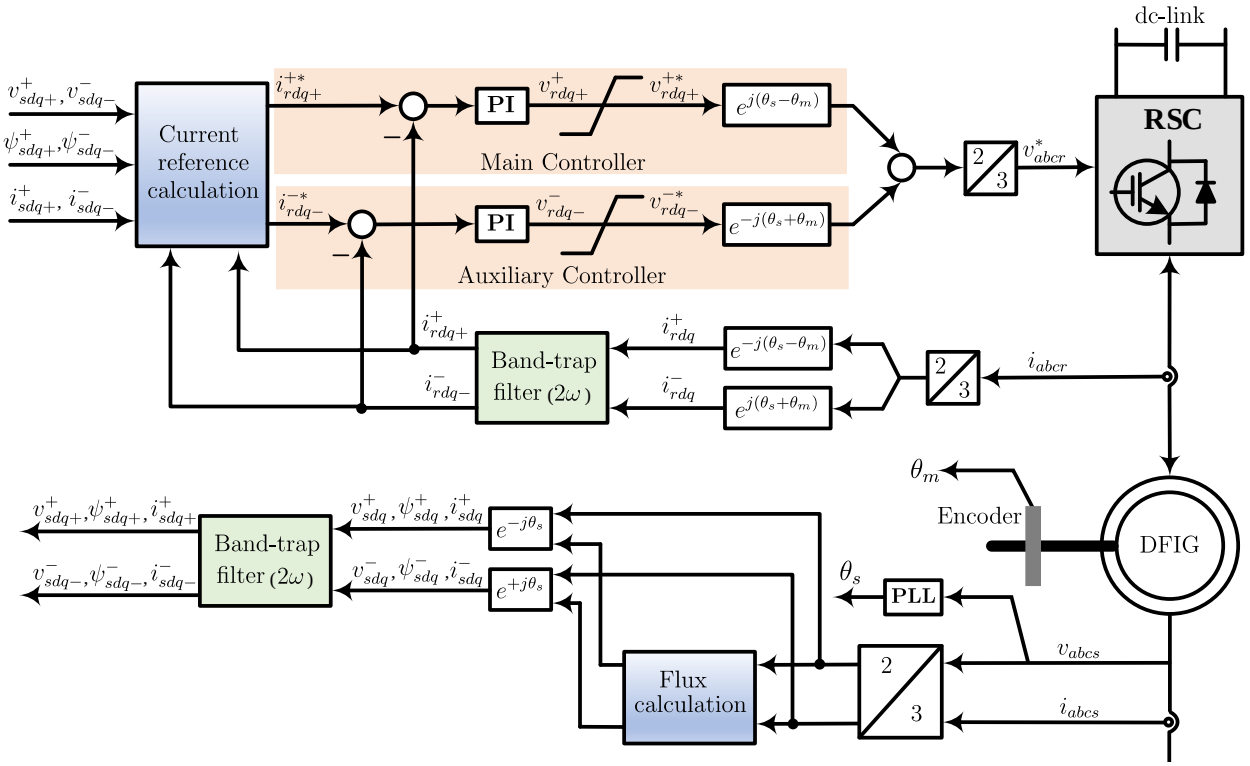

Figure 2.5: Schematic diagram of the DCC scheme [4].

2.2.1. Once the DFIG detects an unbalance condition or enters an unbalanced LVRT mode, the auxiliary control loop is also activated, which regulates the d and q axis currents of the RSC in the dq^- SRF, denoted by i_{rd}^- and i_{rq}^-, respectively. The auxiliary controller of the RSC eventually regulates the stator's negative-sequence current.

Fig. 2.5 shows overall structure of the RSC control in the DCC scheme. In this figure, the subscripts $+$ and $-$ denote the positive and negative components while superscripts $+$ and $-$ indicate the positive and negative SRFs, respectively. In this figure, θ_s is used to transfer the stator components to the $dq+$ and $dq-$ SRFs. $\theta_s - \theta_r$ and $\theta_s + \theta_r$ are used to transfer the rotor currents to $dq+$ and $dq-$ SRFs, respectively. In DCC scheme, while the positive components appear as dc in the positive-sequence SRF, the negative components appear as double the grid frequency.

Similar condition applies to the negative-sequence SRF. To filter out the double the grid frequency components, the signals are passed through band-trap filters tuned at double the grid frequency.

Once the stator and the rotor signals are transferred to $dq+$ and $dq-$ SRFs, they are used to calculate the rotor current references, i.e., $i^{+*}_{rdq^+}$ and $i^{-*}_{rdq^-}$. During normal operation, $i^{+*}_{rdq^+}$ is obtained using using (2.12) and (2.13), and $i^{-*}_{rdq^-} = 0$. During unbalanced or LVRT condition, $i^{+*}_{rdq^+}$ and $i^{-*}_{rdq^-}$ are determined based on the host GC requirement and operational capability of the DFIG. The reference currents are then passed to the main and auxiliary controllers. The controllers determine the required rotor control voltages in the $dq+$ and $dq-$ SRFs, i.e., V^{+*}_{rdq+} and V^{-*}_{rdq-}, respectively. To make sure that the required rotor control voltage does not exceed the maximum capacity of the RSC, the rotor voltage limit block scales out the output from the auxiliary controller if the overall voltage exceeds the RSC maximum capacity. By doing so, the RSC fully generates the required positive-sequence voltage to follow the positive-sequence current references. The required negative-sequence voltage is fully or partially generated only if the RSC still has some extra capacity. This issue does not result in the rotor over-current since the rotor impedance in negative-sequence is very high [49]. V^{+*}_{rdq+} and V^{-*}_{rdq-} are transferred back to the abc quantities before giving them to the RSC. A full description of how the stator and rotor quantities are transferred between different frames can be found in [48]. Pulse width modulation (PWM) is used to generate the switching pattern for the RSC to produce the rotor voltage references.

2.3.2 GSC control

Several DCC schemes have been presented in the literature for the GSC control. This control schemes regulate the dc-link capacitor and the reactive power of the GSC in the positive-sequence SRF. Several control targets, such as eliminating the second order pulsations in the dc-link voltage and the active or reactive power of the DFIG, can be assigned to the negative-sequence controller [50]. However, as in practical applications it is more common to operate the GSC with symmetrical currents [51], similar control system of Fig. 2.3 is used here.

2.3.3 LVRT of the DFIG with DCC scheme

Similar to the CVC scheme, the coordinated control of Fig. 2.4 is used to fulfill the positive-sequence reactive current requirements of the GCs. In this method, while the GSC generates positive-sequence reactive current to its maximum capacity, the RSC positive-sequence reactive current reference, i.e., i^*_{sq}, is determined and passed to the RSC.

During unbalanced or LVRT condition in DCC scheme, there are four rotor currents, i.e., i^+_{rd+}, i^+_{rq+}, i^-_{rd-}, and i^-_{rq-}, that can be independently controlled. The control targets of a DFIG during LVRT condition is determined based on the host GC requirements, such as [2] and [11], and operational capability of the DFIG. In almost all grid codes, the control of the average positive-sequence active and reactive currents are required. Therefore, this method prioritizes the control of positive-sequence active and reactive currents through the RSC's positive-sequence control loop. The reference for the positive-sequence reactive current, i^*_{sq}, is determined from Fig. 2.4. As there is no specific

requirement for generation of positive-sequence active current in [2], this current is generated if any capacity is left in the RSC after fulfillment of the positive-sequence reactive current requirements and the negative-sequence current setpoints discussed in the following.

Various objectives can be targeted by the negative-sequence control. For example, the negative-sequence current references of the RSC can be designed to address one of the following control targets that arise as a result of voltage unbalance at the DFIG terminals:

Target 1) Eliminating the stator negative-sequence current, and hence, creating a balanced stator current. This target results in a balanced heating on the DFIG's three phase stator winding.

Target 3) Eliminating the rotor negative-sequence current, and hence, creating a balanced rotor current.

Target 4) Eliminating the second harmonic active power pulsations.

Target 5) Eliminating the second-harmonic electromagnetic torque pulsations (ETPs). This target reduces the mechanical stress as it avoids vibrations in the shaft.

Target 6) Minimizing the rotor voltage.

The common objective in practice for negative-sequence control is minimization of the second-harmonic ETPs caused by voltage imbalance [44, 52, 53]. It is because the second harmonic ETPs can result in high torsional oscillation and can deteriorate the lifetime of the drive shaft and mechanical units. The electromagnetic torque equation can be written as in (2.18) [48].

$$T_e = \frac{pP_{\text{mec}}}{\omega_m} \tag{2.18}$$

In this equation, p is the number of pole pairs and P_{mec} is the mechanical power. According to

(2.18), constant torque means constant mechanic power. During unbalanced faults, the mechanical power is defined as in (2.19) [48].

$$P_{mec} = \frac{3}{2}\frac{L_m}{L_s}\omega_m Im\left[\vec{\psi}^{+}_{sdq}\bar{\vec{i}}^{+}_{rdq}\right] = P_{m0} + P_{\text{msin}} sin\left(2\omega t\right) + P_{\text{mcos}} cos\left(2\omega t\right) \tag{2.19}$$

where

$$\begin{bmatrix} P_{m0} \\ P_{\text{msin}} \\ P_{\text{mcos}} \end{bmatrix} = \frac{3}{2}\frac{L_m}{L_s}\omega_m \begin{bmatrix} -\psi^{+}_{sq+} & \psi^{+}_{sd+} & -\psi^{-}_{sq-} & \psi^{-}_{sd-} \\ \psi^{-}_{sd-} & \psi^{-}_{sq-} & -\psi^{+}_{sd+} & -\psi^{+}_{sq+} \\ -\psi^{-}_{sq-} & \psi^{-}_{sd-} & -\psi^{+}_{sq+} & \psi^{+}_{sd+} \end{bmatrix} \cdot \begin{bmatrix} i^{+}_{rd+} \\ i^{+}_{rq+} \\ i^{-}_{rd-} \\ i^{-}_{rq-} \end{bmatrix} \tag{2.20}$$

$(\bar{\cdot})$ in (2.19) denotes the complex conjugate of a number. P_{msin} and P_{mcos} in the right hand side of (2.19) are the reasons for the second harmonic ETPs. Solving (2.20) for $P_{\text{msin}} = 0$ and $P_{\text{mcos}} = 0$ yields

$$i^{-*}_{rd-} = \frac{\psi^{-}_{sd-}}{\psi^{+}_{sd+}} i^{+}_{rd+} + \frac{\psi^{-}_{sq-}}{\psi^{+}_{sd+}} i^{+}_{rq+} \tag{2.21}$$

$$i^{-*}_{rq-} = \frac{\psi^{-}_{sq-}}{\psi^{+}_{sd+}} i^{+}_{rd+} - \frac{\psi^{-}_{sd-}}{\psi^{+}_{sd+}} i^{+}_{rq+} \tag{2.22}$$

where i^{-*}_{rd-} and i^{-*}_{rq-} are the rotor d and q references in the dq^{-} SRF to minimize the second harmonic ETPs.

2.4 Uninterrupted and interrupted control of the DFIG

As mentioned earlier in Section 2.1, during a grid fault that causes a voltage dip, the stator flux induces large voltages in the rotor of a DFIG. Depending on the maximum magnitude of the induced rotor voltage, the DFIG control can experience an uninterrupted or interrupted control of the RSC. The following describes the operation of the DFIG during these two modes of operation.

2.4.1 Uninterrupted control of the DFIG

During non-severe grid faults, which happens for high impedance faults, the magnitude of the induced rotor voltage does not exceed the maximum voltage capacity of the RSC. Therefore, the RSC keeps the control of the rotor currents and continues to control the DFIG. In this mode of operation, the DFIG enters to the LVRT mode and both the GSC and the RSC are controlled as discussed in subsections 2.2.3 and 2.3.3 for CVC and DCC schemes, respectively.

2.4.2 Interrupted control of the DFIG

During severe grid faults, which happens for low impedance faults or close-in faults, the magnitude of the induced rotor voltage exceeds the maximum voltage capacity of the RSC. In such conditions, the rotor current control will be lost and large overcurrents in the rotor winding and large over-voltages in the dc-link capacitor of the back-to-back converter appears that can damage the RSC switches and the dc-link capacitor. To protect the RSC and the dc-link capacitor, several hardware modifications and control schemes are proposed in the literature. Among them, the braking chopper

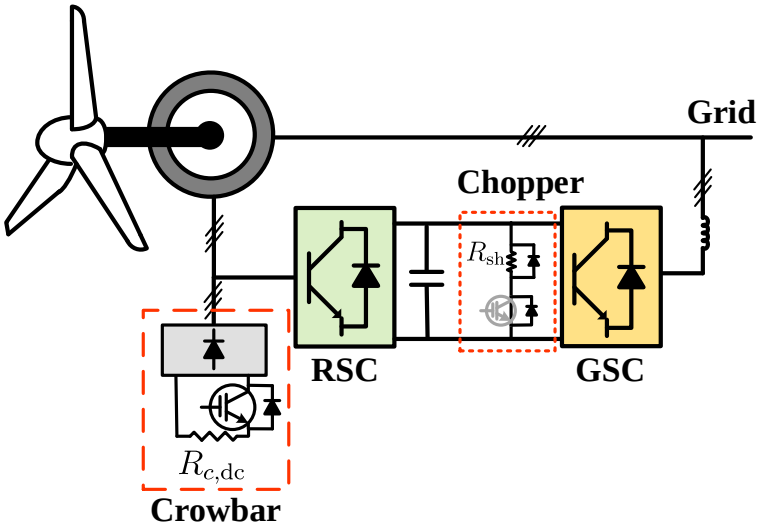

Figure 2.6: A DFIG-based WT equipped with an active crowbar and a breaking chopper [5].

and the crowbar circuit are the most common [54]. The crowbar is used alone or in a combination with a breaking chopper, as shown in Fig. 2.6. The following briefly describes the crowbar and the braking chopper and the DFIG operation during interrupted control of RSC.

Crowbar: Installation of the crowbar in the rotor is the most common approach to protect the RSC and the dc-link capacitor from overcurrents and overvoltages [54]. The crowbar shorts the rotor winding through some resistors and so limits the overcurrents in the rotor circuit and prevents overvoltages of the dc-link. The crowbar gets activated when the voltage induced in the rotor winding of a DFIG exceeds the RSC maximum voltage limit, or the rotor current exceeds a predetermined value.

Although the crowbar effectively protects the RSC, it converts the DFIG to a squirrel-cage IG (SCIG). In such a condition, the DFIG can consume substantial amounts of reactive power, which exacerbate the voltage dip. In addition, with the long connection of the crowbar, fast

resumption of the DFIG control is not possible, and so, the DFIG fails to meet the GCs LVRT requirements. In practice, to prevent the reactive power consumption and enhance LVRT capability of the DFIG, DFIGs are equipped with active crowbar circuits [17]. An active crowbar shorts the rotor winding during the first few ms of the fault [17, 18]. During the crowbar connection, the RSC gating is turned off. However, the GSC continues its operation. The active crowbar is then disconnected and the control of the DFIG is resumed to fulfill the GC requirements and eliminate the second harmonic ETPs.

There are several typologies for the crowbar [18]. The crowbar shown in Fig. 2.6 is a three phase crowbar with three resistors, R_c, and bidirectional switches. To reduce the complexity and cost of the crowbar, many manufacturers use a dc crowbar, where the rotor current is rectified with a diode bridge, and so, only one resistor and one bidirectional switch is used [7]. The resistance of the dc crowbar, indicated by $R_{c,\mathrm{dc}}$, is determined as in (2.23).

$$R_{c,\mathrm{dc}} = \frac{\pi^2 R_c}{6} \tag{2.23}$$

Braking Chopper: A braking chopper is a protective device that shorts the dc-link through a resistor when its voltage exceeds a predefined value. The protection of a DFIG equipped with a chopper starts when the rotor current exceeds a predetermined value—typically 2 pu [19]. In such a condition, the RSC control is turned off and gating of the switches are stopped, and the rotor overcurrent is forced to commute through the RSC free-wheeling diodes [19]. This mode of operation is known as rectification mode. In this mode, the GSC and the braking chopper

attempt to regulate the dc-link voltage within the acceptable limit by either transferring the extra power in the dc-link to the grid or dissipating it by the braking chopper resistance. The chopper is activated when the dc-link voltage exceeds a predefined threshold. The chopper is deactivated when the dc-link voltage decreases below a predetermined threshold.

When the rotor current falls below a predefined value, the rectification mode is ended, and so, the RSC control is resumed after a few milliseconds delay. Although the braking chopper can effectively protect the RSC and the dc-link, it needs up-rated anti-parallel diodes of the RSC to handle the maximum overcurrents—typically 5 pu [19]— that appear in the rotor winding.

Combination of Crowbar and Braking Chopper: When the crowbar is used alone, the activation time should be long enough to prevent overvoltages in the dc-link capacitor. Consequently, resumption of the RSC control and fulfilment of the GC requirements will be delayed. To overcome this problem, the crowbar is accompanied by a braking chopper. When used together, the priority of protection is given to the chopper, and the crowbar is activated for deep voltage sags as a last resort. This reduces the number of crowbar activation, and so, enhances LVRT capability of the DFIG.

In this design, the crowbar gets activated only at the beginning of sever voltage dips, where the rotor overcurrents are very high. However, it is deactivated faster as the chopper keeps the dc-link voltage within an acceptable range after the crowbar deactivation. Therefore, the RSC control will be resumed faster, and fulfilment of the GC requirements will be accelerated. During less sever voltage dips, the crowbar will not be activated and the chopper will protect the dc-link in either RSC control mode or the rectification mode.

2.5 Modeling of the DFIG in PSCAD/EMTDC

For the purpose of this dissertation, a detailed model of the DFIG, consists of insulated-gate bipolar transistor (IGBT) switches, is implemented in PSCAD/EMTDC. This subsection briefly describes the modeling of DFIGs in PSCAD/EMTDC.

2.5.1 Overall structure of the DFIG-based wind plant

Fig. 2.7 shows the overall structure of the 51-MW DFIG-based wind plant connected to the POM in PSCAD/EMTDC. The 51-MW wind plant is an aggregated model of 34 wind turbine units, where each unit has a power rating of 1.5 MW. In fact, a 1.5-MW wind turbine is scaled-up to represent the 51-MW DFIGs by multiplying the output current of one DFIG unit by the number of units. This simplification is supported by several studies [55] showing that an aggregated wind farm model is adequate for power system transient voltage studies. The parameters of the generator and the back-to-back converter used in this study is presented in Appendix A.

2.5.2 RSC and GSC overall structure

For the purpose of this dissertation, a detailed model of the RSC and the GSC, consist of insulated-gate bipolar transistor (IGBT) switches, is implemented in PSCAD/EMTDC. The detailed model of the DFIG consists of two-level converters for both the RSC and the GSC and is developed based on IGBT semiconductor switches as shown in Figure 2.8. In detailed model of the converters, three-phase reference voltages are generated using PWM technique, as shown in Fig. 2.9. Full

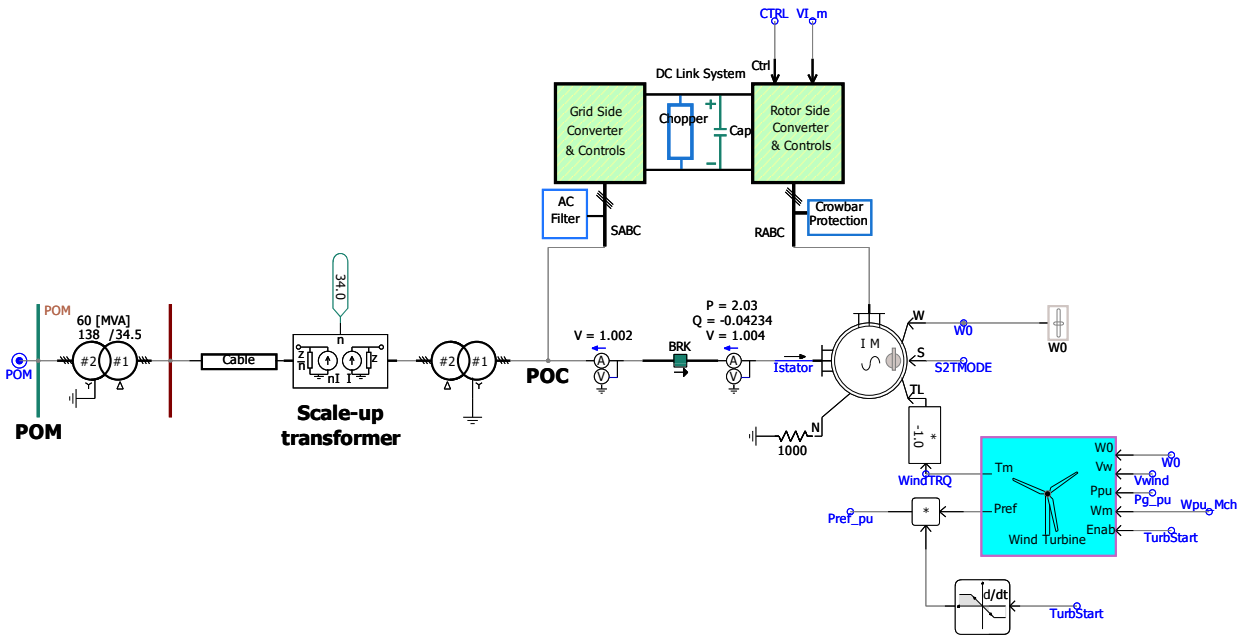

Figure 2.7: Overall structure of the 51-MW DFIG-based wind plant connected to the POM in PSCAD/EMTDC.

description of PWM technique implementation in PSCAD/EMTDC can be found in [6]. The current references of the RSC and the GSC for CVC- and DCC-based DFIGs are generated based on Section 2.2 and 2.3, respectively.

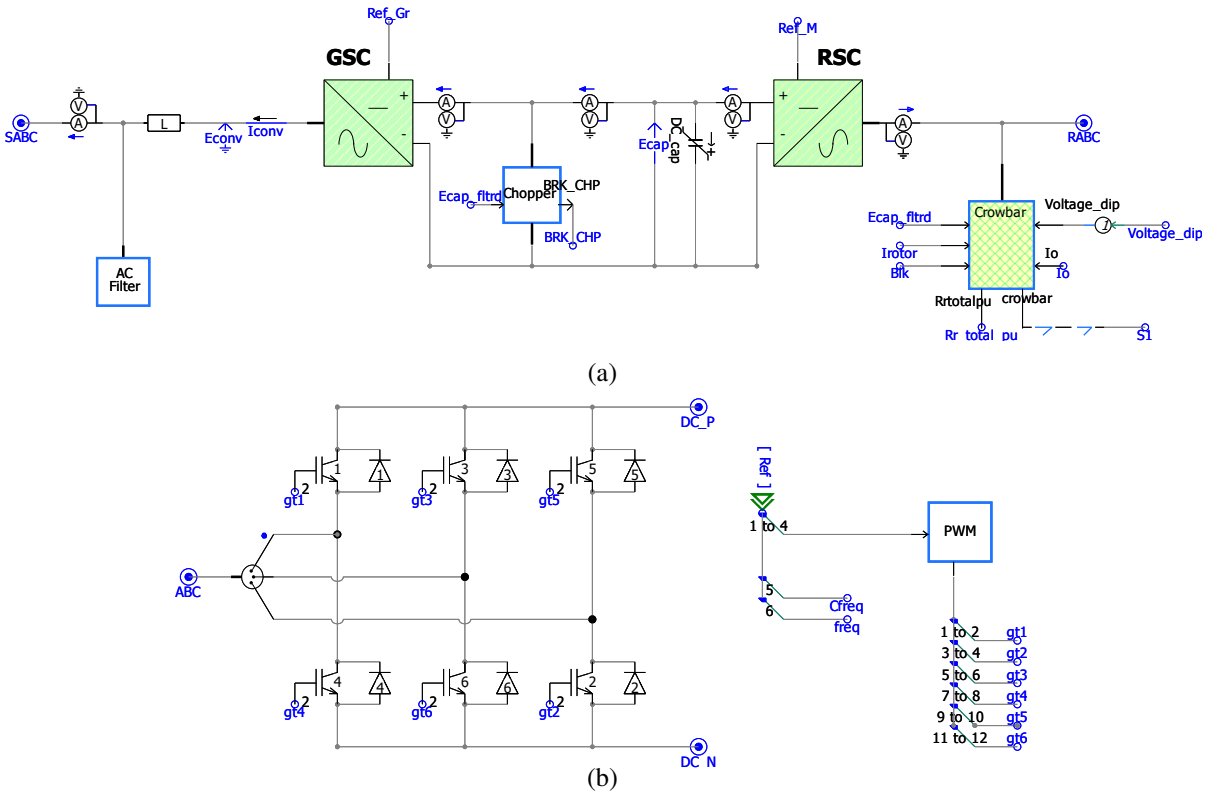

Figure 2.8: Detailed model of the DFIG, (a) RSC and GSC, (b) two level converter.

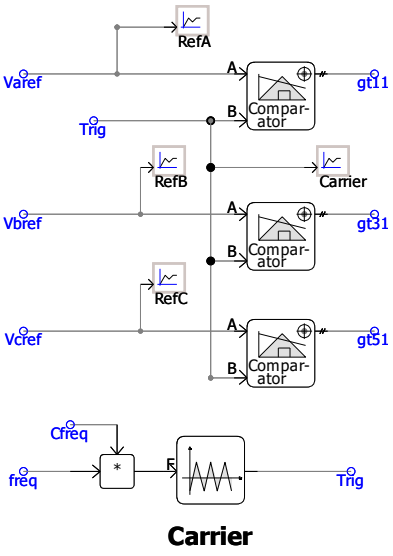

Figure 2.9: Sinusoidal PWM pulse generator [6].

Chapter 3

Eliminating the Need for a Less Strict Requirement for the Negative-Sequence LVRT Current of Type-III Wind Turbine Generators in the IEEE 2800 Standard

The recently approved IEEE 2800 Standard codifies the capability requirements of IBRs for integration with transmission systems [12]. Similar to recent regional GCs, such as [2] and [56], an important part of this Standard is about the performance of IBRs during LVRT conditions. These provisions regulate different aspects of IBR currents during LVRT—such as the current's active/reactive components, response time, etc.—to improve the grid stability and reduce the likelihood of protection malfunction in a system with high penetration of inverter-based generation.

A common feature of emerging GCs and Standards for transmission-connected IBRs, including the 2800 Standard, is the requirement for IBR units to generate negative-sequence current during unbalanced LVRT conditions.

The negative-sequence current required by the GCs during LVRT is primarily reactive, i.e., it must lead the negative-sequence voltage by 90°–100° [2]. Such an angle imitates the negative-sequence current angle of SGs and decreases the probability of malfunction of protective relays—which rely on the negative-sequence components for various functions [14]. The group that drafted the LVRT section of the 2800 Standard was initially going to apply this requirement to all types of IBRs. However, the manufacturers of Type-III wind turbine generators argued that an angle within the [90°, 100°] range was not feasible for the negative-sequence current of available DFIGs. The manufacturers' proposition was that the angle between the negative-sequence current and voltage of DFIGs was highly influenced by the machine parameters and converter limitations, and so it could not be precisely controlled. Thus, the IEEE 2800 Standard eventually exempted DFIGs from this strict requirement and permitted a phase difference within the [90°, 150°] range between the negative-sequence current and voltage of DFIGs during LVRT.

In the meantime, the impact of this DFIG exemption on different elements of protective relays that operate based on the negative-sequence quantities became a concern for the utilities and relay manufacturers. Therefore, Annex J was added at the end of the 2800 Standard to explain the DFIGs' operation during unbalanced LVRT and the necessity for this exemption, at least for today's DFIG technologies. Annex J also acknowledged "At the time of development of this Standard, the impact of this large angle between negative-sequence voltage and current on dependability and security of

traditional protection schemes is not known. Based on engineering judgement, protection functions dependent on negative sequence quantities may be negatively impacted." The lack of clarity about the impacts of this DFIG exemption on protection systems will cause uncertainty about the operation of relays in the proximity of DFIG-based wind plants.

Annex J notes that DFIG manufacturers are working to tackle this problem. However, the potential methodologies briefly mentioned in this annex involve a larger RSC and complex control structures. Therefore, Annex J predicts that the expected solutions may lead to higher cost for DFIGs.

This chapter presents an answer to the following three questions:

1. *Why/how does the phase difference between the negative-sequence current and voltage deviate considerably from 90° when a DFIG uses the control methods applied by DFIG manufacturers?* Our answer to this question sheds light on several critical aspects of this problem that are not discussed in the literature, including Annex J of the 2800 Standard.

2. *How can the protection systems be impacted by the above-mentioned DFIG exemption?* An answer to this question resolves the aforesaid uncertainty acknowledged by the 2800 Standard. As a representative case, this chapter focuses on the relays' phase selection elements, which are sensitive to variations of the negative-sequence current angle [36].

3. *How can the need for this DFIG exemption be obviated in future revisions of the 2800 Standard without imposing a prohibitive cost on DFIG manufacturers?* Our solution leaves the RSC intact and does not involve a complex control scheme. It does not require a hardware upgrade either.

3.1 System Under Study

This section presents different aspects of the system studied in this chapter: (i) the test grid including a DFIG wind plant, (ii) the control system used for the DFIGs, and (iii) the phase selection element of the relay protecting the direct tie-line of this plant.

3.1.1 Test Power Grid

The IEEE 14-bus system in Fig. 3.1 is modeled using PSCAD for this study [57]. The synchronous generator at bus B2 of the original IEEE 14-bus system is replaced with a 51-MW wind plant that includes 34 1.5-MW DFIGs. The plant's main step-up transformer is YGd, 60 MVA, 34.5 kV/230 kV with a leakage reactance of 0.1 pu. As defined in [12], the POM and POC of this plant are at the high-voltage side of the plant transformer and low-voltage side of the turbine transformer, respectively. This plant is connected to bus B2 through line L215, which is 50 km long. R152 is the relay of line L215 at bus B15. The parameters of the DFIGs are presented in Appendix A.

3.1.2 DFIG Control

There are numerous control techniques for DFIGs [7], and research on new DFIG control schemes is ongoing. In this study, we focus on the mainstream established control strategies used by DFIG manufacturers, i.e., the CVC and DCC schemes discussed in Chapter 2.

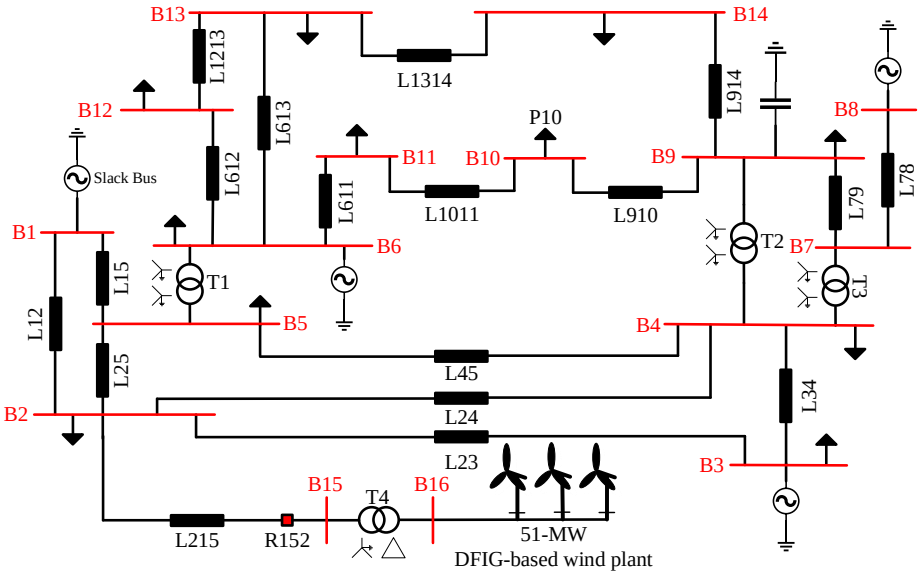

Figure 3.1: Single-line diagram of the test grid.

1) CVC

This widely used conventional control scheme for DFIGs is detailed in [45]. The control is in the *dq* SRF whose *q* axis is aligned with the stator's positive-sequence voltage. The RSC controller aims to regulate only the positive-sequence current of the stator. The controller of the GSC keeps the dc-link voltage constant by regulating the GSC's positive-sequence current. The negative-sequence current is not directly regulated by the control system and is impacted by the machine and the fault characteristics.

2) DCC

This scheme also aligns the *q* axis of the positive-sequence SRF for the RSC controller with the stator's positive-sequence voltage [4]. During LVRT, this method prioritizes the generation of positive-sequence reactive current through the RSC's positive-sequence control loop. Meanwhile,

the RSC control also directly regulates the stator's negative-sequence current. Various objectives can be targeted by the negative-sequence control, but the common objective in practice is minimization of the second-harmonic ETPs caused by voltage imbalance. This is the second priority of the DCC scheme [44]. The GSC control is similar to that of the CVC scheme.

3.1.3 Phase Selection

As mentioned in Chapter 1, protective relays include faulty phase selection elements for various functions, e.g., using the correct distance element and single-pole tripping [15]. This chapter analyzes the operation of this element for relay R152 in Fig. 1.1. Relay R152 employs the widely used current angle-based phase selection method of Fig. 1.3 discussed in Section 1.1. As mentioned in Section 1.1, this method uses the angle difference between the negative- and positive-sequence currents, i.e. $\delta^+ = \measuredangle I^- - \measuredangle I^+$, and the angle between the negative- and zero-sequence currents, i.e. $\delta^0 = \measuredangle I^- - \measuredangle I^0$, to identify the fault type. This method identifies a certain fault type when δ^+ and δ^0 fall in the respective zones of that fault type in Fig. 1.3. Each zone of δ^+ and δ^0 for a fault type is usually extended for $\pm 15^\circ$ and $\pm 30^\circ$ around the zone's center, respectively.

Some relays use only δ^0 to avoid reliance on I^+ [58]. To distinguish between the single line-to-ground (SLG) and line-to-line-to-ground (LLG) faults associated with each zone of δ^0 in Fig. 1.3(b), these relays compare the estimated resistance for the respective SLG and LLG faults, as detailed in [15].

The zones shown for δ^0 and δ^- in Fig. 1.3 are derived based on the negative- and zero-sequence equivalent circuits of synchronous generators. Since each of these circuits consists of a

single highly inductive impedance, the angle between the negative-sequence current and voltage, $\alpha^- = \measuredangle(I^-/V^-)$, and the angle between the zero-sequence current and voltage, $\alpha^0 = \measuredangle(I^0/V^0)$, at the relay location are both around 90° to 100°. For IBRs, α^0 is impacted only by the impedance of the interface transformer, and so it follows the same pattern. However, the impact of different DFIG control schemes on α^- needs to be investigated.

3.2 CVC-Based DFIGs

By deriving a closed-form relation for α^- and testing this relation using simulation, this section scrutinizes α^- of a DFIG that uses CVC. This section also investigates the impact of this α^- on the relays' phase selection element. In the CVC scheme, the GSC regulates the positive-sequence current [45], and so the GSC's negative-sequence current is normally close to zero. The RSC also regulates only the stator's positive-sequence current directly while the stator's negative-sequence current is known to be determined by the fault condition and machine dynamics [59]. This section will investigate if the RSC control can have any indirect impact on the negative-sequence current and consequently on α^-. The relay measures α^- at the POM. However, the negative-sequence voltage across the plant's collector system is not usually large enough to change the voltage angle noticeably and the magnetizing currents of transformers can be neglected. Thus, α^- at the POM (α^-_{pm}) can approximated by α^- at the POC (α^-_{pc}). Therefore, the following discussion focuses on the parameters at the POC.

Neglecting the stator and rotor resistances, the stator's negative-sequence current can be written

as (3.1) [60].

$$I_s^- = j\frac{V_s^-}{\omega L_s} + \frac{L_m}{L_s} I_r^- \tag{3.1}$$

In (3.1), L denotes inductance; subscripts s, r, and m indicate the quantities of the DFIG's stator, rotor, and magnetizing branch; and ω is the grid frequency. If I_r^- on the right side of (3.1) is known, this equation can be used to obtain $\measuredangle(I_s^-/V_s^-)$, denoted by α_s^-. Given the GSC's zero negative-sequence current, $\alpha_{\text{pc}}^- = \alpha_s^-$

During unbalanced faults, the voltage induced in the rotor winding naturally has a negative-sequence component, and so I_r^- flows in the rotor winding. From (2.11) and neglecting the stator resistance and stator flux linkage transients, the voltage induced in the rotor can be expressed in the rotor reference frame as in (3.2) [16].

$$\vec{e}_{r,\text{ind}} = \underbrace{s\frac{L_m}{L_s} V_s^+ e^{js\omega t}}_{\vec{e}_{r,\text{ind}}^+} + \underbrace{(2-s)\frac{L_m}{L_s} V_s^- e^{-j(2-s)\omega t}}_{\vec{e}_{r,\text{ind}}^-} \tag{3.2}$$

In (3.2), s is the machine slip, and $\vec{e}_{r,\text{ind}}^+$ and $\vec{e}_{r,\text{ind}}^-$ are the voltages induced in the rotor due to the positive- and negative-sequence stator voltages, respectively. These two voltages act as disturbances to the RSC control system [7]. As indicated by (3.2), $\vec{e}_{r,\text{ind}}^+$ rotates with the slip frequency in the rotor's reference frame. Thus, it becomes a DC component when it is transferred to the SRF. The rotation frequency of $\vec{e}_{r,\text{ind}}^-$ in the rotor's reference frame, however, is $-(2-s)\omega$. Thus, $\vec{e}_{r,\text{ind}}^-$ is mapped as an oscillatory component with a frequency of -2ω in the SRF. Since proportional integrator (PI) controllers can control only DC quantities ideally, the PI controllers of the RSC control loop are able to compensate for $\vec{e}_{r,\text{ind}}^+$ but not for $\vec{e}_{r,\text{ind}}^-$. Consequently, a sinusoidal component

with a frequency of $-(2-s)\omega$ is superimposed on the fundamental frequency component of the rotor current, oscillating at $s\omega$ [7]. When transferred to the stator side, this superimposed component appears as a negative-sequence current, I_r^- — a negative-sequence current that is the result of RSC control.

The above discussion shows that I_r^- is determined based on (3.2) and the gains of the RSC's PI controllers. As long as the RSC is not saturated, the system is linear and the impact of the RSC controllers' parameters on the magnitude and angle of I_r^- can be analyzed through the superposition principle. Therefore, the DFIG can be decomposed into a positive and a negative machine, representing the DFIG in the positive- ane negative-sequence, respectively, as defined in [7]. These two machines can be studied independently based on the superposition principle.

Fig. 3.2 shows the simplified block diagram of the RSC's inner current control for the negative machine with disturbance e_{dqr}^-. In this chapter, superscript * indicates the setpoint of a quantity; K_p and K_i are the proportional and integral gains of the PI controller, respectively; L_r is the rotor inductance; and $\sigma = 1 - L_m^2/L_sL_r$ is the leakage coefficient of the machine. In this control system, the reference for the negative-sequence current, i_{dqr}^{-*}, is zero because the CVC scheme regulates only the positive-sequence current. In addition, for the first-order control system of the RSC in CVC, K_p and K_i are defined as in (3.3) and (3.4), respectively [59].

$$K_p = 2\pi f_c \sigma L_r \tag{3.3}$$

$$K_i = 2\pi f_c R_r \tag{3.4}$$

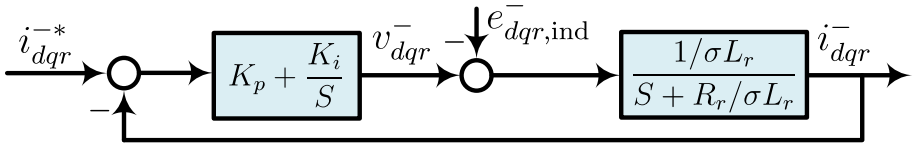

Figure 3.2: Inner current control loop of the RSC for the negative machine [7].

In (3.3) and (3.4), f_c is the bandwidth of the RSC's inner current control loop. If f_c is very small, the RSC control becomes slow (and so the response/settling time requirements of [12] cannot be met). For a very large f_c, the RSC control can become unstable.

Since $R_r << \sigma L_r$, K_i in (3.4) is substantially smaller than K_p in (3.3). Therefore, according to Fig. 3.2, the negative-sequence voltage generated by the RSC control in the rotor winding, V_r^-, is

$$V_r^- = -K_p I_r^- \tag{3.5}$$

In addition to (3.5), which gives V_r^- based on the RSC's control parameters and I_r^-, V_r^- is also related to the machine parameters, V_s^-, and I_r^- through (3.6) [7].

$$V_r^- = \frac{L_m}{L_s}(2-s)V_s^- + j\omega\sigma L_r(2-s)I_r^- \tag{3.6}$$

Using (3.5) and (3.6), I_r^- can be expressed in terms of V_s^- as

$$I_r^- = -\frac{L_m}{L_s}\frac{(2-s)V_s^-}{K_p + j\omega\sigma L_r(2-s)} \tag{3.7}$$

Combining (3.1) and (3.7) yields I_s^- in terms of V_s^-, machine parameters, and K_p:

$$I_s^- = \left(\frac{j}{\omega L_s} - \left(\frac{L_m}{L_s} \right)^2 \times \frac{2-s}{K_p + j\omega\sigma L_r (2-s)} \right) V_s^- \tag{3.8}$$

Finally, (3.3) and (3.8) can be used to derive α_s^- as in

$$\alpha_s^- = \tan^{-1} \left(\frac{(2\pi f_c \sigma L_r)^2 + (2-s)^2 \left((\omega\sigma L_r)^2 + \omega^2 L_m^2 \sigma L_r / Ls \right)}{(2-s) 2\pi f_c \omega\sigma L_r L_m^2 / L_s} \right) \tag{3.9}$$

This equation shows that for a given set of machine parameters, i.e., L_s, L_r, and σ, α_s^- (which equals α_{pc}^-) varies with the slip, s, and the bandwidth of the RSC's current control loop, f_c. Fig. 3.3 displays the variations of α_s^- with respect to s and f_c for the DFIG of Table A.1. In this figure, the range considered for f_c is [100, 500] Hz because the RSC control system is normally designed to have a bandwidth less than one-tenth of the converter's switching frequency [61], which does not usually exceed 5 kHz in practical converters [59]. s also is considered between -30% and 30%, which is the maximum expected range for slip variations [7].

Fig. 3.3 shows that the machine slip variations have a negligible effect on α_s^-. However, α_s^- varies significantly with f_c. α_s^- is directly related to f_c, but once f_c exceeds around 400 Hz, the direct relation between α_s^- and f_c starts to saturate. For smaller bandwidths, the deviation of α_s^- from the ideal range of [90°, 100°] mentioned in this chapter is small. The deviation of α_s^- from the [90°, 100°] range increases commensurate with f_c, and it reaches a maximum of 144.3° for $f_c =$ 400 Hz. Such deviations of α_s^- from the [90°, 100°] range violate one of the main premises based

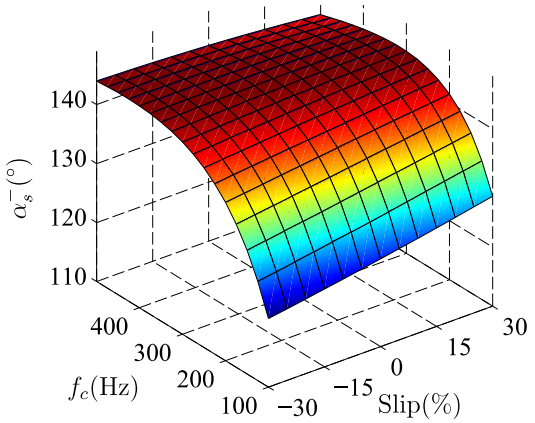

Figure 3.3: Variations of α_s^- with respect to f_c and slip for a CVC-based DFIG.

on which the zones for δ^0 and δ^+ are derived in Fig. 1.3. Therefore, these deviations can potentially cause misoperation of the relays' phase selection element. Such misoperation can adversely impact various other elements of a relay, including distance protection and single-pole tripping.

To elaborate on the above analysis, consider a BCG fault at $t = 2$ s with a fault resistance of $R_f = 15\ \Omega$ at 50% of line L215 in Fig. 3.1. Before the fault, the DFIGs operate at $s = +\,8\%$. The angle of the stator's negative-sequence voltage is almost constant and varies within a small range of 5° to 10° for different values of f_c. The negative-sequence current of the stator, however, depends highly on f_c. This current also leads the negative-sequence voltage by large angles, resulting in the α_s^- curves shown in Fig. 3.4. These curves confirm the pattern derived in (3.9) and demonstrated in Fig. 3.3. α_s^- grows with f_c and reaches 144° for $f_c = 400$ Hz, which is 54° away from the ideal 90°. Fig. 3.5 displays δ^0 for different values of f_c. The considerable deviation of α_s^- from 90° in Fig. 3.3 drives δ^0 in Fig. 3.5 outside the zone for a BCG fault (given in Fig. 1.3). Therefore, R152 is unable to identify the fault type correctly.

The above analysis was presented assuming that the RSC does not saturate and remains in the linear region of operation during the LVRT condition. When the magnitude of the induced

rotor voltage exceeds the RSC's maximum voltage, which happens during more severe faults, the required rotor voltage references exceed the RSC's maximum voltage capacity. In such conditions, the three-phase rotor voltages given to the pulse width modulation (PWM) as reference signals are clipped by the voltage limiter of the RSC control system [62]. Consequently, the magnitude of the undesired $-(2-s)\omega$ frequency component of the voltage generated by the RSC will be smaller than the magnitude of this component when the RSC does not saturate. This condition is similar to when f_c is small and the controller rejects the $-(2-s)\omega$ frequency components. As shown in Fig. 3.3, the deviation of α_s^- from 90° is modest for smaller values of f_c. Therefore, as the magnitude of the induced rotor voltage increases during the saturation mode, the three-phase rotor voltages given to the PWM get clipped further. This situation is analogous to an even smaller f_c, which decreases the deviation of α_s^- from 90° further. As a result, the saturation mode is less severe than the linear mode discussed earlier in terms of the deviation of α_s^- from 90°.

The induced rotor voltage given by (3.2) may include a transient DC component depending on the fault severity and the fault inception angle. As discussed earlier, a DFIG can be analyzed using the superposition principle for the DFIG conditions considered in this section. Therefore, the angle between the negative-sequence current and voltage is determined by the structure and parameters of the negative machine, which are not affected by the transient DC component. It should also be noted that the transient DC component normally decays considerably within the 6-cycle settling time allowed by the 2800 standard for DFIGs.

This section showed (i) why the angle between the negative-sequence current and voltage deviates from its ideal [90°, 100°] range for a DFIG with CVC, (ii) what parameters affect this

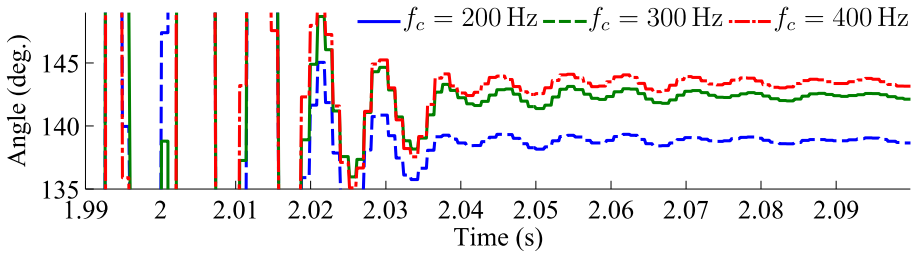

Figure 3.4: α_s^- for a BCG fault with R_f =15 Ω at 50% of line L215.

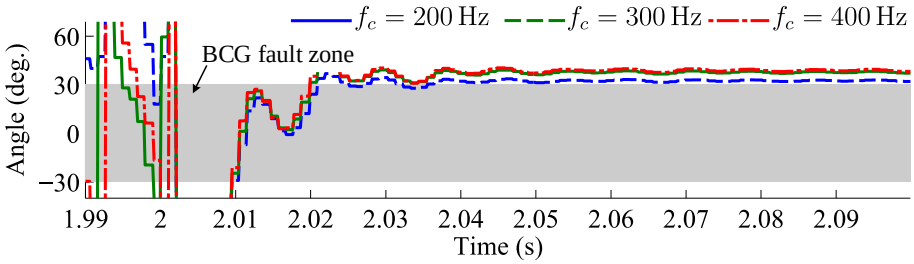

Figure 3.5: δ^0 measured by R152 at the POM for the fault of Fig. 3.4.

deviation, and (iii) how the relays can be negatively impacted by this deviation even though the negative-sequence current angle for a DFIG with CVC is within the extended [90°, 150°] range allowed by the 2800 Standard for DFIGs.

3.3 DCC-Based DFIGs

This section investigates α_s^- for a DFIG with DCC. Similar to the case of CVC, a DCC also results in the flow of negative-sequence current in the rotor winding. The difference is that the negative-sequence current associated with DCC is directly controlled by the RSC control system based on the internal references. These references are normally generated to suppress the second harmonic ETPs caused by the unbalanced fault voltage.

The voltage induced in the rotor given by (3.2) is the sum of two space vectors rotating at different frequencies; thus, the angle between these two vectors keeps changing. The induced rotor

voltage is maximized when this angle becomes zero, when it can be expressed as

$$E_{r,\max} = \underbrace{|s|\frac{L_m}{L_s}|V_s^+|}_{E_{r,\max}^+} + \underbrace{(2-s)\frac{L_m}{L_s}|V_s^-|}_{E_{r,\max}^-} \tag{3.10}$$

in which $E_{r,\max}^+$ and $E_{r,\max}^-$ are the magnitudes of the vectors of the positive- and negative-sequence voltages induced in the rotor, i.e., $\vec{e}_{r,\text{ind}}^+$ and $\vec{e}_{r,\text{ind}}^-$. For a given set of slip and machine parameters in (3.10), $E_{r,\max}$ depends on the magnitude of the stator positive- and negative-sequence voltages. If $E_{r,\max}$ during a grid fault is smaller than the maximum voltage capacity of the RSC, $V_{r,\max}$—which is usually around 0.4 pu [63], [60]—the negative-sequence current remains fully under control by the RSC, and the ETPs can be completely suppressed. Conversely, if $E_{r,\max}$ exceeds the rotor's maximum voltage capacity, the negative-sequence current cannot be perfectly regulated, resulting in only partial suppression of the ETPs. The latter condition occurs when the fault voltage is very small. These two conditions result in fairly different control modes, so the following study of α_s^- is done separately for the full and partial suppression modes of the ETPs.

3.3.1 Full Suppression of ETPs

The electromagnetic torque of a DFIG during unbalanced faults is given by (3.11) [7].

$$\begin{aligned} &T_e = (3p/2)\,\text{Im}(\overline{\vec{\psi}}_s \vec{i}_s) = \\ &(3p)\,\text{Im}(\overline{\Psi}_s^+ I_s^+ + \overline{\Psi}_s^- I_s^- + \overline{\Psi}_s^+ I_s^- e^{j2\omega t} + \overline{\Psi}_s^- I_s^+ e^{-j2\omega t}) \end{aligned} \tag{3.11}$$

p is the number of pair poles; ψ_s is the stator flux vector, and Ψ_s is its phasor. $\bar{(\cdot)}$ denotes the

complex conjugate of a number. The two oscillatory 2ω components in (3.11) are caused by the interaction between the positive- and negative-sequence quantities. A constant torque can be obtained if these two oscillatory terms in (3.11) are forced to zero. This condition is achieved via the relation in (3.12) for the stator sequence currents and voltages [64, 65].

$$\frac{I_s^-}{V_s^-} = \frac{I_s^+}{V_s^+} \tag{3.12}$$

This relation indicates that α_s^- equals the phase difference between the stator's positive-sequence current and voltage, denoted by α_s^+. If the IBR operates at unity power factor (PF), i.e., I_s^+ is totally active, $\alpha_s^+ = 0$, and so α_s^- is also zero irrespective of the fault condition, including its type. If the PF is zero and the IBR generates a fully reactive I_s^+, $\alpha_s^+ = \alpha_s^- = 270°$. For any other PF, α_s^+ and α_s^- remain between 270° and 0 in the fourth quadrant. As a result, α_s^- maintains a minimum deviation of around 180° from the ideal [90°,100°] range in the counterclockwise direction. Consequently, the relays' phase selection elements are not able to determine the faulty phase(s) correctly. Moreover, the deviation of α_s^- is so large that it falls even outside the expanded [90°, 150°] range considered by the 2800 Standard for DFIGs [12].

As a representative case for the above condition, consider a BCG fault with $R_f = 25\ \Omega$ at 20% of line L23 from bus B2 in Fig. 3.1. The DFIGs operate at $s = +\ 0.03\%$ before the fault. The fault decreases the positive-sequence voltage by 0.20 pu and increases the negative-sequence voltage from zero to 0.12 pu. For these two voltages and the DFIG parameters given in Table A.1, $E_{r,\max}$ in (3.10) is 0.26 pu, which is below the 0.4-pu $V_{r,\max}$ of the RSC. Therefore, the ETPs are fully suppressed.

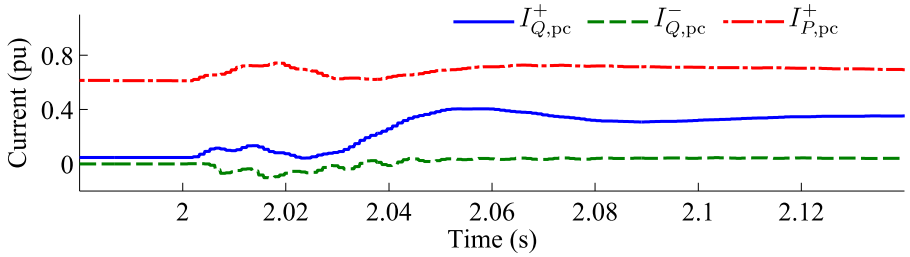

Figure 3.6: Active and reactive currents at the DFIG POC for a BCG fault with $R_f = 25\ \Omega$ at 20% of line L23 from bus B2.

As discussed above, the negative-sequence current in this condition depends on how the DFIG controls its positive-sequence current. The default mode considered for an IBR's positive-sequence LVRT current in the 2800 Standard prioritizes the reactive component, but the Standard does not specify the exact magnitudes of the positive-sequence reactive and active currents. In this case study, we prioritize the reactive component of I^{+} and use the VDE GC (with K-factor equal to 2) to determine the setpoints for the active and reactive components of I^{+} [2]—a method mentioned by the 2800 Standard as an example for setting the current magnitude. Fig. 3.6 displays the DFIG's active and reactive currents, denoted by P and Q in the subscripts, respectively. In this figure, $I^{+}_{P,\mathrm{pc}}$ and $I^{+}_{Q,\mathrm{pc}}$ are $+0.7$ pu and $+0.4$ pu, which correspond to PF $= 0.87$ for the positive-sequence circuit. With this PF, α_s^{+} settles at 335° in Fig. 3.7. This figure confirms the above conclusion that when the ETPs are fully suppressed, α_s^{-} is approximately equal to α_s^{+} when the initial fault transients fade out. α_s^{-} is more than 200° away from its ideal [90°,100°] range.

The variations of α_s^{-} are reflected in the $I^{-}_{Q,\mathrm{pc}}$ curve of Fig. 3.6. During the first 20 ms of the fault, α_s^{-} is between 90° and 180°, so the DFIG consumes negative-sequence reactive current, hence the negative $I^{-}_{Q,\mathrm{pc}}$ in Fig. 3.6. Afterwards, α_s^{-} moves beyond 180° and the DFIG generates a small negative-sequence reactive current—a violation of the 2800 Standard and most GCs, e.g., [2].

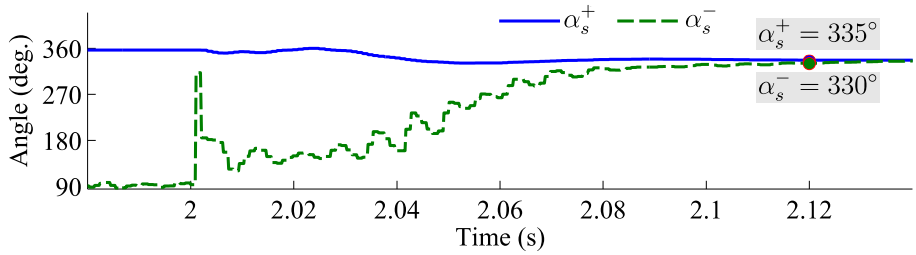

Figure 3.7: α_s^+ and α_s^- at the POC for the fault of Fig. 3.6.

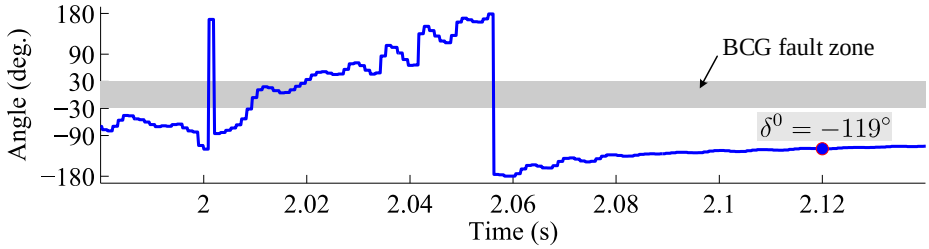

Figure 3.8: δ^0 measured by R152 at the POM for the fault of Fig. 3.6.

The problems in this scenario are not limited to the violation of Standards and GCs. As shown in Fig. 3.8, the unconventional phase angle between the DFIG's negative-sequence current and voltage drives δ^0 out of its expected zone for a BCG fault, defined in Fig. 1.3. δ^0 enters the shaded area in Fig. 3.8 temporarily in the beginning of the fault but passes through it quickly. The subsequent values for δ^0 indicates a CG or an ABG fault before finally settling at $-119°$, which is inside the zone for a BG or CAG fault in Fig. 1.3. Consequently, R152 in Fig. 3.1 fails to detect that the fault is BCG.

3.3.2 Partial Suppression of ETPs

When the induced rotor voltage is larger than $V_{r,\max}$ and the ETPs can be suppressed only partially, the relation between the stator's negative-sequence current and voltage is given by (3.13) if the rotor's resistance is neglected [65].

$$I_s^- = \frac{j}{\omega\sigma L_s}\left(V_s^- - \frac{L_m}{L_r(2-s)}|V_r^-|e^{j\measuredangle V_r^-}\right) \tag{3.13}$$

$|V_r^-|$ and $\measuredangle V_r^-$ in (3.13) are given by (3.14) and (3.15), respectively [64], [48].

$$|V_r^-| = V_{r,\max} - E_{r,\max}^+ \tag{3.14}$$

$$\measuredangle V_r^- = \underbrace{\measuredangle\left(1 - j\omega\sigma L_s\frac{I_s^+}{V_s^+}\right)}_{\varphi} + \measuredangle V_s^- \tag{3.15}$$

Replacing $\measuredangle V_r^-$ in (3.13) with (3.15) yields α_s^- as in (3.16).

$$\alpha_s^- = 90^\circ + \underbrace{\measuredangle\left(|V_s^-| - \underbrace{\frac{L_m}{L_r(2-s)}|V_r^-|e^{j\varphi}}_{\gamma}\right)}_{\beta} \tag{3.16}$$

This equation indicates that α_s^- depends on the slip, the stator's negative-sequence voltage (which is the same as the POC voltage), the magnitude of the RSC's negative-sequence voltage, the angle difference between the stator's positive-sequence current and voltage (embedded within φ), and different machine parameters.

If the suppression of ETPs is not intended, the setpoint for V_r^- is set to zero in the control system. Thus, since $|V_s^-|$ is a positive real number, β becomes zero in (3.16), and α_s^- is equal to the ideal value of 90°. A non-zero V_r^- intended to suppress ETPs, however, moves α_s^- away from this ideal value. The largest deviation of α_s^- from 90° occurs when β in (3.16) is 180°. This

condition can happen when the DFIG's positive-sequence PF becomes zero by generating a purely reactive I_s^+, which makes $(1 - j\omega\sigma L_s I_s^+ / V_s^+)$ in (3.15) a positive real number for the typical values of machine parameters (such as those in Table A.1) and $|V_s^+|$ during unbalanced faults. This would make φ in (3.15) and (3.16) zero. For such a condition, the typical values of $|V_s^-|$ caused by fault, s, $|V_r^-|$ setpoint (depending on the intended degree of ETP suppression), and machine parameters make $|V_s^-| < |\gamma|$ in (3.16) quite possible. If this condition holds, β in (3.16) becomes 180°, making $\alpha_s^- = 270°$; i.e., the farthest from its ideal value of 90°. For other values of DFIG positive-sequence PF, α_s^- varies between the 90° and 270° boundaries derived above. Such large deviations of α_s^- from 90° can render available phase selection methods ineffective. They also make the DFIG non-compliant with the 2800 Standard [12].

As a representative case, consider a BCG fault with $R_f = 20\ \Omega$ at 50% of line L215. The fault results in a 0.36-pu positive-sequence voltage drop and 0.2-pu negative-sequence voltage rise at the POC of the DFIG, which operates at $s = 8\%$. These voltages and slip along with the machine parameters in Table A.1 and (3.10) yield $E_{r,max} = 0.44$ pu, which is above the maximum voltage of the RSC. Thus, the ETPs can be suppressed only partially.

The DFIG's active and reactive currents are depicted in Fig. 3.9. Contrary to the case shown in Fig. 3.6, the DFIG consumes a small negative-sequence reactive current. This is caused by α_s^- in Fig. 3.10, which lags 180°. Unlike Fig. 3.7, α_s^- does not follow α_s^+ in Fig. 3.10 because the ETPs are not fully suppressed, and α_s^- is given by (3.16), not (3.12). The undesired α_s^-—which is outside the wider [90°, 150°] range considered for DFIGs in the 2800 Standard—pushes δ^0 of R152 outside the zone for BCG faults in Fig. 3.11. Thus, the fault type is not correctly detected.

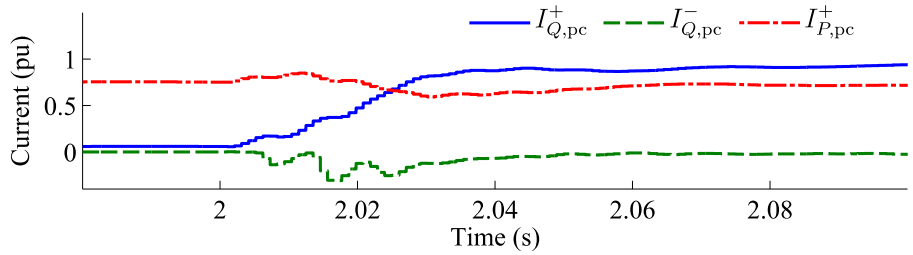

Figure 3.9: Active and reactive currents at the DFIG POC for a BCG fault with $R_f = 20\ \Omega$ at 50% of line L215.

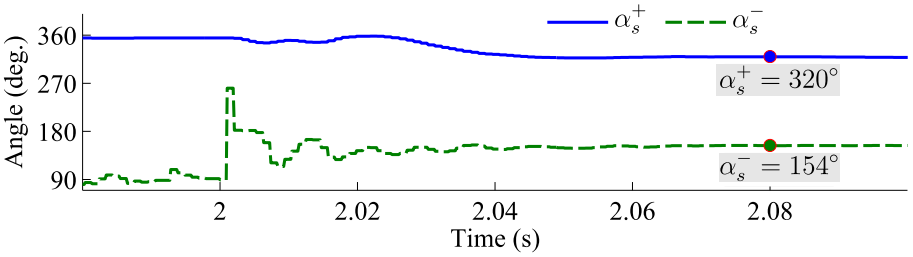

Figure 3.10: α_s^+ and α_s^- at the POC for the fault of Fig. 3.9.

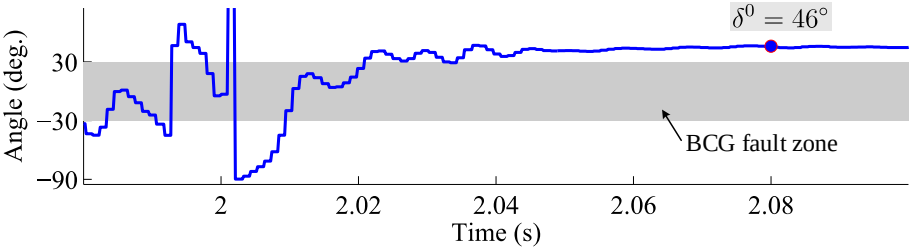

Figure 3.11: δ^0 measured by R152 at the POM for the fault of Fig. 3.9.

This section showed that the available DFIG control methods for suppression of ETPs during unbalanced LVRTs could move the angle between the negative-sequence current and voltage well beyond even the extended [90°, 150°] range allowed by the 2800 Standard for DFIGs. This section also showed that such a deviation in the angles naturally impacted the relays negatively.

3.4 Proposed Solution

It is easy to regulate the phase difference between the negative-sequence current and voltage of a DFIG at 90° and so obviate the need in future revisions of the IEEE 2800 Standard for the previously mentioned undesired exception currently considered for DFIGs. The discussion below (3.16) demonstrated that a DCC scheme for the RSC along with a zero setpoint for V_r^- makes $\alpha_s^- = 90°$. However, this ideal α_s^- is achieved at the expense of unsuppressed ETPs. Large ETPs can cause mechanical stress and damage the coupling shaft of a DFIG [44], [49], [66], so eliminating the ETPs is always considered advantageous [7]. Thus, the ideal—and more challenging— objective would be achieving the desired angle for the negative-sequence current while the ETPs are suppressed to the maximum extent possible. To meet this objective, the following develops a new DCC scheme not for the RSC but for the GSC. The RSC control is left intact, i.e., the DFIG manufacturer can use either the well-established CVC scheme or the DCC method described in Section 3.1 to suppress the ETPs.

During normal operation, only the positive-sequence control loop in the dq^+ SRF is active for the GSC. Once the DFIG enters an unbalanced LVRT mode, the negative-sequence control loop is also activated, regulating the d and q axis of the GSC in the dq^- SRF, denoted by I_{gd}^- and I_{gq}^-, respectively. The setpoints for these two currents, I_{gd}^{-*} and I_{gq}^{-*}, are controlled such that the sum of the negative-sequence current from the GSC and stator at the POC has the proper angle and magnitude. The angle of the POC negative-sequence current must lead the respective voltage by an angle inside the [90°, 100°] range [12]. For the sake of simplicity, we choose $\alpha_{\text{pc}}^- = 90°$, but the

solution in this section is applicable to any α_{pc}^{-} within the [90°, 100°] range.

The 2800 Standard does not determine a specific magnitude for the negative-sequence current, leaving it to the transmission system owner. A common approach to determine the magnitude of I_{pc}^{-} is to use the K-factor diagram of [2]—which has been mentioned by the 2800 Standard as well. In this method, as discussed in Chapter 1, the incremental positive- and negative-sequence reactive currents, $\Delta I_{Q,\text{pc}}^{\pm}$, are determined based on the respective incremental sequence voltages, $\Delta V_{\text{pc}}^{\pm}$, using the diagram in Fig. 1.2. If the current obtained through this diagram exceeds the maximum current that the wind turbine can generate, the two sequence currents are reduced preferably at the same rate until the phase currents meet the wind turbine's maximum current generation capacity. We use the same approach in the following to determine the target magnitude for I_{pc}^{-}. For the sake of simplicity and without loss of generality, we assume that the pre-fault reactive current is zero, so $I_{Q,\text{pc}}^{-} = \Delta I_{Q,\text{pc}}^{-}$. The LV side of the turbine-level transformer is considered as the POC according to the IEEE 2800 Standard.

To achieve $\alpha_{\text{pc}}^{-}=90°$, the GSC's negative-sequence current must cancel any active or capacitive components of the stator negative-sequence current, I_s^{-}. I_s^{-} can be either measured or estimated using (3.1). Selecting V_s^{-} as the reference phasor, this translates to compensating for any real and negative imaginary parts of I_s^{-}. Once α_{pc}^{-} is regulated at 90°, any remaining current capacity of the GSC is allocated to reach the reactive current magnitudes given by Fig. 1.2. For the GSC, the priority is given to egulating the dc-link voltage and the negative-sequence reactive current because the RSC is capable of generating the required positive-sequence reactive current through the stator. The following explains the methodology to find the GSC's negative-sequence current reference, I_g^{-*},

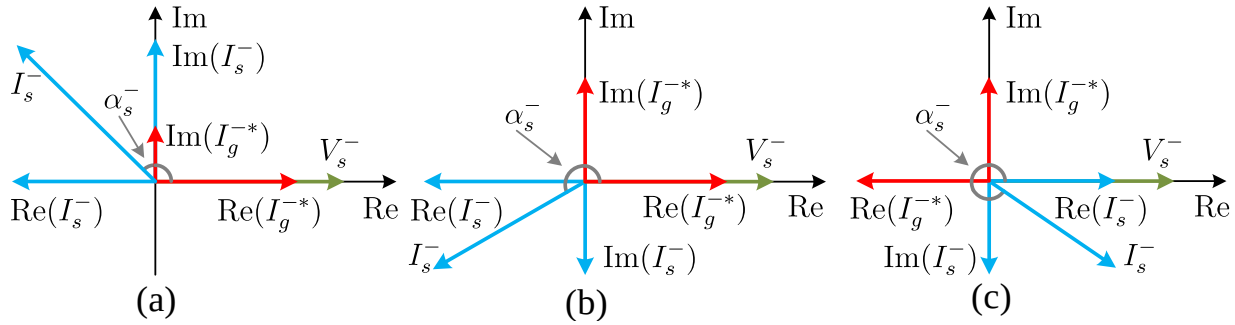

Figure 3.12: Negative-sequence current of the stator and the GSC's negative-sequence current setpoints for (a) Condition 1, (b) Condition 2, and (c) Condition 3.

for the possible combinations of real and imaginary parts for I_s^-, referred to as Conditions 1, 2, and 3 (considering V_s^- as the reference phasor).

Condition 1 $(\mathbf{90^\circ < \alpha_s^- < 180^\circ})$

Sections 3.2 and 3.3 showed that $90^\circ < \alpha_s^- < 180^\circ$ when the RSC control is CVC or DCC with partial suppression of the ETPs. Fig. 3.12(a) illustrates this condition, which results in a negative real and a positive imaginary part for I_s^-. To cancel the real component of I_s^- in Fig. 3.12(a) and make $\alpha_{\mathrm{pc}}^- = 90^\circ$,

$$\mathrm{Re}(I_g^{-*}) = -\mathrm{Re}(I_s^-) \tag{3.17}$$

This equation determines the active component of the GSC's negative-sequence current. Depending on the slip, machine parameters, type of the RSC control system, and the voltage dip level, the GSC may be able to fully or partially cancel out $\mathrm{Re}(I_s^-)$. Section 3.5 will present a detailed analysis that shows $\mathrm{Re}(I_s^-)$ can be cancelled for all realistic conditions of a practical DFIG.

When the GSC completely cancels $\mathrm{Re}(I_s^-)$, the remaining capacity of the GSC is directed towards achieving the desired magnitude for I_{pc}^-. Similar to what was stated in the above paragraph

about $\mathrm{Re}(I_s^-)$, Section 3.5 will show that the GSC of a practical DFIG has enough capacity to meet this objective. To regulate the current magnitude, the proposed method first compares the negative-sequence reactive current from the stator (i.e., $\mathrm{Im}(I_s^-)$ in Fig. 3.12(a)) with the negative-sequence current required by the GC at the POC, $I_{Q,\mathrm{pc}}^-$. If $\mathrm{Im}(I_s^-)$ is greater than $I_{Q,\mathrm{pc}}^-$, the remaining capacity of the GSC is used to reduce $\mathrm{Im}(I_g^-)+\mathrm{Im}(I_s^-)$ to $I_{Q,\mathrm{pc}}^-$ by generating a capacitive I_g^-. On the other hand, if $\mathrm{Im}(I_s^-)$ is less than $I_{Q,\mathrm{pc}}^-$, the remaining capacity of the GSC is used to increase $\mathrm{Im}(I_g^-)+\mathrm{Im}(I_s^-)$ to $I_{Q,\mathrm{pc}}^-$ by generating an inductive I_g^-. If the remaining capacity of the GSC is not sufficient for this purpose, $I_{Q,\mathrm{pc}}^-$ is scaled down to the maximum capacity of the DFIG, which is dictated by the GSC's maximum current limit. As mentioned earlier, the scaling down of the reference currents to the maximum capacity of an IBR is allowed by the GCs and is commonly used, particularly when the K-factor is large [2]. As a result, $\mathrm{Im}(I_g^{-*})$ can be derived as

$$\mathrm{Im}(I_g^{-*}) = \rho_1 I_{Q,\mathrm{pc}}^- - \mathrm{Im}(I_s^-) \tag{3.18}$$

where ρ_1 is the scaling factor for Condition 1. When $\mathrm{Im}(I_s^-) \geq I_{Q,\mathrm{pc}}^-$, ρ_1 is 1. When $\mathrm{Im}(I_s^-) < I_{Q,\mathrm{pc}}^-$, ρ_1 is given by (3.19) to maximize the utilization of the GSC's current generation capacity.

$$\rho_1 = \frac{\sqrt{I_{g,\max}^2 - \mathrm{Re}(I_g^+)^2 - \mathrm{Re}(I_s^-)^2} + \mathrm{Im}(I_s^-)}{I_{Q,\mathrm{pc}}^-} \tag{3.19}$$

$I_{g,\max}$ and $\mathrm{Re}(I_g^+)$ in (3.19) are the GSC's maximum current limit and the real part of the GSC's positive-sequence current with respect to V_s^+, which is used to keep the dc-link voltage within the acceptable limits.

The current setpoints in (3.17) and (3.18) are obtained considering V_s^- as the reference phasor. However, the setpoints for the GSC's control system, i.e., I_{gd}^{-*} and I_{gq}^{-*}, should be calculated in the dq^- SRF. The reference in this frame is the positive-sequence voltage at the GSC terminal—i.e., V_s^+, whose angle is determined by the phase-locked loop (PLL). It can be shown that I_{gd}^{-*} and I_{gq}^{-*} are attainable in the dq^- SRF using the projection of the I_g^- given by (3.17) and (3.18)—i.e., $I_g^{-*} = \sqrt{\mathrm{Re}(I_g^{-*})^2 + \mathrm{Im}(I_g^{-*})^2}$—onto V_s^+, as in (3.20) and (3.21), respectively.

$$I_{gd}^{-*} = |I_g^{-*}| \cos\left(\mathrm{atan}\left(\frac{\mathrm{Im}(I_g^{-*})}{\mathrm{Re}(I_g^{-*})}\right) + \measuredangle V_s^- - \measuredangle V_s^+\right) \tag{3.20}$$

$$I_{gq}^{-*} = |I_g^{-*}| \sin\left(\mathrm{atan}\left(\frac{\mathrm{Im}(I_g^{-*})}{\mathrm{Re}(I_g^{-*})}\right) + \measuredangle V_s^- - \measuredangle V_s^+\right) \tag{3.21}$$

Following this procedure, a DFIG will be able to comply with the negative-sequence current requirements of [2] during LVRT.

Condition 2 ($\mathbf{180^\circ < \alpha_s^- < 270^\circ}$)

Section 3.3 showed that for a DFIG with DCC-based RSC control, $180^\circ < \alpha_s^- < 270^\circ$ (i.e., both $\mathrm{Re}(I_s^-)$ and $\mathrm{Im}(I_s^-)$ can become negative) when the ETPs are partially suppressed (Fig. 3.12(b)). To obtain $\alpha_{\mathrm{pc}}^- = 90^\circ$ under this condition, both $\mathrm{Re}(I_s^-)$ and $\mathrm{Im}(I_s^-)$ in Fig. 3.12(b) have to be eliminated by the GSC current. Therefore, similar to the last subsection, $\mathrm{Re}(I_g^{-*})$ must be equal to $-\mathrm{Re}(I_s^-)$, as given in (3.17). Further, $\mathrm{Im}(I_g^{-*})$ must be regulated such that $\mathrm{Im}(I_s^-)$ in Fig. 3.12(b) is canceled out and $\mathrm{Im}(I_g^-) + \mathrm{Im}(I_s^-)$ equals the $I_{Q,\mathrm{pc}}^-$ given by Fig. 1.2. Section 3.5 will show that the GSC of a practical DFIG can eliminate both $\mathrm{Re}(I_s^-)$ and $\mathrm{Im}(I_s^-)$ in Fig. 3.12(b) and prevent a

resistive/capacitive negative-sequence current for the DFIG. However, the remaining capacity of the GSC might not be sufficient to match I_{pc}^{-} to the $I_{Q,\text{pc}}^{-}$ given by Fig. 1.2 especially when the K-factor is large. If this is the case, the target negative-sequence current magnitude determined by Fig. 1.2 is scaled down, as permitted by the GC [2]. Consequently, $\text{Im}(I_g^{-*})$ is given by

$$\text{Im}(I_g^{-*}) = \rho_2 I_{Q,\text{pc}}^{-} - \text{Im}(I_s^{-}) \tag{3.22}$$

in which ρ_2 is the scaling factor for Condition 2. If the GSC's capacity is sufficient to raise $\text{Im}(I_g^{-}) + \text{Im}(I_s^{-})$ to $I_{Q,\text{pc}}^{-}$, ρ_2 is 1; otherwise ρ_2 is given by (3.23) to maximize utilization of the GSC's current generaztion capacity.

$$\rho_2 = \frac{\sqrt{I_{g,\max}^2 - \text{Re}(I_g^{+})^2 - \text{Re}(I_s^{-})^2} - \text{Im}(I_s^{-})}{I_{Q,\text{pc}}^{-}} \tag{3.23}$$

As a result, once $\text{Re}(I_g^{-*})$ and $\text{Im}(I_g^{-*})$ are derived using (3.17) and (3.22), respectively, I_{gd}^{-*} and I_{gq}^{-*} can be obtained in the dq^{-} SRF using (3.20) and (3.21), respectively.

Condition 3 ($\mathbf{270^\circ < \alpha_s^{-} < 360^\circ}$)

Section 3.3 showed that $270^\circ < \alpha_s^{-} < 360^\circ$ (i.e., the real and imaginary parts of I_s^{-} become positive and negative, respectively) when the DCC-based control of the RSC fully suppresses the ETPs (Fig. 3.12(c)). Similar to Condition 2, to make $\alpha_{\text{pc}}^{-} = 90^\circ$, both $\text{Re}(I_s^{-})$ and $\text{Im}(I_s^{-})$ must be eliminated by the GSC current. Therefore, $\text{Re}(I_g^{-*})$ and $\text{Im}(I_s^{-})$ are obtained using (3.17) and (3.22). Afterwards, I_{gd}^{-*} and I_{gq}^{-*} can be calculated using (3.20) and (3.21), respectively.

On this basis, not only does the proposed method maximize the suppression of the ETPs, it also keeps the angle of the negative-sequence current at the POC equal to 90°, thereby eliminating the need for the previously mentioned exemption for DFIGs in the the IEEE 2800 Standard [12]. This method also complies with the negative-sequence current requirements of [2], which is the most stringent GC in terms of the LVRT requirements. Furthermore, this method is independent of the type/target of the control used for the RSC—which could be either the two control schemes mentioned in Section 3.1 or the other schemes discussed in [4].

Fig. 3.13 illustrates the overall structure of the proposed control scheme for the GSC, which is activated during unbalanced LVRT conditions. In this figure, L_{gf} is the inductance of the GSC filter. Fig. 3.13(a) shows the positive-sequence control loop in the dq^+ SRF. Maintaining the dc-link voltage within the acceptable limits always has the highest priority. The reference for I_{gd}^{+} depends on the rotor speed. During the super-synchronous speed operation, the dc-link voltage increases, and the chopper circuit limits this voltage to 1.1 pu. Therefore, there is no need for the GSC control system to regulate the dc-link voltage during the super-synchronous speed operation, and so the reference for the positive-sequence active current, I_{gd}^{+*}, is set to zero in this mode. During the sub-synchronous speed operation, however, the dc-link voltage may drop, and so the GSC control system will be responsible for regulating this voltage. In this condition, the dc-link voltage regulation has the highest priority for the GSC control, and the reference for I_{gd}^{+} is calculated such that this voltage is maintained at 1 pu. If the GSC has excess capacity afterregulating the dc-link voltage and generating the exact setpoints calculated above for the negative-sequence current, that capacity is allocated to assisting the RSC in meeting the positive-sequence reactive current requirement of the

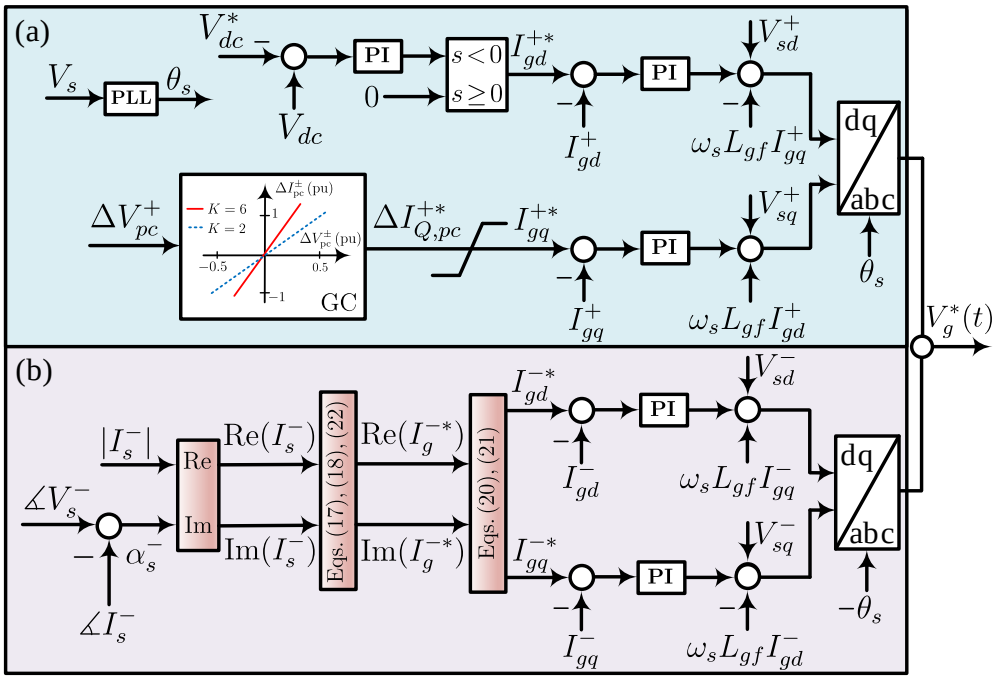

Figure 3.13: Schematic diagram of the proposed control scheme for the GSC, (a) positive-sequence control loop, (b) negative-sequence control loop.

GC. By doing so, the GSC allows freeing up a larger capacity of the RSC to maximize the ETP suppression. Fig. 3.13(b) displays how the above derivations for the negative-sequence current can be implemented.

It is important to note that once the GSC references for the positive-sequence active current (intended to regulate the dc-link voltage) and the negative-sequence current (intended to make $\alpha_{\text{pc}}^- = 90°$) are calculated, the remaining capacity of the GSC for the positive-sequence reactive current generation is quite small in practical DFIGs. Therefore, the change in the angle of the stator's negative-sequence current due to the correction of the RSC setpoints is very small. As a result, α_{pc}^- remains within the [90°, 100°] range that the 2800 standard allows for all types of IBRs. In other words, there is no practical need to change the GSC references after the RSC corrections.

3.5 Feasibility Region of the Proposed Method

This section investigates the conditions under which the proposed method is able to regulate the POC negative-sequence current to move α_{pc}^{-} close to 90° to comply with the IEEE 2800 Standard without the need for an exemption for DFIGs and also satisfy the *K*-factor diagram of Fig. 1.2. Fulfilment of these objectives mainly depends on the GSC's maximum current. In a DFIG with the nominal slip range of ±30%, the converters are rated at about 35% of the nominal power. Therefore, the GSC current rating of a DFIG is about 0.35 pu. As the power electronic switches of DFIG converters typically provide a minimum fault current of 150% of the rated current for DFIGs [43, 67], the GSC's maximum current is at least 0.525 pu. This maximum current is equal to or below the maximum current of GSC in practical DFIGs. For example, in the nameplate of an actual 1.5-MW DFIG shown in [68], the 1-second short-circuit current of the GSC is as high as 265% of the GSC's rated continuous current. Thus, the 150% maximum current considered in this paper for the GSC is below the maximum currents used by actual DFIGs. This issue is confirmed by several other references as well [43], [69]. The following finds the feasibility region of the proposed method for a GSC with a maximum current of 0.525 pu for different RSC control systems. The following finds the feasibility region of the proposed method for a GSC with a maximum current of 0.525 pu for different RSC control systems.

3.5.1 CVC-Based DFIG

The following investigates the feasibility region of the proposed solution for CVC-based DFIGs. As mentioned in Section 3.4, when $\mathrm{Re}(I_s^-) < 0$ and $\mathrm{Im}(I_s^-) > 0$, the proposed solution first makes $\alpha_{\mathrm{pc}}^- = 90^\circ$ by canceling out $\mathrm{Re}(I_s^-)$ in (3.17), and then adjusts $\mathrm{Im}(I_g^-)$ to follow (3.18) to meet the diagram in Fig. 1.2. Thus, the proposed solution is feasible when the GSC can meet these two objectives. (3.17) and (3.18) depend on $\mathrm{Re}(I_s^-)$ and $\mathrm{Im}(I_s^-)$, respectively, which can be expressed as

$$\mathrm{Re}(I_s^-) = |I_s^-|\cos(\alpha_s^-) \tag{3.24}$$

$$\mathrm{Im}(I_s^-) = |I_s^-|\sin(\alpha_s^-) \tag{3.25}$$

where $|I_s^-|$ is given by (3.8). The worst-case scenario for the GSC is when $|I_s^-|$ in (3.24) and (3.25) is maximum. It can be shown that $|I_s^-|$ in (3.8) is maximum when $|V_s^-|$ and the slip are maximum. The maximum negative-sequence voltage at the POM, V_{pm}^-, is 0.5 pu—which occurs for a bolted line-to-line (LL) fault at the POM. However, due to the reactance of the plant's main transformer and turbine transformer along with the collector system's impedance at the medium-voltage level, $|V_s^-|$ at the POC is normally at least 0.1 pu smaller than V_{pm}^-. Thus, it is safe to consider $|V_s^-| = 0.4$ pu for the worst-case scenario. The maximum slip is also $\pm 30\%$.

Using (3.8), (3.24) and (3.25), Fig. 3.14 shows $\mathrm{Re}(I_s^-)$ and $\mathrm{Im}(I_s^-)$ with respect to f_c for $V_s^- = 0.4$ and $s = -30\%$. Fig. 3.14 demonstrates that both $\mathrm{Re}(I_s^-)$ and $\mathrm{Im}(I_s^-)$ decrease commensurate with f_c. As the largest $\mathrm{Re}(I_s^-)$, which corresponds to $f_c = 200$ Hz, is below the worst-case maximum current for the GSC (i.e., 0.525 pu), the GSC can make $\alpha_{\mathrm{pc}}^- = 90^\circ$. Meanwhile, $\mathrm{Im}(I_s^-)$ is also large

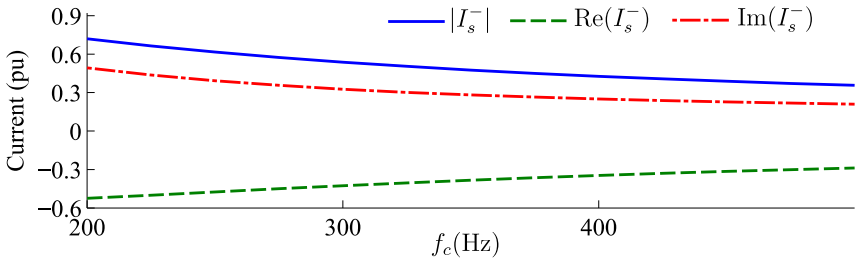

Figure 3.14: Stator current versus f_c for $V_s^- = 0.4$ pu and $s = -30\%$.

enough to independently meet the $I_{Q,\mathrm{pc}}^-$ determined by Fig. 1.2 with a proper scaling factor given by (3.19). If $f_c > 200$ Hz and so $\mathrm{Re}(I_s^-) < 0.525$ pu, the remaining capacity of the GSC can be used to reinforce $\mathrm{Im}(I_s^-)$. Thus, the GSC can make $\alpha_{\mathrm{pc}}^- = 90^\circ$ and satisfy the diagram of Fig. 1.2 for all LVRT conditions.

3.5.2 DCC-Based DFIG

The following investigates the feasibility region of the proposed scheme for DCC-based DFIGs for the two operation modes.

Full Suppression of ETPs

The rotor current of a DFIG depends on the difference between the induced rotor voltage and the maximum voltage that the RSC can generate. During full suppression of the ETPs, since the negative-sequence voltage capacity of the RSC is enough to encounter the negative-sequence voltage induced in the rotor, the rotor's negative-sequence current will be negligible. Considering this negligible I_r^-, the stator's negative-sequence current according to (3.1) will be proportional to $V_s^-/\omega L_s$. For the largest V_s^-, i.e., 0.4 pu discussed above, and L_s in Table A.1, $V_s^-/\omega L_s = 0.13$ pu, which is far below the GSC's 0.525 pu maximum current capacity. Therefore, the GSC can fix α_{pc}^-

at 90° and satisfy the K-factor diagram.

Partial Suppression of ETPs

As mentioned in Section 3.4, during partial suppression of ETPs, $\mathrm{Re}(I_s^-)$ is negative while $\mathrm{Im}(I_s^-)$ can be either positive or negative. For such a condition, the proposed solution is feasible when it can first make $\alpha_{\mathrm{pc}}^- = 90^\circ$ by canceling out $\mathrm{Re}(I_s^-)$ in (3.17) and then adjust $\mathrm{Im}(I_g^-)$ to follow (3.18) or (3.22), depending on the sign of $\mathrm{Im}(I_s^-)$. (3.17), (3.18), and (3.22) depend on I_s^-, which can be obtained using (3.10), (3.13), and (3.14) as in (3.26).

$$I_s^- = \frac{j}{\omega\sigma L_s}\left(V_s^- - \frac{L_m e^{j\measuredangle V_r^-}}{L_r(2-s)}\left(V_{r,\max} - |s|\frac{L_m}{L_s}|V_s^+|\right)\right) \tag{3.26}$$

Based on (3.15), $\measuredangle V_r^-$ in (3.26) depends on the angle between V_s^+ and I_s^+, i.e., the DFIG's positive-sequence PF. Numerical analysis of (3.26) shows that for a given set of realistic machine parameters, $|I_s^-|$ is maximized when PF=0. It can also be demonstrated that $|I_s^-|$ peaks during LL faults for which $|V_s^-|$ is maximum. Assuming PF=0 at the stator terminals, Fig. 3.15 depicts $\mathrm{Re}(I_s^-)$ and $\mathrm{Im}(I_s^-)$ versus $|V_s^-|$ and the slip for LL faults and $V_{r,\max} = 0.4$ pu. $\mathrm{Re}(I_s^-)$ in Fig. 3.15 is always negative while $\mathrm{Im}(I_s^-)$ can be positive or negative, which corresponds to the conditions discussed in Section 3.4 for partial suppression of ETPs. $|\mathrm{Re}(I_s^-)|$ is proportional to the negative-sequence voltage and reaches 0.13 pu for $|V_s^-| = 0.4$ pu and $s = 0$ in Fig. 3.15(a). This 0.13-pu maximum is well below the GSC's worst-case scenario 0.525 pu current limit, and so it can be easily eliminated by the GSC.

Once $\mathrm{Re}(I_s^-)$ is overcome and $\alpha_{\mathrm{pc}}^- = 90^\circ$, the GSC follows (3.18) or (3.22) depending on the

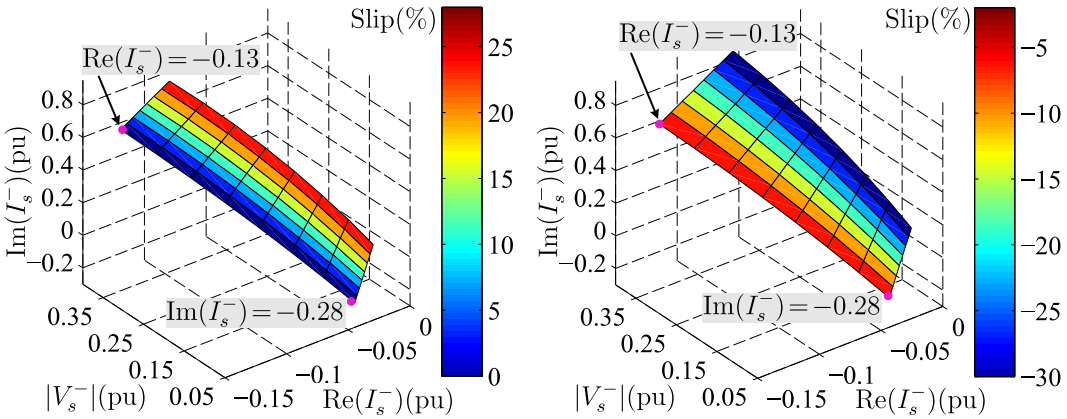

Figure 3.15: Re(I_s^-) and Im(I_s^-) versus $|V_s^-|$ and slip for K-factor=2, (a) Sub-synchronous speed, (b) Super-synchronous speed.

sign of Im(I_s^-) to regulate the magnitude of $I_{Q,\text{pc}}^-$. Since the largest $|\text{Re}(I_s^-)|$ in Fig. 3.15 is 0.13 pu and the GSC's current limit is at least 0.525 pu, the GSC has a minimum of 0.395 pu current capacity to compensate for any difference between the $I_{Q,\text{pc}}^-$ required by Fig. 1.2. The worst-case scenario happens for the largest negative Im(I_s^-) in Fig. 3.15, which is -0.28 pu. Thus, even for the worst condition, the GSC can increase the magnitude of $I_{Q,\text{pc}}^-$ to $0.395-0.28=0.115$ pu, which is more than enough for the relay elements that rely on negative-sequence quantities. This magnitude can also meet [2] using a proper scaling factor given by (3.19) or (3.23).

3.6 Performance Evaluation

The performance of the proposed solution was investigated extensively for various DFIG and LVRT conditions, and promising results were obtained. The following examines this performance for the three case studies of Sections 3.2 and 3.3.

3.6.1 CVC-Based DFIG

Consider the BCG fault studied at the end of Section 3.2. That case is repeated for CVC-based DFIGs equipped with the proposed control scheme for the GSC. The fault decreases the positive-sequence voltage by 0.4 pu and increases the negative-sequence voltage by 0.2 pu at the DFIGs' POC. For K=2 in Fig. 1.2, the positive- and negative-sequence reactive currents required at the POC are 0.8 pu (capacitive) and 0.4 pu (inductive), respectively. Fig. 3.16 shows different components of the stator, GSC, and POC currents for $f_c = 400$ Hz, i.e., the worst-case f_c in terms of α_s^- in Fig. 3.4. In Fig. 3.16(a), the sum of the stator's and GSC's positive-sequence reactive currents yields $I^+_{Q,\text{pc}} = 0.81$ pu. This sum for the negative-sequence currents gives $I^-_{Q,\text{pc}} = -0.4$ pu in Fig. 3.16(b). Both $I^+_{Q,\text{pc}}$ and $I^-_{Q,\text{pc}}$ match the above-mentioned reactive current required by the diagram in Fig. 1.2. The DFIG also generates 0.79 pu of active positive-sequence current (Fig. 3.16(c)).

For different values of f_c, Fig. 3.17 shows α^-_{pc} at the POC and δ^0 at the POM (i.e., R152's location). Contrary to Fig. 3.4, α^-_{pc} in Fig. 3.17(a) enters the ideal [90°, 100°] range within two cycles after the fault inception. Thus, a DFIG with the proposed control scheme can meet the 2800 Standard if the future revisions of the Standard remove the current exemption considered for DFIGs. In addition, the α^-_{pc} of Fig. 3.17(a) keeps δ^0 inside the shaded area that indicates a BCG fault in Fig. 3.17(b). Therefore, R152 can correctly determine the fault type and prevent the problem in Fig. 3.5.

One of the challenging LVRT conditions for IBRs is when the voltage at the POM is zero. Ride-through during such conditions is not mandatory, but desirable in Tables 11 and 12 of the IEEE 2800 Standard [12]. However, the proposed method operates successfully for zero-voltage conditions as well because the derivations in Section V were independent of the voltage level. The

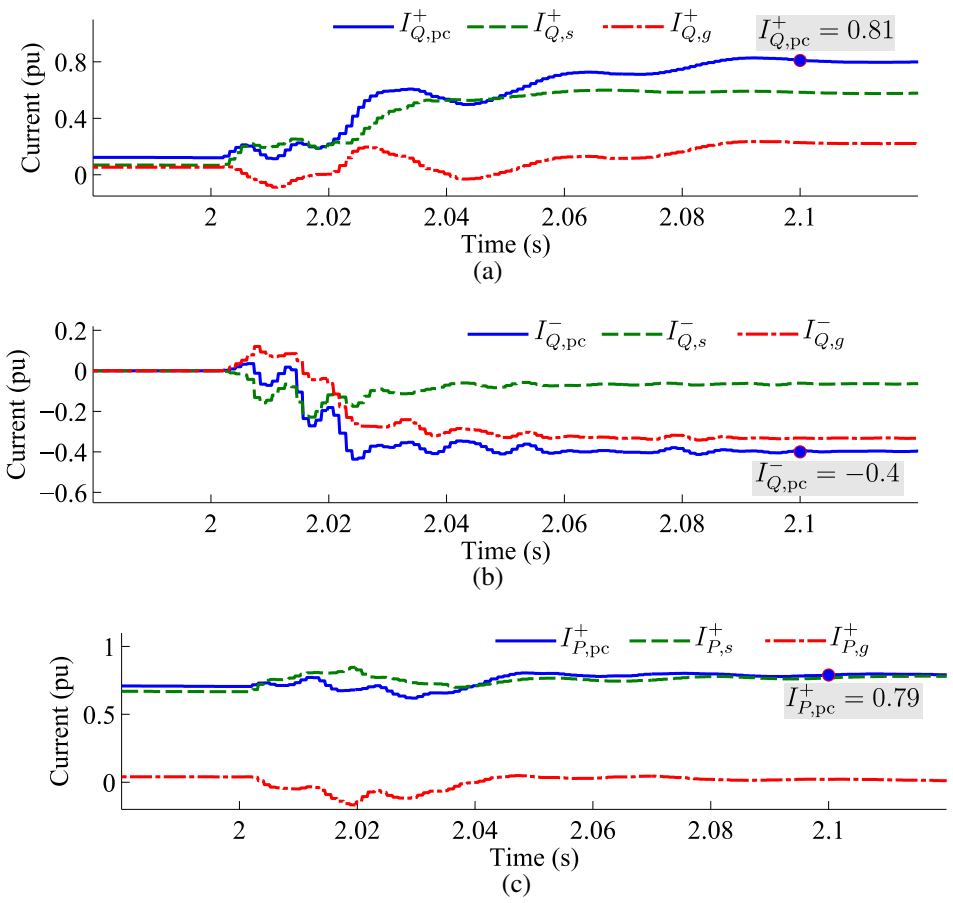

Figure 3.16: Currents at the POC for the fault of Fig. 3.4 when the DFIG uses the proposed method and f_c=400 Hz, (a) Positive-sequence reactive currents, (b) Negative-sequence reactive currents, (c) Positive-sequence active currents.

LVRT requirement of the IEEE 2800 Standard is for the grid faults. Thus the closest location for a zero-voltage fault for a DFIG is at the POM. The following investigates the performance of the proposed method during a bolted AG fault on line L215 next to bus B15 in Fig. 3.1, resulting in a zero voltage for phase A at the POM. Before the fault, the DFIGs operate at $s = -20\%$; the K-factor is 2; and f_c is 300 Hz. As a result of this fault, the positive-sequence voltage drops by 0.32 pu, and the negative-sequence voltage rises by 0.26 pu at the POC. The induced rotor voltage in (3.10) is 0.67 pu, which is higher than the RSC's maximum voltage, and so the RSC saturates. Fig.

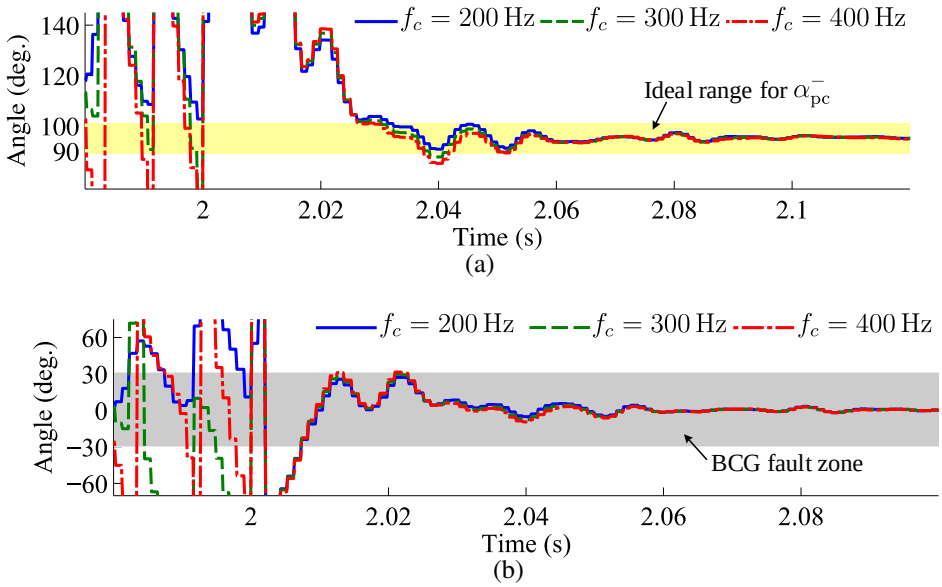

Figure 3.17: α_{pc}^{-} and δ^0 for the fault of Fig. 3.4 when the DFIG uses the proposed method, (a) α_{pc}^{-} at the POC, (b) δ^0 measured by R152 at the POM.

3.18 shows the current measured at the POC. It can be seen that the reactive current requirements for the above K-factor and voltage are met when the DFIG uses the proposed method during this zero-voltage condition, i.e., the DFIG complies with this preferred performance requirement of the 2800 standard. To demonstrate that the correct operation of the proposed method under zero-voltage condition is independent of f_c, Fig. 3.19 shows α_{pc}^{-} and δ^0 for different values of f_c. The proposed method pushes α_{pc}^{-} inside the [90°, 100°] range within 20 ms after the fault inception in Fig. 3.19. As a result, δ^0 remains inside the correct zone for the AG fault, and so the phase selection element of R152 operates reliably.

3.6.2 DCC-Based DFIG

Consider the BCG fault of Section 3.3.1 for which the ETPs could be fully suppressed. That case is repeated here for a DCC-based DFIG with the proposed control for the GSC. The fault decreases

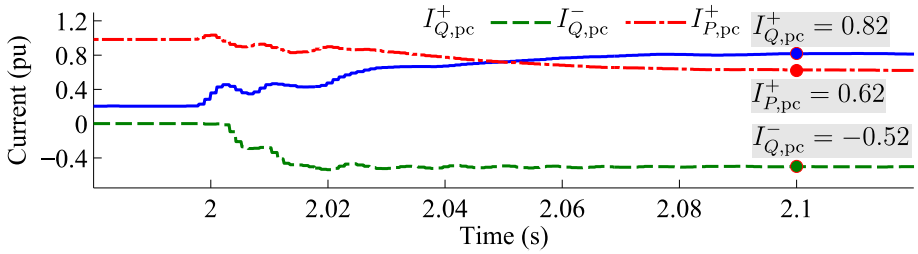

Figure 3.18: POC current when the DFIG uses the proposed method for a bolted AG fault at the POM in Fig. 3.1 with $s = -20\%$.

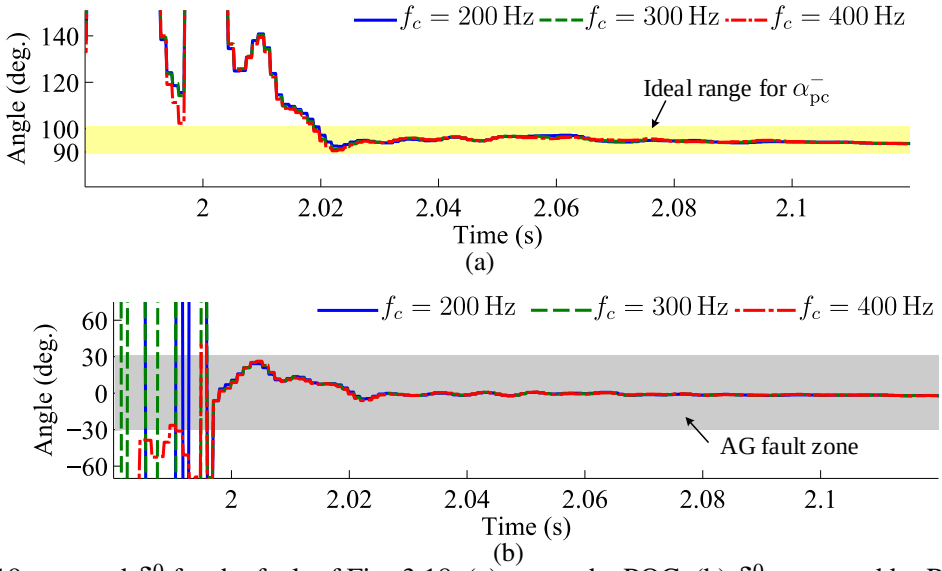

Figure 3.19: α^-_{pc} and δ^0 for the fault of Fig. 3.18, (a) α^-_{pc} at the POC, (b) δ^0 measured by R152 at the POM.

the positive-sequence voltage by 0.2 pu and increases the negative-sequence voltage by 0.12 pu at the POC. For $K = 2$ in Fig. 1.2, the positive- and negative-sequence reactive currents required at the POC are 0.4 pu (capacitive) and 0.24 pu (inductive), respectively. Fig. 3.20 shows that the DFIG satisfies these requirements. The positive-sequence reactive current generation by the RSC and the GSC are 0.3 pu and 0.1 pu, respectively, resulting in the 0.4 pu $I^+_{Q,\mathrm{pc}}$ in Fig. 3.20. Fig. 3.21 displays different components of the negative-sequence reactive current. The stator generates a 0.01 pu capacitive $I^-_{Q,s}$, but the proposed control scheme for the GSC fixes the problem by adding an

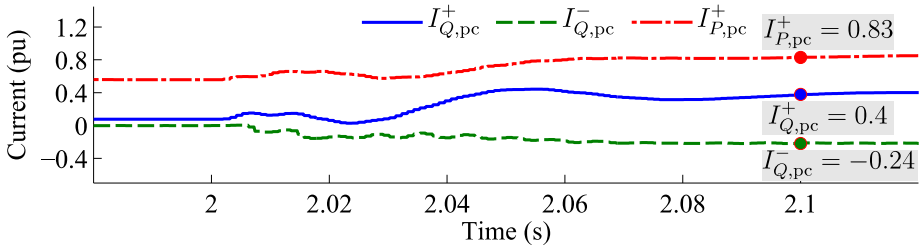

Figure 3.20: POC current when the DFIG uses the proposed method for the fault of Fig. 3.6.

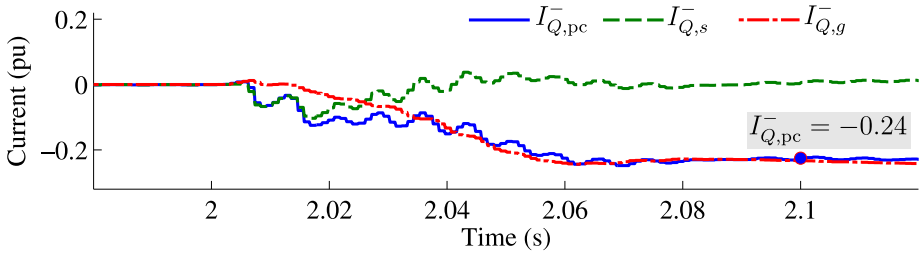

Figure 3.21: Different components of the negative-sequence reactive current when the DFIG uses the proposed method for the fault of Fig. 3.6.

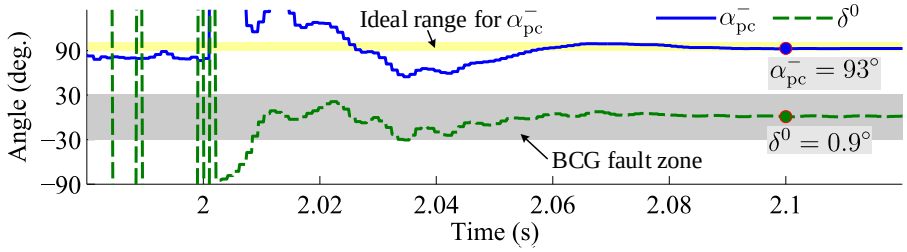

Figure 3.22: α^-_{pc} at the POC and δ^0 measured by R152 when the DFIG uses the proposed method for the fault of Fig. 3.6.

inductive $I^-_{Q,g}$ = 0.25 pu to $I^-_{Q,s}$ and delivering $I^-_{Q,\mathrm{pc}}$ = 0.24 pu (inductive).

Fig. 3.22 shows α^-_{pc} at the POC and δ^0 at the POM for this case. Unlike Fig. 3.7, α^-_{pc} in Fig. 3.22 enters the [90°, 100°] range within three cycles. Thus, a DFIG with the proposed control scheme can meet the 2800 Standard for IBRs without the need for an exemption for the angle of the negative-sequence current. Further, this ideal α^-_{pc} leads to a δ^0 that correctly determines the fault type in Fig. 3.22, preventing the problem observed for R152 in Fig. 3.8.

A similar analysis is applicable to the BCG fault of Section 3.3.2 for which the ETPs were

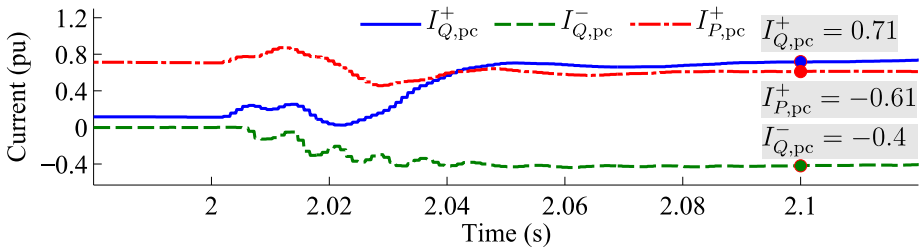

Figure 3.23: POC current when the DFIG uses the proposed method for the fault of Fig. 3.9.

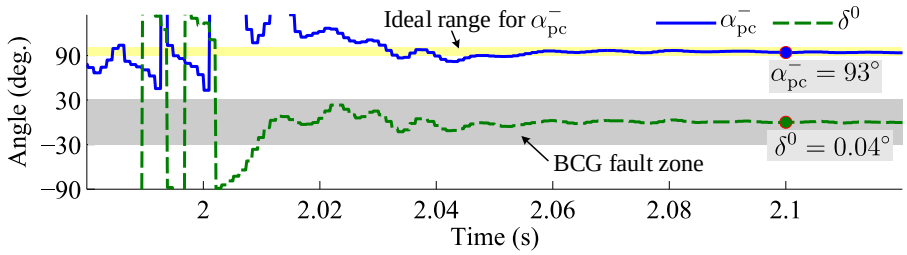

Figure 3.24: α^-_{pc} at the POC and δ^0 measured by R152 when the DFIG uses the proposed method for the fault of Fig. 3.9.

partially suppressed. The fault causes a 0.36-pu drop in V^+_{pc} and a 0.2-pu rise in V^-_{pc}. For $K=2$ in Fig. 1.2, the $I^+_{Q,\mathrm{pc}}$ and $I^-_{Q,\mathrm{pc}}$ required at the POC are 0.72 pu (capacitive) and 0.4 pu (inductive), respectively. Fig. 3.23 shows that this requirement is met at the POC and 0.61 pu of positive-sequence active current is also generated. Fig. 3.24 shows α^-_{pc} and δ^0. In contrast to Fig. 3.10, α^-_{pc} in Fig. 3.24 enters the [90°, 100°] range quickly after the onset of the fault. This α^-_{pc} pushes δ^0 in Fig. 3.24 inside the shaded area, correctly indicating a BCG fault and avoiding the problem observed for R152 in Fig. 3.11.

The performance of the proposed method was also examined during various high-impedance fault conditions. The following reviews an SLG fault when the DFIG's RSC uses the DCC scheme. Consider an AG fault with $R_f = 50\ \Omega$ on line L215 next to bus B15 in front of R152 in Fig. 3.1. Prior to the fault, the DFIG operates in the sub-synchronous mode with $s = 30\%$ and K=2. Fig. 3.25 depicts the current measured at the POC during this fault. Given that K=2, $|\Delta V^+_{\mathrm{pc}}|$= 0.12 pu,

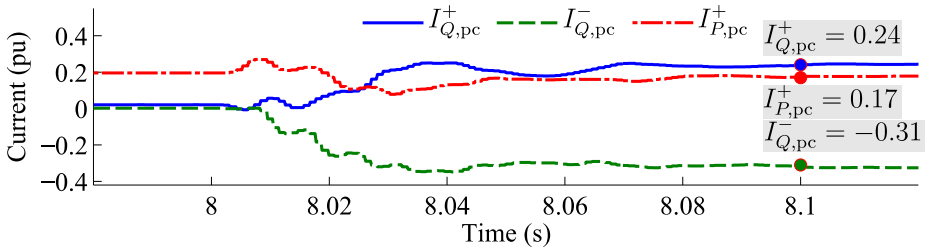

Figure 3.25: POC current during an AG fault with $R_f = 50\ \Omega$ when the DFIG uses the proposed method.

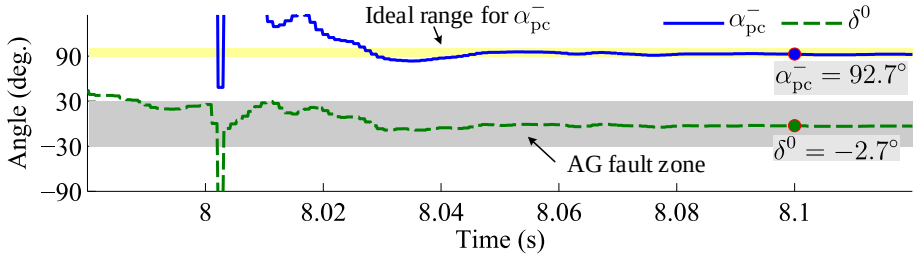

Figure 3.26: α^-_{pc} at the POC and δ^0 measured by R152 for the fault of Fig. 3.25.

and $|\Delta V^-_{\mathrm{pc}}|= 0.155$ pu, $I^+_{Q,\mathrm{pc}}$ and $I^-_{Q,\mathrm{pc}}$ correctly follow the K-factor diagram and are 0.24 pu and -0.31 pu, respectively, in this figure. Moreover, Fig. 3.26 shows α^-_{pc} and δ^0 of R152. In this figure, α^-_{pc} enters the [90°, 100°] range roughly 25 ms after the fault inception, resulting in δ^0 settling inside the [$-30°$, 30°] range for this AG fault. Thus, R152 identifies the fault type correctly. This case study shows that when the DFIG uses the proposed method, compliance with the 2800 standard and correct phase selection by the relays are independent of the fault type and resistance.

The following investigates the operation of the relays inside the collector system of the wind farm when the DFIG is equipped with the proposed control system. Consider a phase-B-to-phase-C (BC) fault with R_f =5 Ω at 85% of line L215 from B15 in Fig. 3.1. Before the fault, the DFIG operates similar to the previous case and K=2. $|\Delta V^+_{\mathrm{pc}}|$ and $|\Delta V^-_{\mathrm{pc}}|$ are 0.375 pu and 0.32 pu, respectively, for this fault. The reactive currents successfully satsify the K-factor diagram and are $I^+_{Q,\mathrm{pc}}$ =0.75 pu and $I^-_{Q,\mathrm{pc}}$= -0.64 pu in Fig. 3.27. Moreover, Fig. 3.28 shows the angle between the

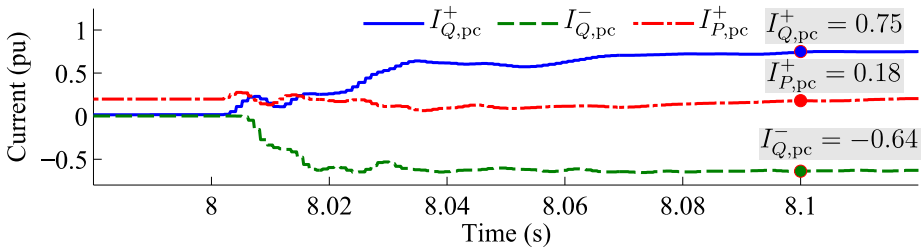

Figure 3.27: POC current when the DFIG uses the proposed method for a BC fault with $R_f = 5\ \Omega$ at 85% of line L215 with $s = 30\%$.

negative-sequence current and voltage at three locations, namely the LV side of the turbine-level transformer, i.e., the POC (α^-_{pc}), the collector side of the turbine-level transformer (α^-_{c}), and the POM (α^-_{pm}). It is illustrated that all of these three angles settle within the [90°, 100°] band, thereby complying with the standard. This shows that the transformer impedances and the transformers' winding configurations do not impact the performance of the proposed method. This stems from the fact that a transformer is modeled by a series impedance in the negative-sequence circuit irrespective of the winding configuration, and it shifts the angle of the negative-sequence voltage and current by the same amount. Therefore, the angle difference between the negative-sequence voltage and current remains almost equal to 90° throughout the collector system and at the POM, where R152 is located.

Since the type of this fault is LL and no zero-sequence current is present, the relay uses $\delta^+ = \measuredangle I^- - \measuredangle I^+$ in Fig. 1.3 to select the faulty phase(s). Fig. 3.29 shows δ^+ measured by R152 at the POM. Since the proposed method successfully regulates α^-_{pc} and α^-_{pm} at almost 90°, δ^+ in Fig. 3.29 correctly lies within the correct zone for BC faults, i.e., [165°, 195°]. As a result, R152 can determine the fault type accurately.

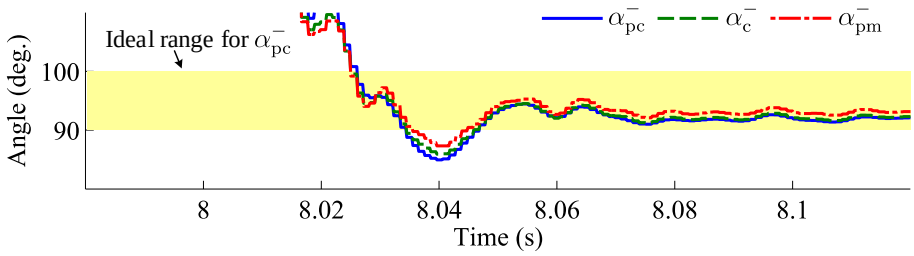

Figure 3.28: α_{pc}^{-}, α_{c}^{-}, and α_{pm}^{-} for the fault of Fig. 3.27.

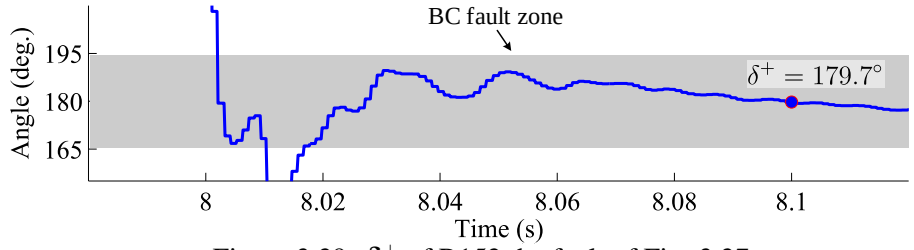

Figure 3.29: δ^{+} of R152 the fault of Fig. 3.27.

3.7 Conclusion

This Chapter showed why/how the angle of a DFIG's negative-sequence current during LVRT deviates from the ideal [90°, 100°] range. For the CVC scheme, the deviation is primarily determined by the bandwidth of the RSC's current control loop. For this scheme, the negative-sequence current angle stays within the wider [90°, 150°] range allowed for DFIGs by the 2800 Standard. However, it is demonstrated in this chapter that the relays can be adversely affected by this deviation. If the DFIG uses DCC for the RSC to suppress the ETPs, the angle falls even outside the [90°, 150°] range. This would violate the 2800 Standard, even with the exemption, and negatively impact the protection system. This chapter also developed a control system for the GSC to move the phase difference between the negative-sequence voltage and current of a DFIG to the ideal [90°, 100°] range. This would obviate the need to exempt the DFIGs from this requirement in the future revisions of the 2800 Standard. This chapter proved the feasibility of this solution for realistic DFIGs.

Chapter 4

Distance Protection of Lines Connected to DFIG-Based Wind Farms During Interrupted Control of DFIGs

As mentioned in Chapter 1, existing distance relays are designed assuming that SGs are the only generating units, where only the system-frequency components and their harmonics are present in the fault current and voltage [70]. However, as it is shown in [20], the fault signals of DFIGs during interrupted control of DFIGs, i.e., during crowbar connection, contain high-magnitude off-nominal frequency components. It has been demonstrated in the literature that the presence of the off-nominal frequency in the DFIG fault signals during balanced faults can negatively affect distance relays' operation that calculates the apparent impedance to the fault [20]. However, neither the operation of the distance relays elements, such as frequency tracking and phasor measurements

units (PMUs), nor the operation of the relays during unbalanced faults is investigated.

Aside from the presence of off-nominal frequency components in the DFIG fault signals, the crowbar or chopper circuits can make the equivalent sequence circuits of DFIGs different than those of SGs. This can potentially result in maloperation of commercial distance relays, such as the reactance method in [71], that are founded upon equivalent sequence circuits of SGs.

On this basis, after describing the test system, Section 4.2 investigates the fault current characteristics of DFIGs during unbalanced faults and interrupted control of DFIGs. Section 4.3 shows how commercial frequency measurement techniques operate when there is an off-nominal frequency component in their input signal. In Section 4.4, the operation of distance relays with the apparent impedance calculation approach and the reactance method during unbalanced faults is investigated. It is unveiled that how the fault current signals and equivalent sequence circuits of DFIGs affect the operation the distance relays. A solution is developed to address maloperation of the distance relays that protect the DFIGs tie-line

4.1 Description of the Test System

4.1.1 Power System Configuration

The IEEE 9-bus system, shown in Fig. 4.1, is simulated using PSCAD/EMTDC for this study [72]. The synchronous generator (SG) at bus 4 of the original system is replaced by 51-MW wind plant that includes 34 1.5-MW DFIGs. The plant's main step-up transformer is YGd, 60 MVA, 34.5 kV/230 kV with a leakage reactance of 0.1 pu. The plant is connected to bus 4 through the 40-km

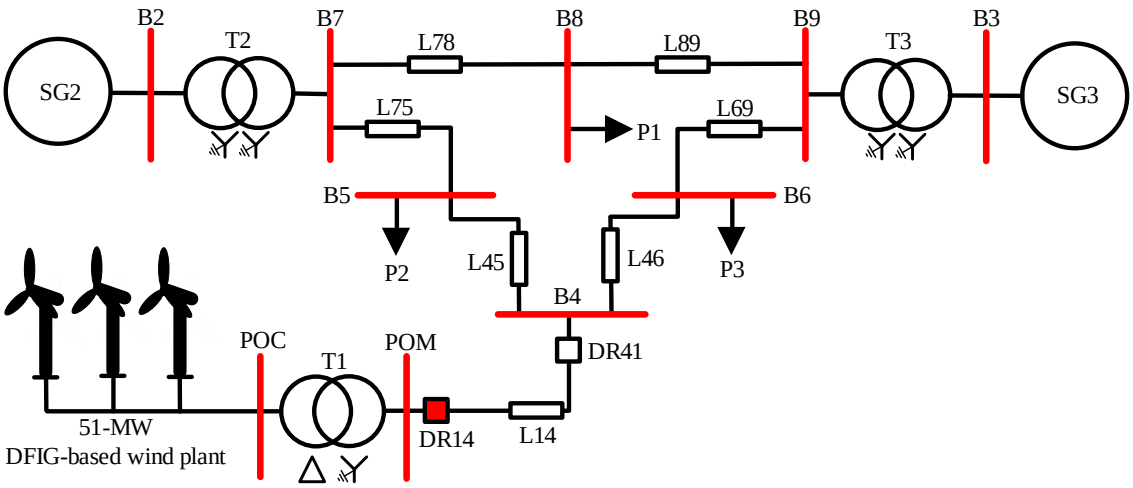

Figure 4.1: Single-line diagram of the test system.

line L14, whose positive- and zero-sequence impedances are $Z^{+}_{L14} = 0.0358 + j0.5078$ Ω/km and $Z^{0}_{L14} = 0.0363 + j1.3230$ Ω/km, respectively. DR14 and DR41 are the distance relays protecting line L14. Zones 1 and 2 of DR14 cover 90% and 120% of L14, respectively. The parameters of the DFIGs are presented in Appendix A.

4.1.2 DFIG-based WT Control System

In this study, the DFIG's RSC is controlled using the CVC scheme discussed in Chapter 2. To ride through the faults, an active crowbar and a braking chopper is used to protect the RSC from rotor overcurrents and the dc-link capacitor from overvoltages. The chopper can be used alone or in coordination with a crowbar. When used together, the priority of protection is given to the chopper, and crowbar is activated for deep voltage sags as a last resort. In both cases, the RSC gating is stopped during the protection scheme operation. However, the GSC will continue its operation as discussed in Section 2.4.

4.2 Fault Current Characteristics of DFIGs During Unbalanced Faults

This section first instigates the characteristics of the DFIG fault signals during unbalanced faults and crowbar connection. Afterwards, it investigates the fault signals characteristics of DFIGs during the rectification mode of operation.

4.2.1 DFIG Operation During Crowbar Connection

The voltage induced in the rotor winding of a DFIG is very large during severe grid faults, and so crowbar can be activated for a period of up to a couple of cycles. Consequently, the RSC's controllers are deactivated while the GSC remains in operation. The space vector of the DFIG fault current at the generator terminal during crowbar activation period is given by

$$\vec{i}_s(t) = \vec{i}_{sf}(t) + \vec{i}_{sn}(t) \tag{4.1}$$

where $\vec{i}_{sf}(t)$ and $\vec{i}_{sn}(t)$ are the space vectors of the stator steady state and decaying currents, given by (4.2) and (4.3), respectively [22].

$$\vec{i}_{sf}(t) = \vec{I}_s^{+} e^{j\omega t} + \vec{I}_s^{-} e^{-j\omega t} \tag{4.2}$$

$$\vec{i}_{sn}(t) = \vec{I}_{dc} e^{\frac{-t}{T_s}} + \vec{I}_{sr} e^{\frac{-t}{T_r}} e^{j\omega_m t} \tag{4.3}$$

In (4.2), $\vec{I}_s^{+}e^{j\omega t}$ and $\vec{I}_s^{-}e^{-j\omega t}$ are the stator positive-sequence and negative-sequence currents, respectively. These currents arise due to the positive-sequence and negative-sequence voltages at the DFIG terminals, and have a frequency equal to the fundamental frequency, i.e., ω. In (4.3), $\vec{I}_{dc}$ is the dc component of the stator current, which stems from the stator initial dc flux, $\vec{\psi}_{s,dc0}$, and decays with the stator time constant, T_s [16]. The stator dc flux appears to guarantee the continuity of the stator flux during the fault. As mentioned earlier in Chapter 2, during unbalanced faults, the magnitude of the stator dc flux, and hence, $\vec{I}_{dc}$, depends on the phase shift between the stator positive-sequence and negative-sequence fluxes at the fault instant. If the two fluxes are aligned, $\vec{\psi}_{s,dc0}$, and so $\vec{I}_{dc}$ will be zero. The magnitude of $\vec{\psi}_{s,dc0}$ increases commensurate with the phase shift between positive-sequence and negative-sequence fluxes. The maximum dc flux occurs when the two sequence fluxes are 180° out of phase [16]. $\vec{I}_{sr}$ in (4.3) is the stator decaying ac current, which is caused by the the rotor initial dc flux, $\vec{\psi}_{r,dc0}$ [23]. Similar to the stator dc flux, $\vec{\psi}_{r,dc0}$ appears to guarantee the continuity of the rotor flux during the fault. $\vec{\psi}_{r,dc0}$, and thus, $\vec{I}_{acr}$, decays with the rotor time constant expressed by

$$T_r = \frac{L_r - (L_m^2/L_s)}{R_r + R_c} \tag{4.4}$$

in which R_r and R_c are the rotor and crowbar resistances, respectively. From the stator winding perspective, the rotor dc flux is seen as a rotating flux that rotates at ω_m frequency. Therefore, the corresponding current, i.e., $\vec{I}_{acr}$, rotates at ω_m and decays with T_r.

Since the DFIG slip varies in the range of ±30%, ω_m adds a frequency component in the range of 42∼78 Hz to the fault current of a DFIG in a 60 Hz system. In addition, as the stator voltage depends on the stator flux and current, the non-fundamental frequency components in (4.2) and

(4.3) appear in the stator fault voltage as well, but with different magnitudes. The effect of the ω_m component in the fault signals extremely depends on the rotor time constant. Therefore, it can be concluded that the DFIG fault current during crowbar connection is composed of a fundamental frequency component, a decaying dc component, and a decaying component with ω_m frequency. The fundamental frequency component in the DFIG fault current is normally larger than the two decaying components.

The above discussion described the stator fault current of the DFIG while the current measured by a relay is the combination of the stator and the GSC current. The current from the GSC is balanced at the fundamental frequency. The control system of GSC includes feed-forward compensation of the grid voltage. As a result, any imperfection in the DFIG's terminal voltage—including the above-mentioned off-nominal frequency components—are eliminated from the current, and the GSC's current is almost entirely a 60-Hz signal.

To investigate the frequency content of a DFIG's fault current and voltage during unbalanced faults, a permanent phase-B-to-phase-C (BC) fault with fault resistance $R_f = 5\ \Omega$ is applied next to bus B4 on line L45 in Fig. 4.1. The rotor speed is 1.2 pu immediately before the fault inception. The fault occurs at $t = 1.996$ s, resulting in the maximum dc component in the stator fault current. The positive-sequence voltage at the POM drops by 65%, causing overcurrents in the rotor winding and activating crowbar. Crowbar resistance is set at the maximum allowable value of $20R_r$, which is a common value [24, 55]. To examine crowbar effect on the voltage and current frequency components, crowbar is kept activated during the whole duration of the fault.

Fig. 4.2 displays the voltage and current measured at the WF's POM. The fast Fourier transform

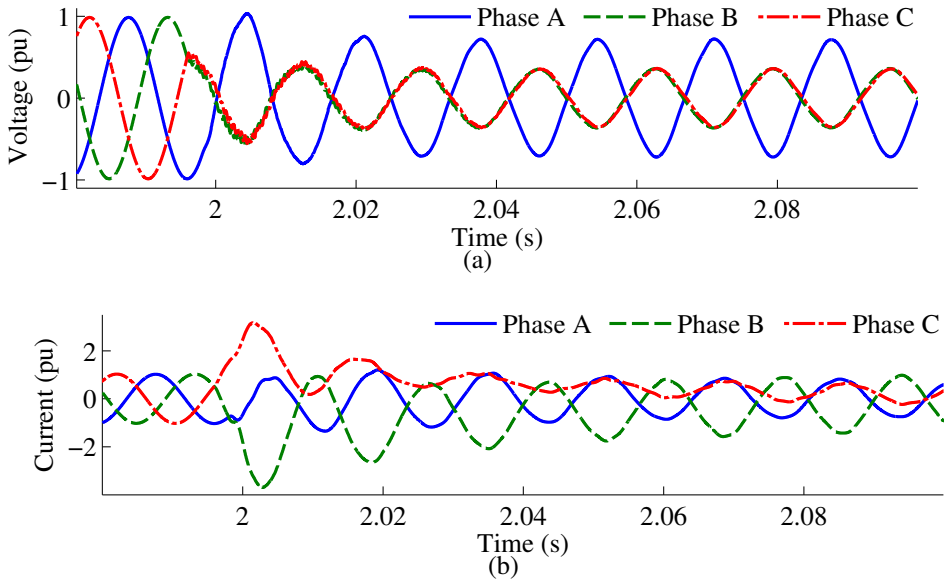

Figure 4.2: Measurements of DR14 for the BC fault on line L45: (a) voltage, (b) current.

(FFT) is applied to the first 83.3 ms of these fault signals—i.e., five fundamental cycles—to derive the frequency spectra shown in Fig. 4.3. For the current, the dc, 60-Hz grid frequency, and 72-Hz rotor-speed frequency components are visibly present in all three phases. Conversely, the voltage frequency is mainly dictated by the grid. Thus, the dc and rotor speed frequency components are relatively minute and not visually obvious. The non-zero values of the other components in the current and voltage spectra are due to the picket-fence effect of the FFT.

4.2.2 DFIG Operation During Rectification Mode

This subsection investigates the fault current of the DFIG during the rectification mode, i.e., when the breaking chopper is on while the RSC switching is turned off.

As mentioned in Chapter 2, the braking chopper may be activated when the voltage induced in the rotor winding of a DFIG exceeds the RSC maximum voltage limit, or the rotor current exceeds

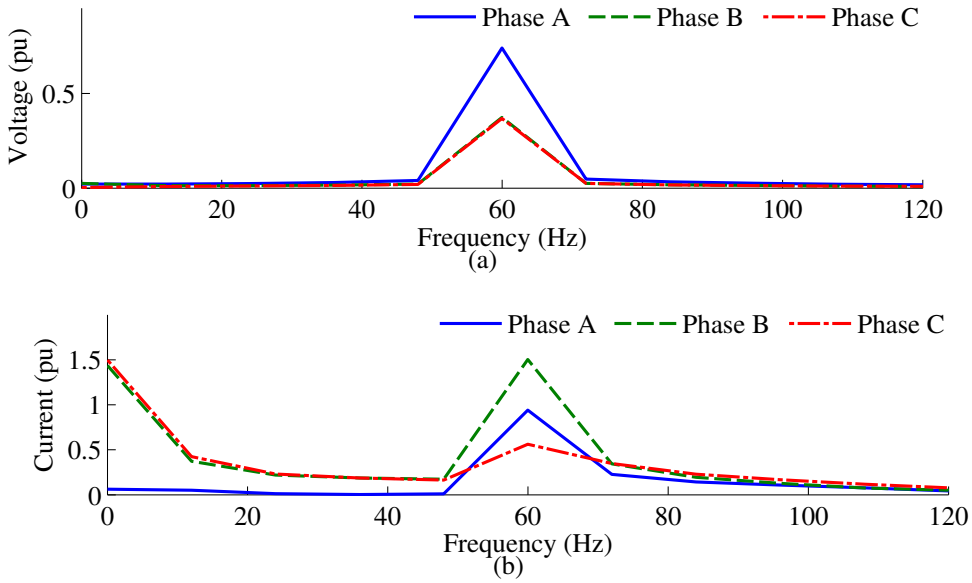

Figure 4.3: Frequency spectrum of the fault voltage and current in Fig. 4.2: (a) Voltage, (b) Current.

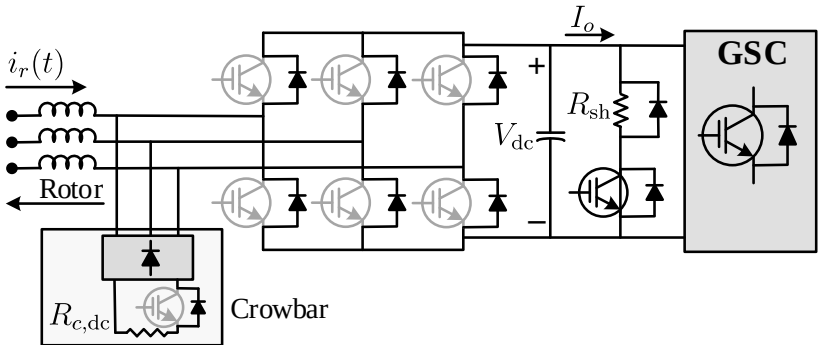

Figure 4.4: Rectification mode of operation (IGBTs are inactive and the braking chopper may or may not operate).

a predetermined value. In such a condition, the RSC gating will stop, and the rotor overcurrent is forced to commute through the RSC free-wheeling diodes [19]. This mode of operation, shown in Fig. 4.4, is known as rectification mode. In this figure, $R_{c,\text{dc}}$ is the dc crowbar resistance, V_{dc} is the dc-link voltage, R_{ch} is the braking chopper resistance, and I_o is rectified current by the RSC.

During the rectification mode, the GSC and the braking chopper attempt to regulate the dc-link voltage at 1 pu by either transferring the extra power to the grid or dissipating it by the braking

chopper resistance. Thus, they can be modeled as an equivalent resistive load. Since the dc-link voltage is kept constant, the operation of the RSC during the rectification mode is analogous to that of a three phase full bridge diode rectifier with a capacitor-filtered load supplied by a voltage source described in [73, 74]. In this analogy, the magnitude of the induced voltage at the rotor winding, i.e., the magnitude of $\vec{e}^{\,r}_{r,\mathrm{ind}}$ in (2.11), has a similar effect of the voltage source while the GSC and the braking chopper have the same effect of the capacitor-filtered load. With this analogy and neglecting the rotor resistance, the rectifier in Fig. 4.4 can be modeled by a resistance in each phase as in (4.5) [73, 74].

$$R_{\mathrm{rec}} = \frac{|\omega_{\mathrm{ind}}| L_r V_{\mathrm{dc}}}{\sqrt{(|\vec{e}^{\,r}_{r,\mathrm{ind}}|^2 - V_{\mathrm{dc}}^2)}} \tag{4.5}$$

In (4.5), ω_{ind} is the frequency of the induced voltage at the rotor winding. According to (4.5), for a given L_r and V_{dc}, R_{rec} varies depending on the induced rotor voltage and its frequency during a grid fault. The approximation for the equivalent resistance in (4.5) is valid only if $\vec{e}^{\,r}_{r,\mathrm{ind}}$ is balanced and is grater than V_{dc}, and the rectifier operates in continuous conduction mode. This situation occurs when a DFIG is subject to a balanced 100% voltage dip at the stator side. In such condition, $\vec{e}^{\,r}_{r,\mathrm{ind}}$, which is given in (2.11), is a balanced component with the frequency of ω_m. From (2.11), and considering the slip of a DFIG in the range of $\pm 30\%$, $|\vec{e}^{\,r}_{r,\mathrm{ind}}|$ at the beginning of a bolted balanced fault can be $3\sim5$ times of the normal operation. Therefore, for a bolted balanced fault and the DFIG with the parameters given in Table A.1, the initial value of R_{rec} is about 18 times of the rotor resistance. However, R_{rec} increases by time as $|\vec{e}^{\,r}_{r,\mathrm{ind}}|$ decays by the rotor time constant.

The above analysis indicates that the DFIG fault current during rectification mode is chiefly similar to (4.1) except that the rotor time constant in (4.4) is modified by replacing R_c with R_{rec}

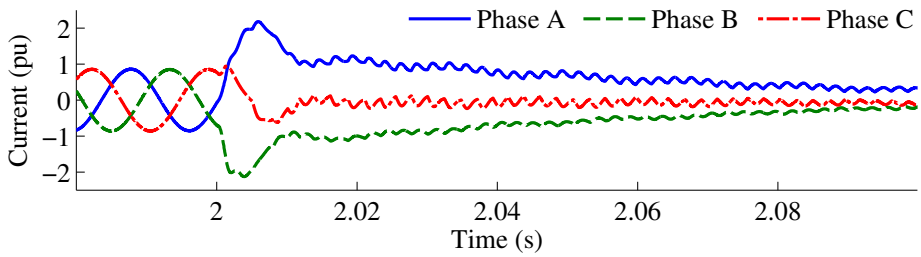

Figure 4.5: Generator fault current during the rectification mode for a bolted balanced fault at the POM.

Consequently, $\vec{I}_{acr}$ in (4.3), which rotates with ω_m, is large at the beginning of the fault. But, it decays faster than when the crowbar is active.

To verify the above analysis and investigate the frequency content of the DFIG's fault current during the rectification mode, a permanent bolted three-phase fault is applied at the POM in Fig. 4.1. The braking chopper resistance is set to be 0.7 Ω [19]. The anti-parallel diodes of the RSC are sufficiently uprated to manage the rotor overcurrents. The rotor speed is 1.2 pu immediately before the fault inception, and the fault occurs at $t = 2$ s. The rectification mode is kept on during the whole duration of the fault. Fig. 4.5 displays the fault current at the generator's terminals. The GSC current is not shown here as it only adds a grid-frequency component to the DFIG fault current. It is seen in Fig. 4.5 that the generator fault current contains the rotor-speed frequency component at the beginning of the fault. However, since R_{rec} increases by time, the rotor-speed frequency component decays very fast. That is why the fault current nearly resembles a decaying dc current after about 20 ms of the fault.

Equation (4.5) was obtained assuming that the rotor input currents are approximately sinusoidal, and the induced rotor voltage is larger than the dc-link voltage. As mentioned earlier, this situation occurs during bolted balanced faults at the DFIG terminals. However, R_{rec} cannot be obtained as straightforward as (4.5) during high impedance balanced faults or unbalanced faults. It is because,

according to (2.11), the induced rotor voltage during high impedance balanced faults contains the slip and $(1-s)\omega$ frequencies while during unbalanced faults it additionally contains $(2-s)\omega$ frequency. This situation violates the assumptions made for modelling of the rectification mode as a three phase full bridge diode rectifier with a capacitor-filtered load supplied by a voltage source. However, the simulation results for numerous unbalanced faults show that the rotor-speed frequency component is also present at the begining of the rectification mode for $1 \sim 2$ cycles. Therefore, the DFIG fault current during unbalanced fault and rectification mode of operation is also similar to (4.1) except that the rotor time constant in (4.4) is modified by replacing R_c with R_{rec}

The following unveils how the presence of the rotor-speed frequency component during crowbar connection or the rectification mode affects the operation of the frequency tracking of the commercial relays.

4.3 Frequency Measurement For DFIG Fault Signals

Distance relays use the frequency tracking algorithms to calculate the phasors of the voltage and current, and so, the impedance to the fault. This section shows how the DFIG fault signals discussed in the last section impact phasor measurement by a relay.

The phasor measurement unit of a relay always tracks the voltage and/or current frequency to continuously update the digital filters. As a result, phasor measurement is not affected by the changes in the fundamental frequency. A lot of frequency tracking methods are founded upon variations of the measured phasor's angle. In [8], for example, the rotation rate of the phasor calculated using a variable N-point discrete Fourier transform (DFT) with a sampling interval of Δt

yields the frequency. This is, by definition, the instantaneous frequency (IF) of the input signal [75]. Therefore, the IF of a signal with two distinct frequencies can offer insight into how DFIG fault signals (with an ω and an ω_m component) impact a relay's frequency tracking and, subsequently, phasor measurement.

Consider the sinusoidal signal in (4.6) with two frequency components at f_1 and f_2:

$$x(t) = x_1(t)\cos(\underbrace{2\pi f_1}_{\omega_1} t) + x_2(t)\cos(\underbrace{2\pi f_2}_{\omega_2} t) \tag{4.6}$$

where $x_1(t)$ and $x_2(t)$ are the time-variant magnitudes of the two frequency components. For $x_1(t) > x_2(t)$ and $f_2 > f_1$, the IF of $x(t)$ is given by (4.7) [76].

$$f(t) = f_1 + (f_2 - f_1)\frac{x_2^2(t) + x_1^2(t)x_2^2(t)\cos(2\pi(f_2 - f_1)t)}{M^2(t)} \tag{4.7}$$

$M(t)$ is the magnitude of $x(t)$ obtained by

$$M(t) = \sqrt{x_1^2(t) + x_2^2(t) + x_1(t)x_2(t)\cos(2\pi(f_2 - f_1)t)} \tag{4.8}$$

Equation (4.7) shows that for a signal in the form of (4.6), the IF oscillates asymmetrically around the more dominant frequency component. The rate of oscillations is $|f_1 - f_2|$ Hz.

To verify that (4.7) expresses the frequency calculated by a relay that measures the fault signals of a DFIG, consider (4.6) for $x_1(t) = 1$, $f_1 = 60$ Hz, and $f_2 = 72$ Hz. $x_2(t)$ is equal to 0 and 0.2 before and after $t = 1$ s, respectively. This signal and its IF along with the frequency calculated

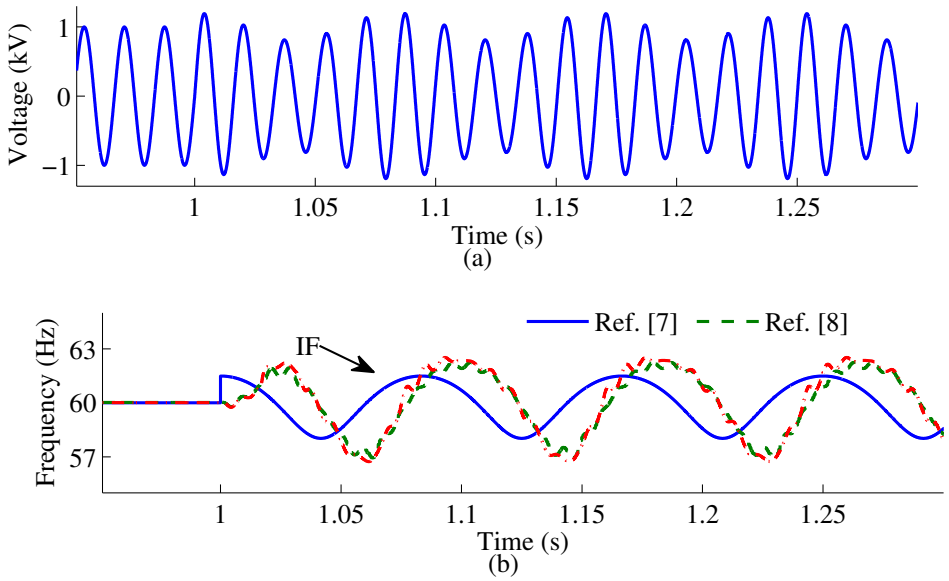

Figure 4.6: Performance of frequency measurement techniques: (a) synthetic voltage with 60 and 72 Hz components, (b) frequencies measured by [8] and [9].

using the method of [8] are displayed in Fig. 4.6. It is shown that, similar to the IF, the frequency given by [8] asymmetrically oscillates around 60 Hz at a rate of 12 Hz once the 72-Hz component is added to the signal. The delay of the measured frequency is because it takes at least one cycle after $t = 1$ s for the data window of DFT to get filled with the 72-Hz component.

Some relays use non-phasor-based frequency tracking methods, such as the one in [9]. However, since these methods are founded upon the assumption that the instantaneous signal is composed of the fundamental frequency component and its harmonics, they also fail to measure the dominant frequency component of a DFIG fault signal accurately. As shown in Fig. 4.6(b), there is no material difference between the frequencies measured using the methods in [8] and [9].

As discussed in the last section, the rotor frequency component of an actual DFIG fault signal decays over time with the rotor time constant, T_r. As a result, the variation of the frequency measured by the relay from the fundamental frequency declines at the same rate. Consider, for

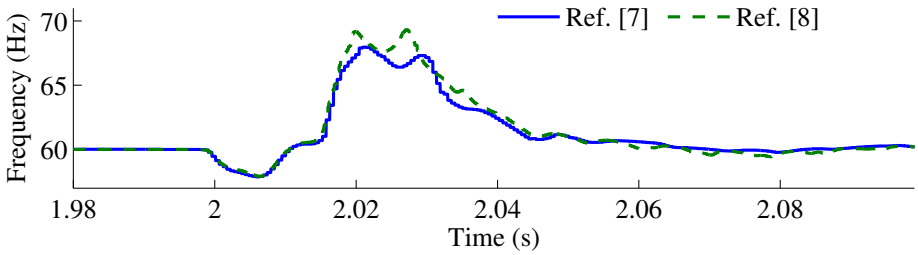

Figure 4.7: The frequency measured by methods in [8] and [9] for the BC fault on Line L45.

instance, the frequency measured for the fault currents of Fig. 4.2. The three-phase currents are combined using

$$i_f(t) = i_a(t) - \frac{i_b(t) + i_c(t)}{2} \tag{4.9}$$

which is a common practice in commercial relays [77]. i_f given by (4.9) is fed to the frequency tracking methods [8] and [9]. As depicted in Fig. 4.7, the measured frequency initially oscillates at 12 Hz, but the oscillations subside as soon as the rotor frequency component declines.

4.4 Operation of Distance Relays During RSC Control Interruption

This section shows how the characteristics of DFIG fault signals and their impact on frequency tracking methods, detailed in the last two sections, affect the operation of a distance relay. First, the performance of a distance relay that operates based on the calculation of apparent impedance is investigated. This would offer basic insight into the problems caused by DFIGs. Afterwards, further complications caused by the techniques used by commercial relays are revealed by examining the operation of distance relays based on the reactance method in [71].

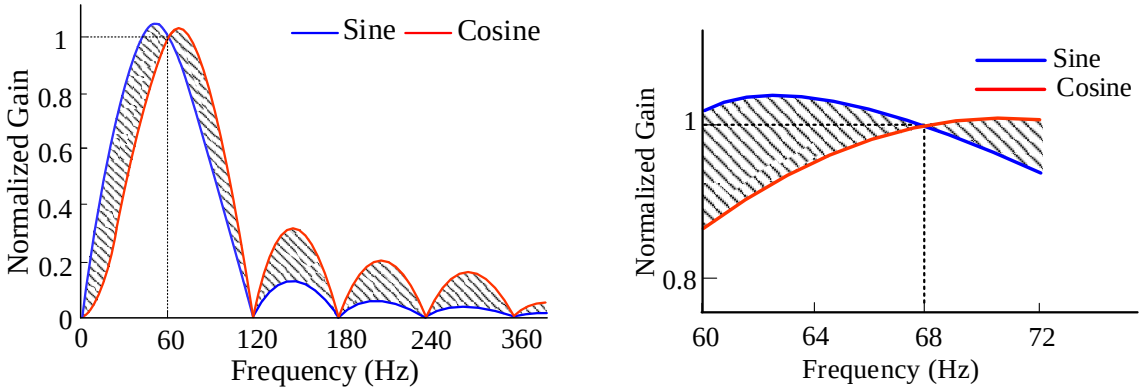

Figure 4.8: (a) frequency response of the sine and cosine filters around the fundamental frequency, (b) gains of DFT sine and cosine filters for the tracked frequency of Fig. 4.7.

4.4.1 Apparent Impedance Calculation

Calculation of apparent impedance for distance protection relies upon precise measurement of the fundamental-frequency phasor for all three phase voltages and currents. In the case of DFIGs during unbalanced faults, this would mean that the ω component of the fault currents in (4.2) and (4.3) must be perfectly extracted. Distance relays usually calculate phasors using DFT, whose sine and cosine filters are updated based on the result of frequency tracking. Assuming that the computed frequency is 60 Hz, the frequency response of the sine and cosine filters around the fundamental frequency are displayed in Fig. 4.8(a). The shaded area between the two frequency responses indicate the amount of oscillation in the calculated phasor for a signal at a given frequency. There is no oscillation at 60 Hz, but as the frequency deviates from 60 Hz, the gap between the two filter gains widens and the phasor becomes more oscillatory. These are exactly the frequency intervals where the ω_m component of DFIG fault signals may reside.

To illustrate the impact of DFIG fault signals on DFT measurements, Fig. 4.9 displays the

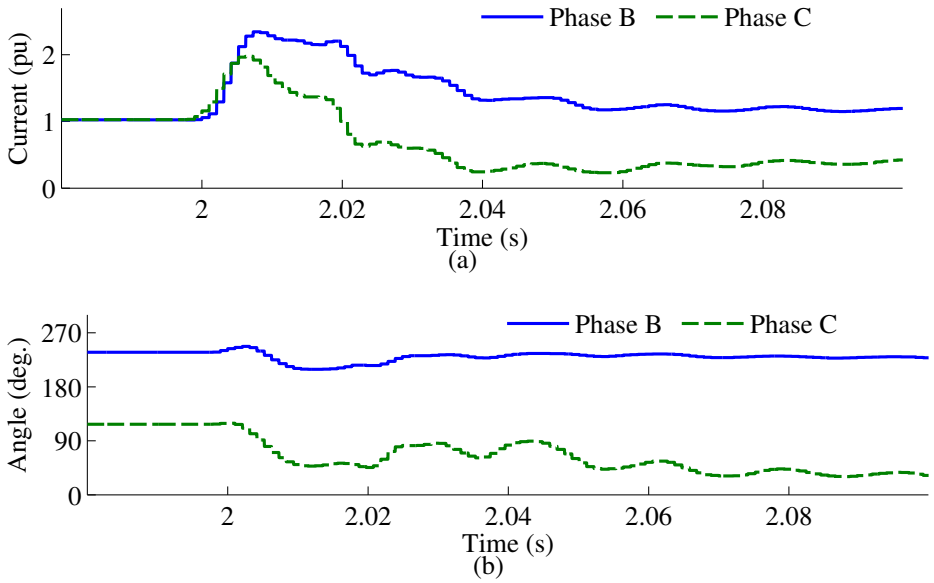

Figure 4.9: Phasors of phases B and C for the BC fault on line L45: (a) magnitude, (b) angle.

current phasors for phases B and C during the BC fault discussed in Section 4.2. It is evident that the phasor undergoes significant oscillations in the beginning of the fault. This is a direct result of the fault currents' 72-Hz rotor-frequency component, for which the DFT filters have different gains. This problem cannot be tackled through frequency tracking. The frequency measured for this fault in Fig. 4.7 reaches beyond 68 Hz shortly after the fault inception. The gains of DFT sine and cosine filters for this tracked frequency are shown in Fig. 4.8(b). Here the gains are equal neither for the synchronous, nor for the rotor-frequency component. That is why the phasors in Fig. 4.9 keep fluctuating until the rotor-frequency component dies out. The following investigates the effect of the rotor-speed frequency component of the DFIG fault signal and the phasor fluctuations on distance relays.

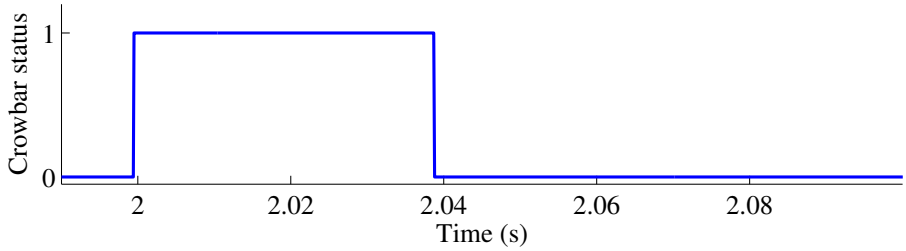

Figure 4.10: Crowbar status for the BC fault on line L45.

1) Line-to-Line Faults

To investigate the effect of the rotor-speed frequency component of the DFIG fault signals on the distance relay, the BC fault of Section 4.2 is repeated, when the LVRT mode is turned on. Fig. 4.10 shows the crowbar connection time for the BC fault, where the crowbar is activated for 38 ms.

The BC element of a distance relay, for example, measures the apparent impedance to the fault location by dividing the fundamental frequency phasors of phases B and C voltages over their respective currents, i.e., $Z_{BC} = (V_B - V_C)/(I_B - I_C)$. The current phasors of Fig. 4.9 is used to measure the resistance and reactance of the BC element of DR14, shown in Fig. 4.11. As can be seen in this figure, due to the fluctuations of the current phasors, the calculated resistance and reactance experience significant oscillations. These oscillations are directly translated into the impedance rotation in the impedance plane shown in Fig. 4.12. DR14 should trip as a backup protection for a fault on Line L45 if the fault persists for more than a delay time, usually of the order of 300 ms. However, while rotating, the impedance trajectory enters zone 1 of the relay 10 ms after the fault, leading to false trip of line L14 before the required 300 ms time delay is passed. Consequently, secure operation of DR14 as well as any subsequent LVRT scheme designed inside the WF is failed.

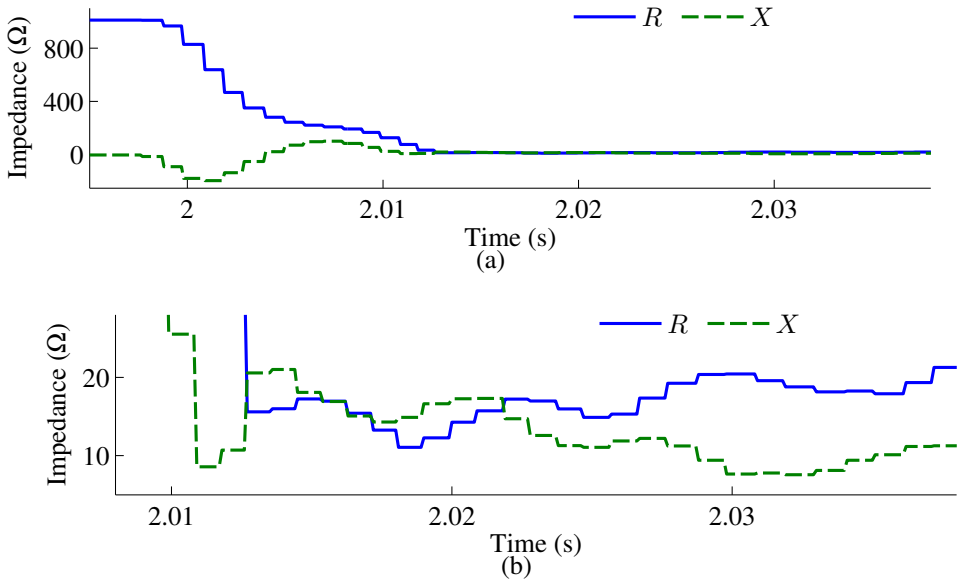

Figure 4.11: Apparent impedance calculated by the BC element of DR14 at the second zone of DR14: (a) Measured resistance and reactance, (b) Magnified view of the resistance and reactance.

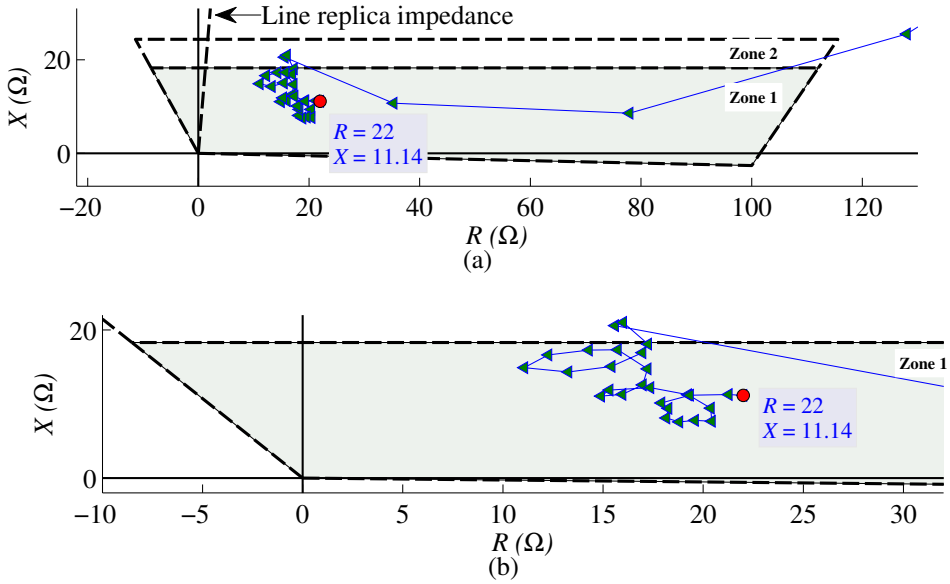

Figure 4.12: Apparent impedance calculated by the BC element of DR14 at the second zone of the relay: (a) Impedance trajectory, (b) Magnified view of the impedance trajectory.

Similar analysis can be presented for the performance of DR14 during the rectification mode. This mode of operation is activated when the rotor current exceeds 2 pu. This mode is ended when the rotor current falls below a predetermined value [19]. To evaluate DR14 performance, the same

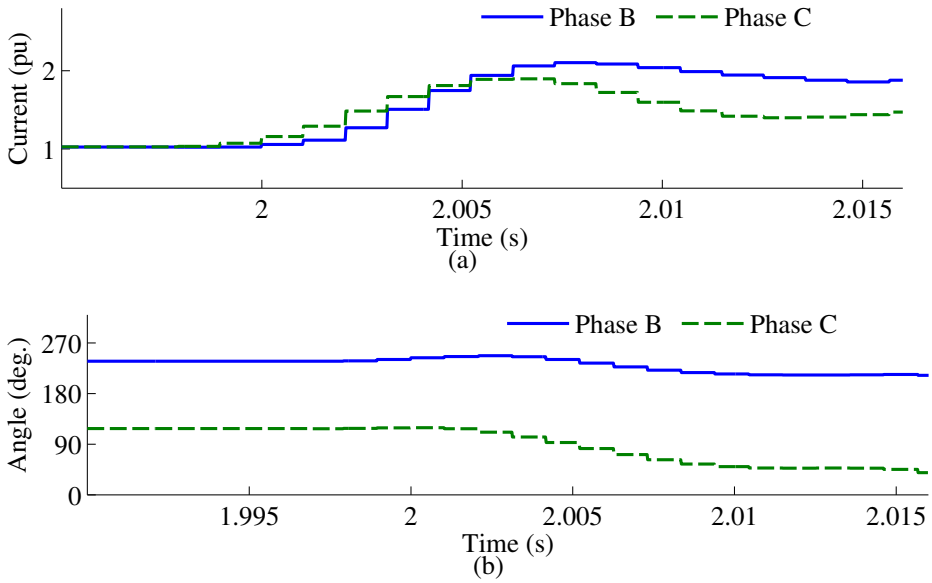

Figure 4.13: Phasors of phases B and C for the BC fault on line L45: (a) magnitude, (b) angle.

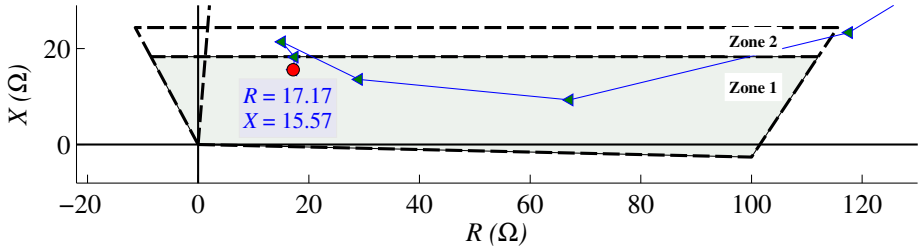

Figure 4.14: Apparent impedance calculated by the BC element of DR14 at the second zone of the relay during the rectification mode.

BC fault is repeated. The rectification mode is activated 3 ms after the fault inception and remains active for 17 ms. Fig. 4.13 displays the current phasors for phases B and C. Similar to crowbar connection time, the current phasors experience fluctuations. However, as the rectification mode is shorter than crowbar connection time, the fluctuations do not cause any rotation in the impedance plane shown in Fig. 4.14. The impedance trajectory enters to zone 1 of the relay 10 ms after the fault inception, leading to a false instantaneous trip of line L14.

The simulations are repeated for different types of faults with different fault resistances, different

rotor speeds, and other operating conditions affecting the fault currents of the DFIGs during both crowbar connection and the rectification mode. In most LL or LLG faults, the impedance trajectories in the impedance plane display an unreliable behavior.

2) Line-to-Ground Faults

The apparent impedance measured by the AG element of a distance relay is expressed as

$$Z_{AG} = \frac{V_A}{I_A + K^0 I^0} \tag{4.10}$$

where V_A and I_A are the phase A voltage and current, respectively. I^0 is the zero-sequence component of the fault current, and K^0 is the zero-sequence compensation factor, which is $1.72 \measuredangle -17.86^\circ$ for the system of Fig. 4.1. As mentioned earlier in Section 4.2, the voltage frequency is mainly dictated by the grid. Thus, the voltage is of the fundamental frequency type in the numerator of (4.10). The fundamental frequency component dominates the denominator of (4.10) as well during crowbar or rectification activation modes of a DFIG. As mentioned earlier, these modes are activated once the voltage dip is sever. This results in flow of a large zero-sequence from the neutral winding of the WF's main step-up transformer, which has a YGd winding configuration, to the fault. Thus, the zero-sequence current dominates relay measurements as well as the denominator of (4.10). Given that the zero-sequence current is not impacted by the DFIG's fault behaviour, the off-nominal frequency component of $I_A + K^0 I^0$ is much smaller than the fundamental frequency component, and so the apparent impedance as well as the tracked frequency remain stable and with minimal oscillations. As a result, the relay behaves similar to conventional systems with SGs.

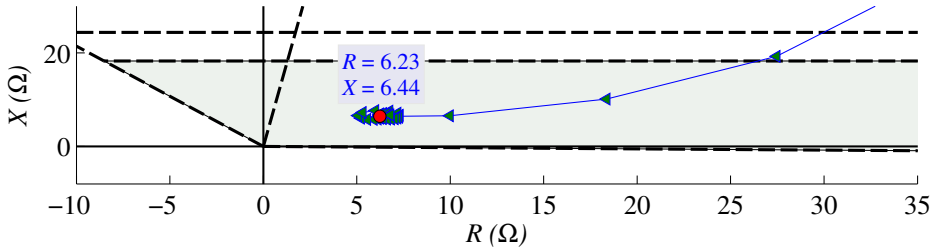

Figure 4.15: Apparent impedance calculated by the AG element of DR14.

To investigate the operation of DR14 during the crowbar connection, consider a phase-A-to-ground (AG) fault at 25% of line L14 with $R_f = 5\ \Omega$. The rotor speed is 1.2 pu immediately before the fault inception. The fault occurs at $t = 2$ s, resulting in the maximum dc component in the stator fault current. The crowbar is activated 5 ms after the fault inception and remains active for 16 ms. The impedance between the relay and the fault is $Z_{AG} = 0.358 + j5.078\ \Omega$. Fig. 4.15 shows the measured impedance for the AG fault. As can be seen in this figure, the reactance calculated with DR14 is only 1.34 Ω larger than the actual impedance to the fault. The impedance enters zone 1 in less than 15 ms. Similar to conventional systems with SGs, the impedance settles in its final position with minimal oscillation. Therefor, DR14 operates correctly for LG faults.

4.4.2 Reactance Method

The infeed current at the remote end of a line introduces an error to the apparent impedance measured by distance relays when there is a fault resistance. The reactance method used by commercial relays tackles this problem by giving the actual impedance to the fault location through estimating the phase angle of the fault current at the fault location. This subsection shows how the characteristics of the DFIG fault signals affect the operation of distance relays based on the reactance method

in [71].

1) Line-to-Line Faults

The reactance and resistance of the phase element measured by the reactance method during, for example, BC faults are given by (4.11) and (4.12), respectively [71].

$$X_{BC} = \frac{\mathrm{Im}[V_{BC}\bar{I}_{F_{est}}]}{\mathrm{Im}[Z^{+}_{L14}(I_B - I_C)\bar{I}_{F_{est}}]}|Z^{+}_{L14}|\sin(\measuredangle Z^{+}_{L14}) \tag{4.11}$$

$$R_{BC} = \frac{\mathrm{Im}[V_{BC}\overline{(Z^{+}_{L14}(I_B - I_C))}]}{\mathrm{Im}[2I_{F_{est}}\overline{(Z^{+}_{L14}(I_B - I_C))}]}|Z^{+}_{L14}|\cos(\measuredangle Z^{+}_{L14}) \tag{4.12}$$

In these equations, $\mathrm{Im}(.)$ and $\bar{(.)}$ denote the imaginary part and complex conjugate, respectively; $I_{F_{est}}$ is the estimated phasor of the fault current, which is estimated using the local negative-sequence current, jI^{-}_{L}. $I_{F_{est}}$ at the relay location is estimated based upon the fact that the the remote end negative-sequence current, denoted by I^{-}_{R}, is in phase with I^{-}_{L}.

The following shows how the equivalent negative-sequence circuits of DFIGs differ from those of SGs that can impact $\measuredangle I_{F_{est}}$, and consequently, result in wrong measurement of the impedance to the fault.

2) Reactance Method Operation During the First 1∼3 Cycles of Crowbar Activation

Given that a DFIG is essentially a SCIG with high rotor resistance during crowbar connection, the equivalent sequence circuit of the SCIG can be adopted to be used for the DFIG. As it is demonstrated in [21], the equivalent sequence circuit of a SCIG has two stages. The first stage,

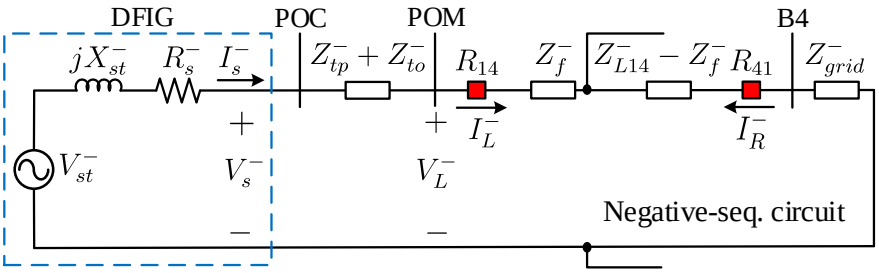

Figure 4.16: Transient negative-sequence circuit of the test system for a BC fault on line L14.

namely, the transient stage, starts at the instant of the fault inception and lasts for the first 1∼3 cycles, depending on the rotor time constant. The second stage, namely, the steady state stage, starts after 1∼3 cycles of the fault inception and lasts till the end of the fault. The following investigates the operation of the reactance method during the first 1∼3 cycles of the crowbar activation.

The transient equivalent negative-sequence circuit of the test system during the crowbar connection for a BC fault on line L14 can be shown as in Fig. 4.16. In this figure, $X_{st}^- = X_s - X_m^2/X_r$ is the stator transient reactance; X_s and X_r denote the stator and rotor leakage reactants, respectively; X_m is the magnetizing reactance; V_{st}^- is the transient voltage behind the stator transient reactance. The subscripts r, s, and p denote the rotor, stator, and POC quantities, respectively. Z_{tp} and Z_{to} are the generator and the main step-up transformer impedances, respectively; Z_f is the impedance to the fault location; Z_g^- is the impedances of the grid behind bus B4. All parameters of the DFIGs are referred to the stator. The GSC is not modeled in the equivalent negative-sequence circuit of Fig. 4.16 as it does not generate any negative-sequence current.

As shown in Fig. 4.16, contrary to SGs, the negative-sequence voltage of V_{st}^- appears behind the stator transient reactance due to the negative-sequence rotor flux and decays with the rotor transient time constant defined by (4.4). Thus, this circuit is valid for the first 1∼3 cycles of the fault depending on crowbar resistance, and hence, the rotor time constant, i.e., T_r. Although V_{st}^-

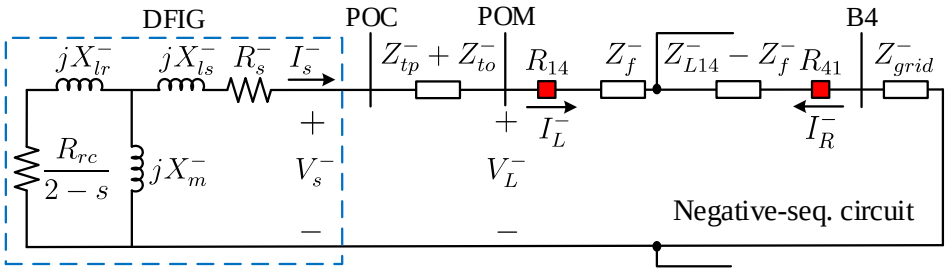

Figure 4.17: Permanent negative-sequence circuit of the test system for a BC fault on L14.

is small compared to the positive-sequence voltage in the positive-sequence circuit, it is proven to have a significant effect on the fault current of the machine [21], [78]. Using KVL for the circuit of Fig. 4.16, I_R^- is obtained as follows:

$$I_R^- = \frac{\left(Z_{st}^- + Z_{tp}^- + Z_{to}^- + Z_f^-\right) I_L^- - V_{st}^-}{Z_{L14}^- - Z_f^- + Z_g^-} \tag{4.13}$$

where $Z_{st}^- = R_s^- + j\omega L_{st}^-$ is the transient internal impedance of the DFIG. Due to the existence of V_{st}^- in the numerator of (4.13), I_R^- is not in phase with I_L^-. Consequently, jI_L^- does not represent the angle of the fault current, which results in wrong measurements of R_{BC} and X_{BC} in (4.12) and (4.11), respectively.

A similar analysis can be presented for the DFIG transient negative-sequence equivalent circuit during the rectification mode. However, as demonstrated in Section 4.2, the rotor time constant of the rectification mode is much shorter than that of crowbar activation mode. Therefore, the negative-sequence equivalent circuit shown in Fig. 4.16 is valid during the rectification mode as well, but for less than a cycle.

3) Reactance Method Operation After 1∼3 Cycles of Crowbar Activation

The steady-state equivalent negative-sequence circuit of the test system during crowbar connection for a BC fault on line L14 is illustrated in Fig. 4.17. In this figure, X_{ls} and X_{lr} are the stator and rotor leakage reactances, respectively. Depending on the rotor time constant, this circuit is valid after 1∼3 cycles of the fault inception till crowbar disengagement. Using KVL for the circuit of Fig. 4.17, I_R^- is obtained as

$$I_R^- = \frac{\left(Z_{sp}^- + Z_{tp}^- + Z_{to}^- + Z_f^-\right) I_L^-}{Z_{L14}^- - Z_f^- + Z_g^-} \tag{4.14}$$

where Z_{sp}^- is the DFIG's steady state negative-sequence impedance given by

$$Z_{sp}^- = \frac{\left(R_{rc}^-/(2-s) + jX_{lr}^-\right) jX_m^-}{R_{rc}^-/(2-s) + j\left(X_{lr}^- + X_m^-\right)} + R_s^- + jX_{ls}^- \tag{4.15}$$

in which $R_{rc} = R_r + R_c$ is the rotor total resistance. Given that the network impedances are highly inductive and so almost in phase, I_R^- and I_L^- in (4.14) have almost equal phase angles if Z_{sp}^- is highly inductive too. Based on (4.15), $\measuredangle Z_{sp}^-$ depends on crowbar resistance, i.e., R_c, and the rotor slip, i.e., s. As illustrated in Fig. 4.18, for the DFIGs of Fig. 4.1, $\measuredangle Z_{sp}^-$ is not necessarily inductive, especially, when the crowbar resistance increases. For example, for $s = 30\%$ and $R_c = 20R_r$, which is a typical value for R_c, $\measuredangle Z_{sp}^- = 78^\circ$. Since the phase angle of the negative-sequence impedance of the WF might be different than that of L14 and SGs impedances at the remote end of line L14, $\measuredangle I_R^-$ can deviate from $\measuredangle I_L^-$. Consequently, similar to the transient equivalent circuit, $\measuredangle jI_L^-$ does not provide a reliable estimate of $\measuredangle I_{F_{est}}$. Consequently, the relay may under/over-reach by measuring an incorrect R_{BC} and X_{BC}.

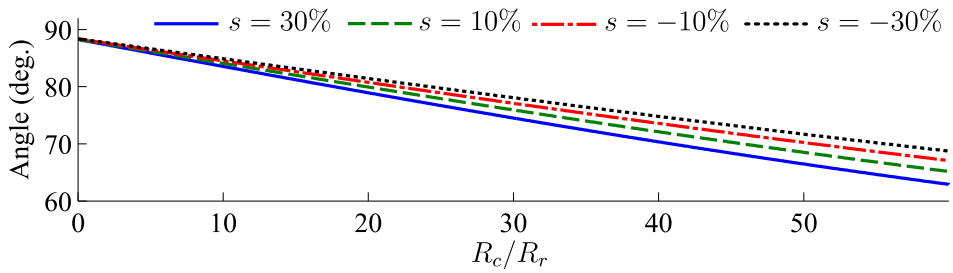

Figure 4.18: Phase angles of line L14 impedance and Z_{sp}^{-} for the DFIG with parameters given in Table A.1 for different crowbar resistances.

Fig. 4.17 is also valid for the rectification mode when R_c is replaced by R_{rec}. As illustrated in Fig. 4.18, $\measuredangle Z_{inp}^{-}$ significantly deviates from $\measuredangle Z_{L14}^{-}$ for higher R_c/R_r. The deviation reaches 23° for $R_c = 60R_r$, which is a possible scenario if the rectification mode is long enough.

It is to be noted that the transition between the two equivalent circuits in Figs. 4.16 and 4.17 is gradual. As the transient equivalent circuit's effect reduces from the beginning of the fault, the permanent equivalent circuit effect increases. However, the transient equivalent circuit's effect will be negligible after 0.5∼1 cycles depending on the mode of operation. Therefore, both of the equivalent circuits affect the behavior of distance relays.

To investigate the performance of DR14 with the reactance method, consider a BC fault at $t = 1.996$ s with $R_f = 8\ \Omega$ at 80% of line L14. The rotor speed is 1.2 pu right before the fault. The fault is in zone 1 of DR14. For this fault, crowbar is connected for 39 ms. Fig. 4.19 displays the estimated and measured angles of the fault current. This figure demonstrates that there is a significant discrepancy between $\measuredangle I_{F_{est}}$ and $\measuredangle I_F$. In addition, the estimated phase angle fluctuates as the negative-sequence current at POM contains the rotor-speed frequency components. The fluctuations reduce as the near rotor-frequency component dies out.

As a result of inaccurate estimation of $\measuredangle I_F$, the measured resistance and reactance, shown in

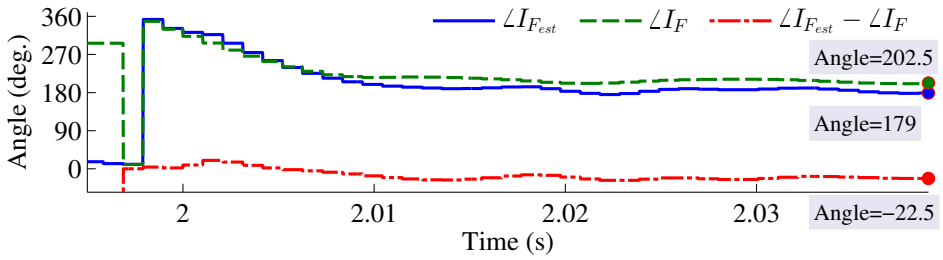

Figure 4.19: Estimated and measured angles of the fault current during the BC fault at 80% of line L14.

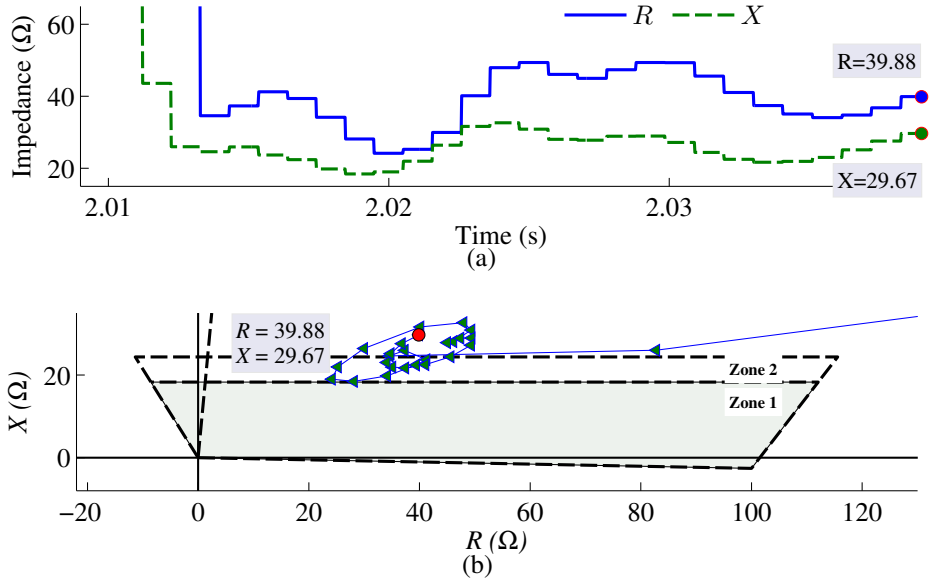

Figure 4.20: Performance of the BC element of DR14 with reactance method for the BC fault at 80% of line L14: (a) Impedance versus time, (b) Impedance trajectory.

Fig. 4.20(a), deviate from correct values. The fluctuations of the resistance and reactance are due to the rotor-speed frequency component of the fault current. The fluctuations are directly reflected in the impedance plane shown in Fig. 4.20(b). The measured impedance back and forth between the second and third zones and never enters the first zone of DR14. Consequently, DR14 fails to trip line L14 within the first 40 ms of the fault. The final value at the end of crowbar engagement is $Z_{BC} = 39.38 + j\ 29.67\ \Omega$, which is greater than $Z_f = 1.16 + j\ 15.25\ \Omega$ and results in the relay underreach.

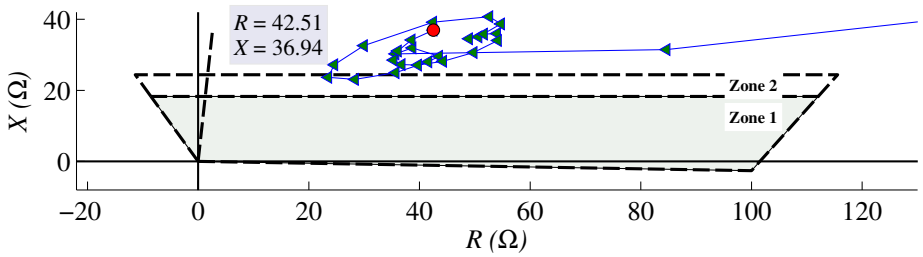

Figure 4.21: Impedance trajectory for the bolted BC fault at the second zone of DR14.

To further investigate the reactance method's performance during crowbar connection, consider the same BC fault of Fig. 4.2 at zone 2 of DR14. Fig. 4.21 depicts the impedance measured by DR14. It can be seen that, similar to Fig. 4.20(b), the measured impedance revolves around the final value. The measured impedance enters the second zone 22.5 ms after the fault inception but leaves it in 4 ms before the 300 ms time delay is passed. Thus, DR14 fails to operate as backup protection.

Finally, to investigate the performance of the reactance method during the rectification mode, the crowbar is turned off and the same BC fault of in Section 4.2 is applied, but with zero fault resistance. The rectification mode is triggered 3 ms after the fault inception and lasts for 17 ms. Fig. 4.22 illustrates the estimated and measured phase angles of the fault current during the rectification mode. Similar to crowbar connection mode, $\measuredangle I_{F_{est}}$ is significantly deviated from $\measuredangle I_F$, due to the presence of V_{st}^{-} and R_{rec}. The deviation reaches 20° 9 ms after the fault inception. The estimated angle keeps changing due to both the variable nature of R_{rec} and the rotor-speed frequency component of the fault current.

Similar to crowbar connection time, the rotor-speed frequency component's existence leads to fluctuation of the fault current and voltage phasors. These fluctuations along with the inaccurate estimation of $\measuredangle I_F$ lead to inaccurate measurement of the impedance to the fault, as displayed in Fig. 4.23. The measured impedance enters zone 1 of DR14 19 ms after the fault inception, leading to

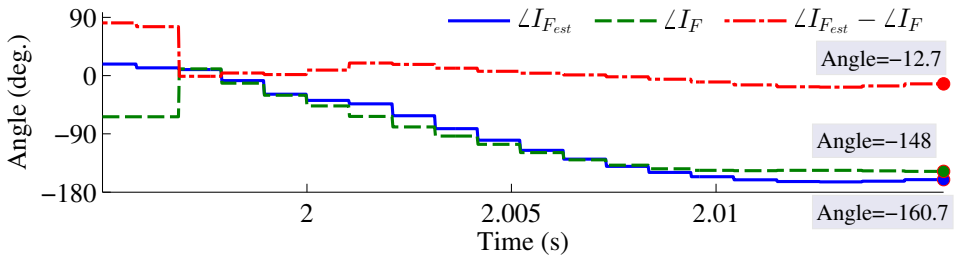

Figure 4.22: Estimated and measured angles of the negative-sequence current during the rectification mode for the BC fault.

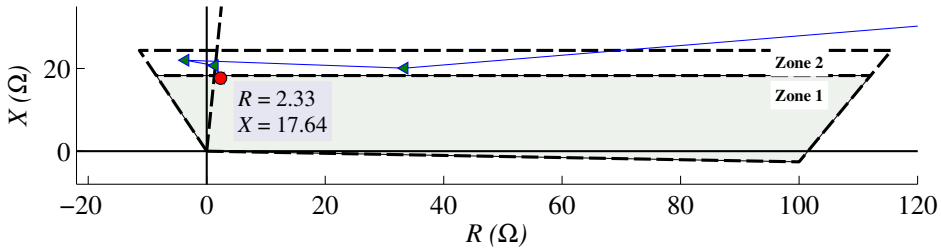

Figure 4.23: Impedance trajectory for the BC fault during rectification mode.

the false instantaneous trip of the line L14. The overreaching level could be different if a longer rectification time is set in place by a different control strategy. Besides, even if the measured impedance did not enter zone 1 of DR1, the relay is still prone to maloperation depending on the control scheme used for control resumption of the rotor currents.

The simulations are repeated for different types of faults with different fault resistances, different rotor speeds, and other operating conditions affecting the fault currents of the DFIGs. In most cases, the impedance trajectories in the impedance plane display an unreliable behavior.

4) Line-to-Ground Faults

The resistance and the reactance of the ground element measured by the reactance method during, for example, AG faults are given by (4.17) and (4.16), respectively [71].

$$X_{AG} = \frac{\mathrm{Im}[V_A \bar{I}_{F_{est}}]}{\mathrm{Im}[Z^+_{L14}(I_A - K^0 I^0)\bar{I}_{F_{est}}]} |Z^+_{L14}| \sin(\measuredangle Z^+_{L14}) \tag{4.16}$$

$$R_{AG} = \frac{\mathrm{Im}[V_A \overline{\left(Z^+_{L14}(I_A - K^0 I^0)\right)}]}{\mathrm{Im}[I_{F_{est}} \overline{\left(Z^+_{L14}(I_A - K^0 I^0)\right)}]} |Z^+_{L14}| \cos(\measuredangle Z^+_{L14}) \tag{4.17}$$

During SLG faults, $I_{F_{est}}$ is estimated using $3I^0$, or $3I^-$, or $1.5I^0 + 1.5I^-$.

As mentioned earlier in Section 4.2, the tracked frequency remains stable and with minimal oscillations during SLG faults, and the voltage is of the fundamental frequency type. As the off-nominal frequency component of $I_A + K^0 I^0$ is much smaller than the fundamental frequency component, the accuracy of X_{AG} in (4.16) depends on $I_{F_{est}}$. If the fault current is estimated through $3I^0$ or $1.5I^0 + 1.5I^-$, the off-nominal frequency in (4.16) will be minimal. In addition, if $I_{F_{est}}$ is estimated by $3I^0$ or $1.5I^0 + 1.5I^-$, the zero-sequence current will be dominant. Therefore, the effect of negative-sequence equivalent circuit characteristics, discussed in the previous section, on $\measuredangle I_{F_{est}}$ will be minimal. Similar analysis can be presented for R_{AG} in (4.17). Therefore, the impedance measured using the reactance method during SLG faults will have minimal oscillations when the fault current is estimated by $3I^0$ or $1.5I^0 + 1.5I^-$.

As demonstrated in the previous subsection, the DFIG equivalent negative-sequence circuit as well as the crowbar resistance affect the angle of the estimated fault current, i.e., $I_{F_{est}}$, when it is

estimated by the negative-sequence current at the relay location. Consequently, as both numerator and denominator of X_{AG} in (4.16) and the denominator of R_{AG} in (4.17) are multiplied by $I_{F_{est}}$, the measured impedance by the reactance method may deviate/oscillate. As mentioned earlier in Section 4.2, the crowbar connection time depends on the magnitude of the stator dc flux, i.e., $\vec{\psi}_{s,\mathrm{dc}}$. Since $\vec{\psi}_{s,\mathrm{dc}}$ during SLG faults is mall, the crowbar connection or the rectification mode does not last for more than a cycle. Therefore, the RSC controllers will take the control of the DFIG before the DFIG experiences the permanent negative-sequence circuit during the crowbar or the rectification mode connection. Consequently, the transient negative-sequence circuit of the DFIG during the first cycle of the SLG fault, which is similar to the circuit shown in Fig. 4.16, is the only factor that can affect $\angle I_{F_{est}}$, and thus, the measured impedance to the fault. As mentioned earlier in this section, V_{st}^{-} in Fig. 4.16 depends on the rotor negative-sequence flux. Since the rotor negative-sequence flux is smaller compared to phase-to-phase fault discussed in this section, V_{st}^{-}, and thus, its effect in (4.13) will be negligible. Therefore, I_L^- will be almost in phase with I_R^- in the transient negative-sequence circuit of the DFIG shown in Fig. 4.16.

To elaborate on the above analysis, consider an AG fault at 25% of line L14 with $R_f = 10$ Ω at $t = 2$ s. As the worst condition, the fault current is estimated by $3I^-$ at the relay location. For this fault, the crowbar is activated 5 ms after the fault inception and remains active for 16 ms. The impedance between the relay and the fault is $Z_{AG} = 0.358 + j5.078$ Ω. Fig. 4.24 shows the measured impedance for the AG fault. As can be seen in this figure, the reactance calculated with DR14 is only 1.34 Ω larger than the actual impedance to the fault. The impedance enters zone 1 in less than 15 ms and settles in its final position with minimal oscillation. Therefor, DR14 operates

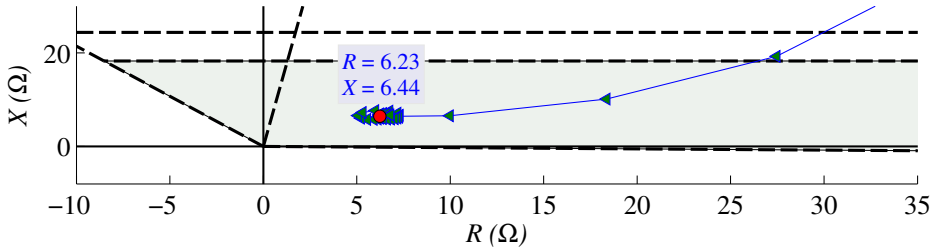

Figure 4.24: Impedance trajectory for the AG element of DR41 at the remote end of line L14.

correctly for LG faults.

4.5 Proposed Solution

This section proposes a new method to address the misoperation of the distance relays connected to DFIG-based WFs, unveiled in the previous sections. The objective of the proposed method is to obtain a non-delayed fast protection over the entire line length with minimal bandwidth requirements. The following first describes the layout of the modifies POTT scheme. Then, the details of the proposed fault direction identification (FDI) technique used by the modifies POTT scheme are discussed.

4.5.1 Modified POTT scheme

Distance relays at the two ends of a line are generally able to communicate through a low-bandwidth communication channel. Various pilot schemes use this channel to provide a non-delayed trip over 100% of the line length. Among them, POTT scheme is widely used in practice due to its relatively low price, and a very low bandwidth requirement [20].

According to the conventional POTT scheme, if the measured impedances by DR14 and DR41

at the two ends of the line L14 fall within their second zones, there is a fault on line L14. Thus, once DR41 detects a fault at its second zone, it sends a trip signal to DR14. DR14 will trip only if the received signal accompanies a fault in its second zone of protection. The same principle is also applied for DR41.

For a fault on line L14 in Fig. 4.1, DR41 can correctly measure the impedance to the fault as its input signals have the conventional SGs fault characteristics. DR14, however, fails to accurately measure the impedance to the fault due to the specific fault characteristics of DFIGs. As a solution, a modified POTT scheme is developed. In the modified POTT scheme, DR41 operation principle remains the same. However, the relay at the WF location, i.e., DR14, detects faults in its forward direction not based on the measure impedance by the relay, but according to the frequency characteristics of the DFIG fault signals described in Section 4.3.

Fig. 4.25 illustrates the decision-making process of DR14 based on the modified POTT scheme during crowbar connection or the rectification mode. This scheme is initiated by a high-speed disturbance detector (DD) unit developed in [79]. Once a fault is detected, the algorithm investigates the direction of the fault according to the fault direction identification (FDI) method later described in this section. If the FDI does not identify the DFIG fault signals during the crowbar connection or the rectification mode, either the crowbar or the rectification mode is not activated or there is a reverse fault inside the WF. In such condition, the modified POTT scheme is not activated and DR14 operates based on local measurements. If the FDI technique identifies the DFIG fault signals during crowbar connection or the rectification mode of operation, the fault lies in the forward direction of DR14, and it sends a trip signal to DR41. If such condition is accompanied by the

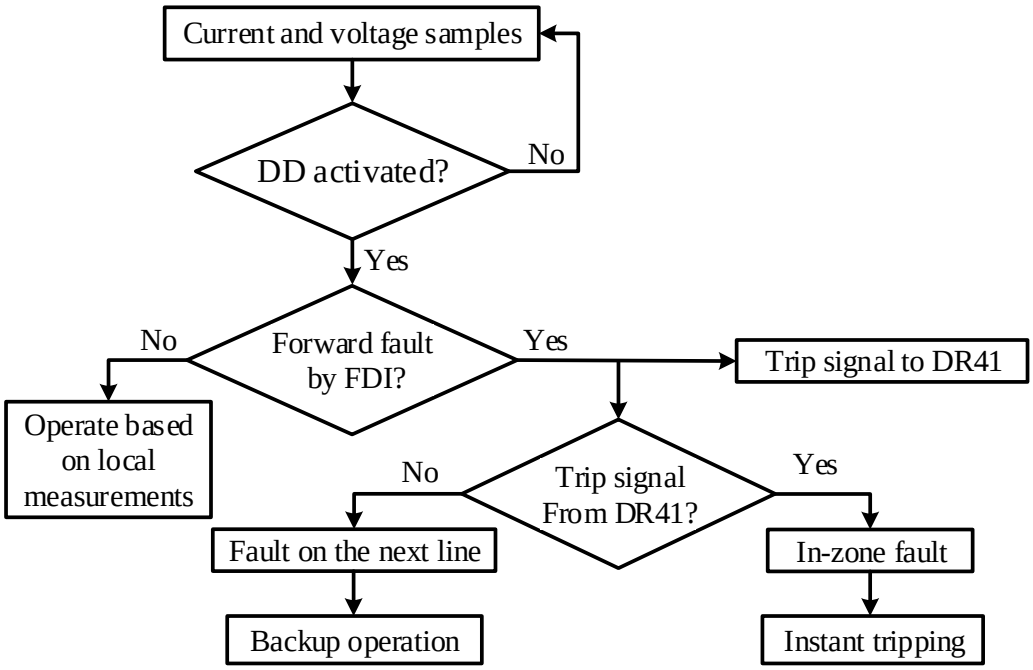

Figure 4.25: Proposed method for DR14 operation during the crowbar connection or the rectification mode of operation.

receipt of a signal from the remote end relay, i.e., DR41, DR14 trips the line L14. Otherwise, the fault is on the neighboring line and DR14 would operate as a backup protection with a typical time delay of 300 ms. Similarly, DR41 issues a trip command if it detects a fault in its second zone and simultaneously receives a trip signal from DR14. As a result of this communication between DR14 and DR41, a non-delayed fast trip over the entire line length is obtained. It should be noted that the instantaneous tripping of DR41 is blocked if the relay detects the DFIG fault signals during the crowbar connection or the rectification mode to prevent maloperation of DR41 for reverse faults.

4.5.2 Proposed FDI Method

This section proposes a new FDI method to determine the fault signals of the DFIG, and hence, the direction of the faults. As discussed in Section 4.3, during the crowbar connection or the

rectification mode, the measured frequency of the DFIG fault current asymmetrically oscillates around the nominal frequency while the voltage frequency is relatively constant. These current and voltage frequency characteristics of the DFIG's fault signals are used by the FDI to determine if the fault signals are coming from the DFIGs during the crowbar connection or the rectification mode. The following describes the logic behind the proposed FDI method.

According to the proposed FDI, if the frequencies of the both voltage and current measured by DR14 remain within a narrow margin of the fundamental frequency, either the crowbar or the rectification mode is activated while the DFIGs are working with a slip close to zero, or control systems of the DFIGs have not been interrupted and the RSCs keep the frequency of the current at the POM close to the nominal frequency. In such a condition, the output of FDI is 0, meaning that the fault direction is not determined and the modified POTT scheme shown in Fig. (4.25) is not activated. Therefore, DR14 measures the impedance to the fault based on the local measurements of the current and voltage. If the measured frequency of the current by DR14 deviates large enough form the synchronous frequency while the voltage frequency is within a narrow margin of the nominal frequency, DR14 measurements are coming from the DFIGs during the crowbar connection or the rectification mode. Therefore, the FDI declares a forward fault and activates the proposed POTT scheme. Extensive simulation analysis though different case studies, considering different variables and operating conditions that affect the DFIG fault current, show that a margin of ± 1 Hz around the nominal frequency is a reliable indicator of the crowbar connection or the rectification mode of operation.

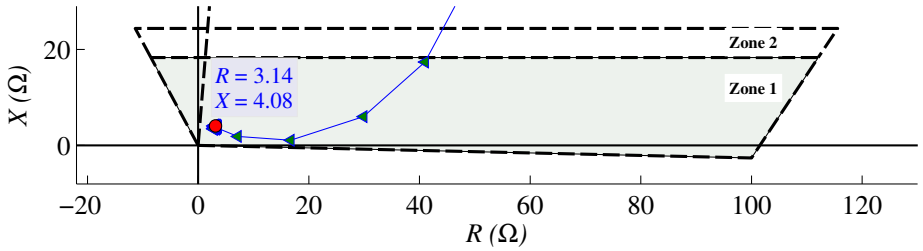

Figure 4.26: Apparent impedance calculated by the AG element of DR14.

4.6 Performance Evaluation

The performance of the proposed modified POTT scheme was tested for different conditions in the test system of Fig. 4.1. Various fault locations, fault types, fault resistance, crowbar resistance, the DFIGs operating modes, fault phase angle, and short circuit ratios (SCRs) at the POM were investigated. The results show that the line connected to the DFIG-based WF is protected within one to two cycles after fault inception. The following presents the performance of DR14 in Fig. 4.1 when it is equipped with the proposed modified POTT scheme as well as discusses the most crucial issues that can affect the performance of the proposed POTT scheme.

4.6.1 Performance of DR14

Consider the BC fault studied at the end of Section 4.2.1. That case is repeated for DR14 equipped with the modified POTT scheme and DR41 equipped with the conventional POTT scheme. Fig. 4.26 shows the measured impedance by DR41. As shown in Fig. 4.26, the impedance quickly enters inside zone two of DR41 (within 10 ms), indicating a fault in its directional overreaching zone. Therefore, DR41 sends a trip signal to DR14, as shown in Fig. 4.27.

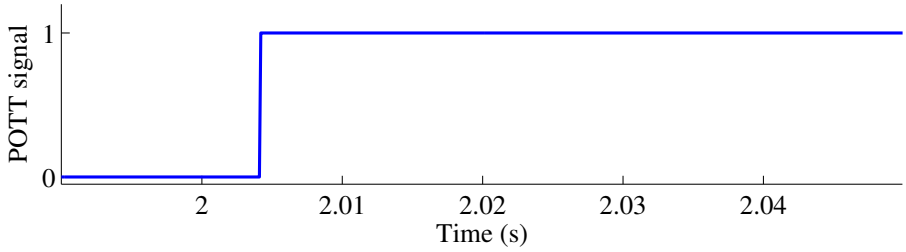

Figure 4.27: Permissive signal sent to DR14 by the remote relay DR41.

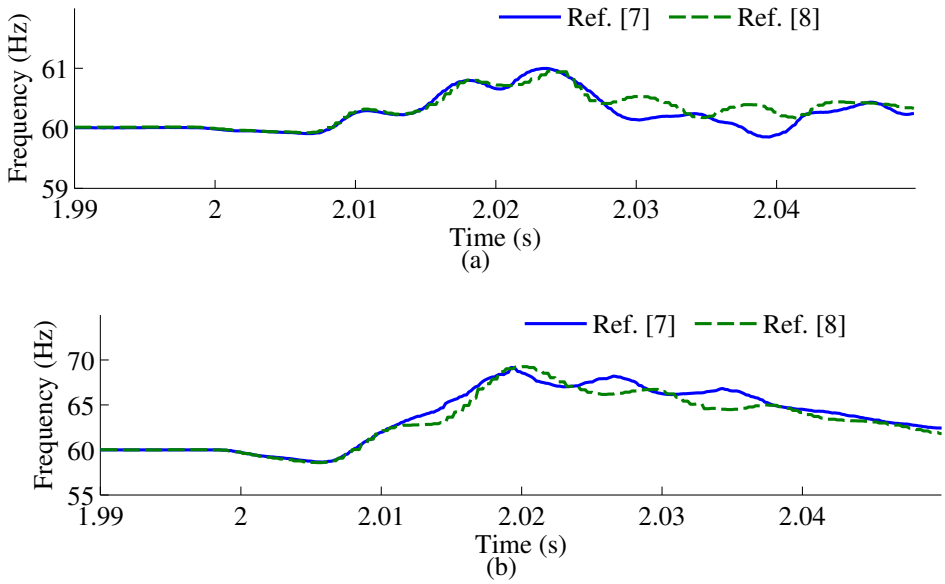

Figure 4.28: The frequency measured by methods in [8] and [9] for the BC fault on Line L14 with R_f =8 Ω: (a) voltage, (b) current.

Fig. 4.28 shows the voltage and current frequencies measured by DR14 using the methods in [8] and [9]. This figure shows that the voltage frequency remains within the margin of ± 1 Hz around the nominal frequency while the current frequency largely deviates from the fundamental frequency. Therefore, FDI declares a forward fault during the crowbar connection within 14 ms as shown in Fig. **??**. Since, the forward fault condition is accompanied by the receipt of a signal from the remote end relay in Fig. 4.27, DR14 trips the line L14 14 ms after the begging of the fault.

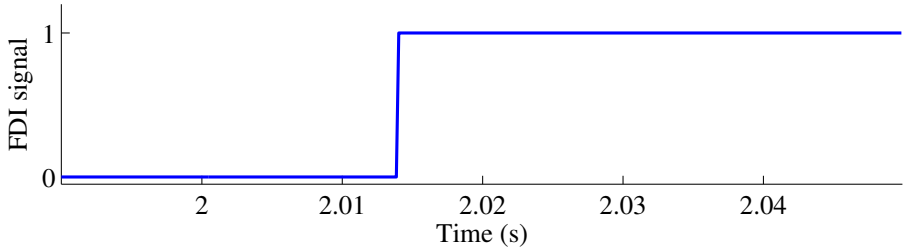

Figure 4.29: FDI signal for the the BC fault on Line L14 with R_f =8 Ω.

4.6.2 Effect of Loss of Generation or Power System Overloading

In some specific conditions, for example, during loss of generation or power system overloading, the frequency of the current and voltage may deviate from the nominal frequency. In such a condition, since the frequency deviation of the current is accompanied by the same rate of frequency deviation of the voltage, the output of the proposed FDI described in Subsection 4.5.2 is 0, and no forward fault is declared. However, if both frequency of the current and voltage largely deviate from the nominal frequency but with different deviation/oscillation rate, a forward fault is declared by the FDI and the modified POTT scheme described in Fig. (4.25) is activated. This scenario can happen when the DFIGs are connected to a relatively weak grid, where the voltage frequency also largely deviates from the nominal frequency.

4.6.3 Effect of Crowbar Resistance

For the DFIG fault currents discussed so far, the crowbar resistance was 20 times of the rotor resistance. $R_c = 20R_r$ is the maximum R_c used for the DFIG with the parameters given in the Appendix. Meanwhile, smaller crowbar resistances may be used in practice. As discussed in Section 4.2, the rotor frequency component of an actual DFIG fault signal decays over time with the rotor

time constant, T_r. According to (4.4), smaller crowbar resistance results in larger rotor time constant. Therefore, the variation of the frequency measured by the relay from the fundamental frequency declines slower when the crowbar resistance is smaller. Such situation will not have any negative effect on operation of the proposed method.

4.7 Conclusion

This chapter showed that the Crowbar connection or rectification mode results in appearance of the rotor-speed frequency component in the fault current and voltage of a DFIG. It was unveiled that the existence of the rotor-speed frequency component results in asymmetrical oscillation of the measure frequency by the commercial frequency tracking methods at the WF substation. In addition, it was demonstrated that the existence of the off-nominal frequency component in the DFIG fault signals results in unequal oscillations in the fundamental-frequency phasors of currents and voltages, which leads to maloperation of distance relays operating based on apparent impedance calculation method. It was revealed that the equivalent sequence circuits of DFIGs are different than that of SGs upon which commercial distance relays with reactance method is developed. The appearance of a decaying negative-sequence voltage source behind the stator transient reactance in the transient negative-sequence circuit of DFIGs along with variable nature of the DFIG negative-sequence impedance during the interrupted control of the RSC results in inaccurate estimation of the fault current angle at the relay location. Such a wrong estimation results in the relay under-/over-reach in the presence of DFIGs. This chapter also proposed a modified POTT scheme to provide a fast non-delayed protection over the entire line length, where a minimal bandwidth for communication

between the relays was used. While the remote end relay uses an impedance-based overreaching zone, the relay at the WF substation detects the fault direction according to the measured frequency properties of the DFIG fault signals. The performance of the proposed method was also investigated under different fault conditions and promising results were obtained.

Chapter 5

Conclusion

5.1 Summary

This dissertation investigated the challenges associated with the control and GC compliance of the DFIGs as well as their impact on distance relays. The studies were based on time-domain simulation of the mainstream established control strategies used by DFIG manufacturers as well as commercial digital relays using PSCAD/EMTDC. The main objectives of this study were threefold: (i) unveiling several previously unknown DFIG characteristics that impact their LVRT behaviour and GC compliance, (ii) revealing the negative impacts of the DFIG unique fault characteristics on relays, and (iii) developing new solutions to overcome these challenges. These objectives were achieved by focusing on the following subjects:

1. *Investigating the effect of the CVC-based DFIG control system on the phase difference between the negative-sequence current and voltage at the POC.* It was proven that why/how the control

system of the RSC considerably deviates the phase difference between the negative-sequence current and voltage from its ideal [90°, 100°] range for a DFIG with CVC. However, it was demonstrated that the negative-sequence current angle for a DFIG with CVC is within the extended [90°, 150°] range allowed by the 2800 Standard for DFIGs.

2. *Investigating the effect of the DCC-based DFIG control system on the phase difference between the negative-sequence current and voltage at the POC.* It was unveiled that the available DFIG control methods with suppression of the second harmonic ETPs during unbalanced LVRT condition could move the angle between the negative-sequence current and voltage well beyond even the extended [90°, 150°] range allowed by the 2800 Standard for DFIGs.

3. *Investigating the possible negative impacts of the DFIG control system on distance relays elements.* It was revealed that the protection systems can be impacted by the exemption made by IEEE 2800 Standard, i.e., 90°–150° phase difference between the negative-sequence current and voltage at the DFIG terminals, during LVRT condition. As a specific case, it was shown that the phase selection elements, which are sensitive to variations of the negative-sequence current angle, are not able to identify the fault type when the mainstream established control strategies used by DFIG manufacturers are used.

4. *Modifying the control system of the DFIG to address the aforementioned problems.* A simple yet effective control scheme was developed for the GSC to move the phase difference between the negative-sequence voltage and current of a DFIG to the ideal [90°, 100°] range. This

would obviate the need to exempt the DFIGs from this requirement in the future revisions of the 2800 Standard. As a Representative case, it was also shown that the proposed method results in correct operation of phase selection element of relays.

5. *Distance protection of lines adjacent to DFIG-based WFs during unbalanced faults and interrupted control of DFIGs.* A detailed analysis was provided on the impact of DFIGs on distance relays implemented using the apparent impedance calculation and the commercially developed reactance methods. It was unveiled that the phase elements of these methods are prone to under-/over-reach during interrupted control of DFIGs. It was shown that the problem originates from the unconventional fault behaviour of DFIGs, which affects the impedance measurement relations used by a distance relay. A new method was proposed to address this problem such that a fast non-delayed distance protection over the lines connected to the DFIG-based WFs is achieved. The proposed method uses the commonly available communication links with minimal bandwidth between the relays at the two end of the line.

5.2 Contributions

The contributions fall roughly into three categories: (i) diagnosis of several so-far-unknown DFIG characteristics that impact their LVRT behaviour and GC compliance, (ii) unveiling the negative impacts of the DFIG unique fault characteristics on relays, and (iii) proposal of solutions to address them.

5.2.1 Diagnosis of Several So-far-Unknown DFIG Characteristics

The following lists the DFIG characteristics that impact their LVRT behaviour and GC compliance unveiled, for the first time, by this dissertation.

1. It was unveiled in Chapter 3 that why/how the angle of a DFIG's negative-sequence current during LVRT deviates from the ideal [90°, 100°] range. For the CVC-based DFIG schemes, the deviation is primarily determined by the bandwidth of the RSC's current control loop. It was shown that for smaller bandwidths, the deviation of the angle from the ideal range of [90°, 100°] is small. The deviation of the angle from the [90°, 100°] range increases commensurate with the bandwidth of the RSC's current control loop. For this scheme, the negative-sequence current angle stays within the wider [90°, 150°] range allowed for DFIGs by the 2800 Standard.

2. It was unveiled in Chapter 3 that if the DFIG uses DCC scheme for the RSC to suppress the ETPs, the angle between the negative-sequence current and voltage could move well beyond even the extended [90°, 150°] range allowed by the 2800 Standard for DFIGs. This would violate the 2800 Standard, even with the exemption. This would also result in generation of capacitive negative-sequence reactive current at the POC, despite general assumption made by some GCs about DFIG negative-sequence reactive current. This chapter also found all possible ranges for the angle of the DFIG negative-sequence current.

3. It was shown in Chapter 4 that, from the rotor perspective, the rectification mode of a DFIG can be modeled as a resistance in each phase. This resistance varies depending on the induced

rotor voltage and its frequency during a grid fault. It was also shown that the initial value of this resistance is roughly equal to commonly used crowbars. However, the resistance increases as the induced rotor voltage decays by time. The analysis showed that the fault signals of the DFIG during the rectification mode is chiefly similar to that of the crowbar connection except that the rotor time constant of the crowbar fault signals is replaced by the equivalent resistance of the rectification mode.

5.2.2 Diagnosis of Relay Failures

The followings are among the failures of the existing distance protection schemes in the presence of the DFIGs that this dissertation has identified.

1. Chapter 3 unveiled that the protection functions dependent on negative sequence quantities can be impacted by the exemption made by IEEE 2800 Standard during LVRT of DFIGs, i.e., 90°–150° phase difference between the negative-sequence current and voltage at the DFIG terminals. As a specific case, it was shown that the commercial current angle-based faulty phase selection elements that operate based on the angle difference between the sequence currents are not able to identify the fault type when the mainstream established control strategies used by DFIG manufacturers are used.

2. Chapter 4 demonstrated that the instantaneous frequency of a signal that contains an off-nominal frequency component oscillates asymmetrically around the more dominant frequency component. The rate of oscillations in Hz is the difference between the two frequencies. It was also shown that in the case of the DFIG fault signals that contain the rotor speed frequency

component of 42∼78 Hz in a 60 Hz system, the measured frequency by the frequency tracking elements of relays asymmetrically oscillates around the more dominant frequency component with a frequency of 0∼18 Hz. However, since the rotor frequency component of an actual DFIG fault signal decays over time with the rotor time constant, the variation of the frequency measured by the relay from the fundamental frequency declines at the same rate.

3. It was shown in Chapter 4 that the existence of the rotor-speed frequency component in the DFIG fault signals and their impact on frequency tracking methods during unbalanced faults and interrupted control of the DFIGs result in oscillations of the current and voltage phasors measured by phasor measurement units of relays. The oscillations of the current and voltage phasors are different as the frequency of the fault voltage is mainly dictated by the grid and is close to the nominal frequency while the fault current contains high magnitude rotor speed frequency component. For phase elements, the oscillatory phasors of current and voltage make the phasor-based relations upon which distance relays implemented using the apparent impedance calculation method fail to calculate a meaningful impedance. The measured impedance is such that results in the relay overreach and unnecessary WF tripping, and thus, failing to ride through the fault and fulfill the GCs requirements.

   During LG faults, the fundamental frequency component dominates the denominator of the phasor-based relations on which distance relays are founded due to the flow of a large zero-sequence current from the neutral winding of the WF's main step-up transformer. Therefore, the rotor-speed frequency component of the DFIG fault signals during SLG faults does not considerably affect the apparent impedance measured by distance relays.

4. It was shown in Chapter 4 that the equivalent sequence circuits of the DFIG has two transient and permanent stages. While the transient stage starts at the instant of the fault inception and lasts for the first 1$\sim$3 cycles, the permanent circuit is valid after 1$\sim$3 cycles of the fault inception till crowbar disengagement. During transient stage, a decaying negative-sequence voltage appears behind the stator transient reactance, despite to SGs' negative-sequence circuit upon which distance relays with the reactance methods are developed. The existence of the decaying voltage results in wrong estimation of the angle of the fault current by the phase elements of the distance relay at the DFIG substation.

   During permanent stage, it was shown that the estimation of the fault current angle by the relay depends on the angle of the DFIG negative-sequence impedance, which was shown to be variable and different than that of SGs. Consequently, the relay at the DFIG substation also fails to accurately estimate the angle of the fault current during crowbar connection or the rectification mode. Such a wrong estimation results in the relay under-/over-reach in the presence of DFIGs.

   Similar to the apparent impedance method discussed above, due to the flow of a large zero-sequence current from the neutral winding of the WF's main step-up transformer, the equivalent circuits of the DFIG during SLG faults does not considerably affect the impedance measured by the reactance method.

5.2.3 Proposal of Solutions

This dissertation has presented the following solutions to address the GC compliance as well as the unveiled challenges for distance relays of system with DFIGs.

1. Chapter 3 developed a control system for the GSC to move the phase difference between the negative-sequence current and voltage of a DFIG to the ideal [90°, 100°] range while the ETPs are suppressed to the maximum extent possible. This would obviate the need to exempt the DFIGs from this requirement in the future revisions of the IEEE 2800 Standard without imposing a prohibitive cost on DFIG manufacturers. The solution is comprehensive and capable of addressing both positive- and negative-sequence current requirements of the GCs. It does not require a hardware upgrade either. Further, it awards correct operation of the relays' elements that operate based on negative-sequence quantities, such as phase selection elements. This chapter also proved the feasibility of this solution for realistic DFIGs. As the proposed method leaves the RSC control intact, the DFIG manufacturer can use either the well-established CVC scheme or the DCC method to suppress the ETPs.

2. A modified POTT scheme was proposed in Chapter 4 to address the revealed problems for distance relays during unbalanced faults and interrupted control of DFIGs. In this scheme, while the remote end relay uses an impedance-based overreaching zone, the relay at the WF substation uses the current and voltage frequency characteristics of the DFIGs' fault signals to determine the fault direction, i.e., if the fault signals are coming from the DFIGs during the crowbar connection or the rectification mode of operation. The modified POTT scheme

awards a fast non-delayed protection over the entire line length while uses a low-bandwidth communication channel between the distance relays.

5.3 Future Works

Further research on IBRs control and protection can be listed as:

1. Investigating the IEEE 2800 compliance of DFIGs during interrupted control of the RSCs. It should be investigated how the crowbar activation and deactivation affects the angle between the negative-sequence current and voltage at the POC. It is important to realize how fast the DFIG is able to fix the angle to 90° when the crowbar gets activated.

2. Proposal of a new solution that uses only local measurements of the distance relay during interrupted control of the DFIGs. Using local measurements of the fault currents and voltages at the DFIG substation will increase the dependability of the distance relays as they would no longer rely on the data from the remote relay.

3. Investigating the distance protection of lines connected to DFIG-based WFs during uninterrupted control of both CVC- and DCC-based DFIGs. Since DFIGs are modeled as current sources, the angle between the fault currents at the two ends of the line can largely deviate, despite SG-based systems. This large deviation of the angle would negatively impact the impedance measured to the fault, and may result in overreach or underreach of the relay.

4. Investigating the operation of other types of distance relays, such as phase comparator method, during interrupted and uninterrupted control of the DFIGs.

APPENDICES

Appendix A

WIND-TURBINE GENERATOR

PARAMETERS

Table A.1: **Type-III WT parameters [1].**

Wound-Rotor Induction Machine Parameters			
Quantity	**Symbole**	**Value**	Unit
Rated Power	P	1.5	MW
Stator Voltage (L-L RMS)	V_s	690	V
Stator Resistance	R_s	0.00706	pu
Stator Leakage Reactance	X_{ls}	0.171	pu
Magnetizing Reactance	X_m	2.9	pu
Rotor Resistance	R_r	0.005	pu
Rotor Leakage Reactance	X_{lr}	0.156	pu
Stator/Rotor Turns Ratio	N_s/N_r	0.38	-
Inertia	J	5.04	Sec.
GSC Parameters			
Filter Resistance	R_g	0.0104	pu
Filter Inductance	L_g	1.9578	mH
Filter Capacitance	C_f	500	\mu F
DC-Link Voltage	V_{dc}	1200	V(dc)
GSC Maximum Current	$I_{g,max}$	0.525	pu
DC-Chopper Resistance	R_{sh}	0.6	pu
DC-Chopper Turn-on/Turn-off Voltage	V_{con} V_{coff}	1320 1300	V(dc)
RSC Parameters			
RSC Maximum Current	$I_{r,max}$	1.5	pu
DC Crowbar Resistance	$R_{c,dc}$	0.165	pu
Crowbar Threshold Current	I_c	1.5	pu

Appendix B

List of Publications

The following is a list of publications by the author from this dissertation:

- H. Mohammadpour, A. Banaiemoqadam, A. Hooshyar and A. Al-Durra, "Eliminating the Need for a Less Strict Requirement for the Negative-Sequence LVRT Current of Type-III Wind Turbine Generators in the IEEE 2800 Standard," Submitted to *IEEE Trans. on Sustain. Energy*.

- H. Mohammadpour, A. Banaiemoqadam and A. Hooshyar, "Distance Protection of Lines Connected to DFIG-Based Wind Farms During Interrupted Control of DFIGs," Ready for submission to *IEEE Trans. on Power Del*.

Bibliography

[1] J. Hu, Y. He, L. Xu, and B. W. Williams, "Improved control of DFIG systems during network unbalance using PI–R current regulators," *IEEE Trans. Ind. Electron.*, vol. 56, no. 2, pp. 439–451, Feb. 2009.

[2] "Technical requirements for the connection and operation of customer installations to the extra high voltage network," VDE-AR-N 4130, Berlin, Germany, Nov. 2018. [Online]. Available: https://bit.ly/2SKOoD6

[3] *Instruction manual: GE Multilin, D60^{Plus} line distance protection system*, General Electric (GE), Canada, July 2021. [Online]. Available: https://www.gegridsolutions.com/app/viewfiles.aspx?prod=d60&type=3

[4] L. Xu and Y. Wang, "Dynamic modeling and control of DFIG-based wind turbines under unbalanced network conditions," *IEEE Trans. Power Del.*, vol. 22, no. 1, pp. 314–323, Feb. 2007.

[5] H. Mohammadpour, S. Ghassem Zadeh, and S. Tohidi, "Symmetrical and asymmetrical low-voltage ride through of doubly-fed induction generator wind turbines using gate controlled

series capacitor," *IET Renew. Power Gen.*, vol. 9, no. 7, pp. 840–864, Aug. 2015.

[6] *Type 3 Wind Turbine Model*, Manitoba Hydro International Ltd., Nov. 2018. [Online]. Available: https://www.pscad.com/knowledge-base/article/496

[7] G. Abad, J. Lopez, M. Rodriguez, L. Marroyo, and G. Iwanski, *Doubly Fed Induction Machine: Modeling and Control for Wind Energy Generation Applications*. Wiley-IEEE Press, 2011.

[8] D. Hart, Y. Hu, D. Novosel, and R. Smith, "System and method for phasor estimation and frequency tracking in digital protection systems," U.S. Patent 5 721 689, Feb. 24, 1998.

[9] B. Z. Kasztenny, "Frequency measurement for electric power delivery system," U.S. Patent 10 312 041B2, Jun. 4, 1998.

[10] "IRENA (2022), renewable energy statistics 2022," The International Renewable Energy Agency, Abu Dhabi, 2022. [Online]. Available: //www.irena.org/publications/2022/Apr/Renewable-Capacity-Statistics-2022

[11] *Requirements for Generating Plants to be connected in parallel with distribution networks - Part 2: Connection to a MV distribution network - Generating plants up to and including Type B*, CLC/TC 8X, Brussels, Jan. 2019. [Online]. Available: https://bit.ly/31E3tTb

[12] *IEEE Standard for Interconnection and Interoperability of Inverter-Based Resources (IBRs) Interconnecting with Associated Transmission Electric Power Systems*, IEEE Std 2800, April 2022. [Online]. Available: https://ieeexplore.ieee.org/document/9762253

[13] A. Hooshyar, M. A. Azzouz, and E. F. El-Saadany, "Distance protection of lines emanating from full-scale converter-interfaced renewable energy power plants–Part I: Problem statement," *IEEE Trans. Power Del.*, vol. 30, no. 4, pp. 1770–1780, Aug. 2015.

[14] B. Kasztenny, M. V. Mynam, and N. Fischer, "Sequence component applications in protective relays—Advantages, limitations, and solutions," in *46th Annual Western Protective Relay Conference*, Oct. 2019.

[15] D. Costello and K. Zimmerman, "Determining the faulted phase," in *63th Annu. Conf. for Protective Relay Eng.*, March 2010, pp. 1–20.

[16] J. Lopez, E. Gubia, P. Sanchis, X. Roboam, and L. Marroyo, "Wind turbines based on doubly fed induction generator under asymmetrical voltage dips," *IEEE Trans. Energy Convers.*, vol. 23, no. 1, pp. 321–330, March 2008.

[17] A. Bucker, W. Janssen, and H. Lutze, "Method for operating a wind power plant and method for operating it," U.S. Patent 7 321 221B2, Jan. 22, 2008.

[18] J. Vidal, G. Abad, J. Arza, and S. Aurtenechea, "Single-phase DC crowbar topologies for low voltage ride through fulfillment of high-power doubly fed induction generator-based wind turbines," *IEEE Trans. Energy Convers.*, vol. 28, no. 3, pp. 768–781, Sept. 2013.

[19] G. Pannell, B. Zahawi, D. J. Atkinson, and P. Missailidis, "Evaluation of the performance of a dc-link brake chopper as a dfig low-voltage fault-ride-through device," *IEEE Trans. Energy Convers.*, vol. 28, no. 3, pp. 535–542, May 2013.

[20] A. Hooshyar, M. A. Azzouz, and E. F. El-Saadany, "Distance protection of lines connected to induction generator-based wind farms during balanced faults," *IEEE Trans. Sustain. Energy*, vol. 5, no. 4, pp. 1193–1203, Oct. 2014.

[21] D. F. Howard, T. G. Habetler, and R. G. Harley, "Improved sequence network model of wind turbine generators for short-circuit studies," *IEEE Trans. Energy Convers.*, vol. 27, no. 4, pp. 968–977, Dec. 2012.

[22] F. Sulla, J. Svensson, and O. Samuelsson, "Symmetrical and unsymmetrical short-circuit current of squirrel-cage and doubly-fed induction generators," *Electr. Pow. Syst. Res.*, vol. 81, no. 7, pp. 1610 – 1618, Jul. 2011.

[23] G. Pannell, D. J. Atkinson, and B. Zahawi, "Analytical study of grid-fault response of wind turbine doubly fed induction generator," *IEEE Trans. Energy Convers.*, vol. 25, no. 4, pp. 1081–1091, Dec. 2010.

[24] J. Morren and S. W. H. de Haan, "Short-circuit current of wind turbines with doubly fed induction generator," *IEEE Trans. Energy Convers.*, vol. 22, no. 1, pp. 174–180, March 2007.

[25] M. Liu, W. Pan, R. Quan, H. Li, T. Liu, and G. Yang, "A short-circuit calculation method for DFIG-based wind farms," *IEEE Access*, vol. 6, pp. 52 793–52 800, Oct. 2018.

[26] D. Zhou, F. Blaabjerg, M. Lau, and M. Tønnes, "Optimized reactive power flow of DFIG power converters for better reliability performance considering grid codes," *IEEE Trans. Ind. Electron.*, vol. 62, no. 3, pp. 1552–1562, March 2015.

[27] S. E. da Silveira, B. J. C. Filho, and S. M. Silva, "Fault ride-through enhancement in DFIG with control of stator flux using minimised series voltage compensator," *IET Renew. Power Gen.*, vol. 12, no. 1, pp. 1234–1240(6), Aug. 2018.

[28] Y. Shen, M. Cui, Q. Wang, F. Shen, B. Zhang, and L. Liang, "Comprehensive reactive power support of dfig adapted to different depth of voltage sags," *Energies*, vol. 10, no. 6, 2017. [Online]. Available: https://www.mdpi.com/1996-1073/10/6/808

[29] S. Ghosh, Y. J. Isbeih, R. Bhattarai, M. S. E. Moursi, E. F. El-Saadany, and S. Kamalasadan, "A dynamic coordination control architecture for reactive power capability enhancement of the dfig-based wind power generation," *IEEE Trans. Power Syst.*, vol. 35, no. 4, pp. 3051–3064, 2020.

[30] ——, "Study of fault current characteristics of the dfig considering dynamic response of the rsc," *IEEE Trans. Power Syst.*, vol. 35, no. 4, pp. 3051–3064, June 2020.

[31] X. M. H, Xu and S. D, "Reactive current assignment and control for DFIG based wind turbines during grid voltage sag and swell conditions," *Journal of Power Electronics*, vol. 15, no. 1, p. 235–245, Jan 2015.

[32] H. Xu, Y. Zhang, Z. Li, R. Zhao, and J. Hu, "Reactive current constraints and coordinated control of dfig's rsc and gsc during asymmetric grid condition," *IEEE Access*, vol. 8, pp. 184 339–184 349, Oct. 2020.

[33] Y. Chang, I. Kocar, J. Hu, U. Karaagac, K. W. Chan, and J. Mahseredjian, "Coordinated control of dfig converters to comply with reactive current requirements in emerging grid codes," *J. Mod. Power Syst. Clean Energy*, pp. 1–12, Oct. 2021.

[34] M. Nagpal and C. Henville, "Impact of power-electronic sources on transmission line ground fault protection," *IEEE Trans. Power Del.*, vol. 33, no. 1, pp. 62–70, Feb. 2018.

[35] A. Haddadi, M. Zhao, I. Kocar, U. Karaagac, K. W. Chan, and E. Farantatos, "Impact of inverter-based resources on negative sequence quantities-based protection elements," *IEEE Trans. Power Del.*, pp. 1–1, March 2020, In press.

[36] A. Hooshyar *et al.*, "Fault type classification in microgrids including photovoltaic DGs," *IEEE Trans. Smart Grid*, vol. 7, no. 5, pp. 2218–2229, July 2016.

[37] G. Song, C. Wang, T. Wang, M. Kheshti, and X. Kang, "A phase selection method for wind power integration system using phase voltage waveform correlation," *IEEE Trans. Power Del.*, vol. 32, no. 2, pp. 740–748, April 2017.

[38] J. Zhang, B. Zhang, and C. Wang, "Improved schemes for traditional current-based phase selectors in wind power systems," *IET Gen., Trans. Dis.*, vol. 12, no. 21, pp. 5781–5788, Sep. 2018.

[39] K. Xu, Z. Zhang, Q. Lai, and X. Yin, "Fault phase selection method applied to tie line of renewable energy power stations," *IET Gen., Trans. Dis.*, vol. 14, no. 13, pp. 2549–2557, Sep. 2020.

[40] A. K. Pradhan and G. Joos, "Adaptive distance relay setting for lines connecting wind farms," *IEEE Trans. Energy Convers.*, vol. 22, no. 1, pp. 206–213, March 2007.

[41] S. Chen, N. Tai, C. Fan, J. Liu, and S. Hong, "Adaptive distance protection for grounded fault of lines connected with doubly-fed induction generators," *IET Renew. Power Gen.*, vol. 11, no. 6, pp. 1513–1520, May 2017.

[42] J. Lopez, P. Sanchis, X. Roboam, and L. Marroyo, "Dynamic behavior of the doubly fed induction generator during three-phase voltage dips," *IEEE Trans. Energy Convers.*, vol. 22, no. 3, pp. 709–717, Aug. 2007.

[43] D. Xiang, L. Ran, P. J. Tavner, and S. Yang, "Control of a doubly fed induction generator in a wind turbine during grid fault ride-through," *IEEE Trans. Energy Convers.*, vol. 21, no. 3, pp. 652–662, Sept. 2006.

[44] H. Geng, C. Liu, and G. Yang, "LVRT capability of DFIG-based WECS under asymmetrical grid fault condition," *IEEE Trans. Ind. Electron.*, vol. 60, no. 6, pp. 2495–2509, June 2013.

[45] R. Pena, J. C. Clare, and G. M. Asher, "Doubly fed induction generator using back-to-back PWM converters and its application to variable-speed wind-energy generation," *IEE Proceedings Elec. Power Appl.*, vol. 143, no. 3, pp. 231–241, May 1996.

[46] B. Wu, Y. Lang, N. Zargari, and S. Kouro, *Power Conversion and Control of Wind Energy Systems*. Wiley-IEEE Press, 2011. [Online]. Available: https://ieeexplore.ieee.org/servlet/opac?bknumber=6047595

[47] G. Abad, J. Lopez, M. Rodriguez, L. Marroyo, and G. Iwanski, *Doubly Fed Induction Machine: Modeling and Control for Wind Energy Generation Applications*. Wiley-IEEE Press, 2011, ch. Analysis of the DFIM Under Voltage Dips, pp. 276–363.

[48] L. Xu, "Enhanced control and operation of DFIG-based wind farms during network unbalance," *IEEE Trans. Energy Convers.*, vol. 23, no. 4, pp. 1073–1081, Dec. 2008.

[49] A. Leon, J. Mauricio, and J. Solsona, "Fault ride-through enhancement of DFIG-based wind generation considering unbalanced and distorted conditions," *IEEE Trans. Energy Convers.*, vol. 27, no. 3, pp. 775–783, Sep. 2012.

[50] L. Xu, "Coordinated control of DFIG's rotor and grid side converters during network unbalance," vol. 23, no. 3, pp. 1041–1049, May 2008.

[51] S. Engelhardt, J. Kretschmann, J. Fortmann, F. Shewarega, I. Erlich, and T. Neumann, "Capability and limitations of dfig based wind turbines concerning negative sequence control," in *2013 IEEE Power Energy Society General Meeting*, Nov. 2013, pp. 1–5.

[52] P. Cheng and H. Nian, "Collaborative control of DFIG system during network unbalance using reduced-order generalized integrators," *IEEE Trans. Energy Convers.*, vol. 30, no. 2, pp. 453–464, June 2015.

[53] L. Chen, B. Zhang, and X. Fan, "Asymmetrical fault ride-through control strategy for rotor-side converter of DFIG," *IEEE Trans. Energy Convers.*, vol. 35, no. 2, pp. 1046–1053, June 2020.

[54] I. Erlich, J. Kretschmann, J. Fortmann, S. Mueller-Engelhardt, and H. Wrede, "Modeling of wind turbines based on doubly-fed induction generators for power system stability studies," *IEEE Trans. Power Syst.*, vol. 22, no. 3, pp. 909–919, July 2007.

[55] V. Akhmatov, *Induction Generators for Wind Power*. UK: Multi-Science Publishing, 2007.

[56] *The Grid Code*, National Grid, March 2022. [Online]. Available: https://www.nationalgrideso.com/document/162271/download

[57] *Power Systems Test Case Archive*, [Online]. Available: http://labs.ece.uw.edu/pstca/.

[58] *Instruction Manual: SEL-421-4, -5 Relay, Protection, Automation, and Control System*, SEL, USA, Dec. 2021. [Online]. Available: https://selinc.com/products/421/

[59] X. Kong, Z. Zhang, X. Yin, and M. Wen, "Study of fault current characteristics of the DFIG considering dynamic response of the RSC," *IEEE Trans. Energy Convers.*, vol. 29, no. 2, pp. 278–287, June 2014.

[60] S. Engelhardt, *Direkte Leistungsregelung einer Windenergieanlage mit doppelt gespeister Asynchronmaschine ("Direct Power Control of DFIG-Based Wind Turbines")*. Dissertation Universität Duisburg-Essen, Germany, 2010.

[61] D. F. Howard, *Short-circuit current in wind-turbines generator networks*. Dissertation Georgia Institute of Technology, Dec. 2013.

[62] M. I. Martinez, G. Tapia, A. Susperregui, and H. Camblong, "Dfig power generation capability and feasibility regions under unbalanced grid voltage conditions," *IEEE Trans. Energy Convers.*, vol. 26, no. 4, pp. 1051–1062, Oct. 2011.

[63] C. Feltes, *Advanced Fault Ride Through Control of DFIG Based Wind Turbines Including Grid Connection Via VSC-HVDC*, ser. Berichte aus der Energietechnik. Shaker, 2012.

[64] S. Engelhardt, H. Wrede, and A. Geniusz, "Method of and apparatus for compensation of oscillation effects in the event of mains asymmetry in a double-fed asynchronous machine," U.S. Patent 8 415 818, April 9, 2013.

[65] S. Engelhardt *et al.*, "Negative sequence control of DFIG based wind turbines," in *2011 IEEE Power and Energy Soc. Gen. Meeting*, Oct. 2011.

[66] O. Gomis-Bellmunt *et al.*, "Ride-through control of a doubly fed induction generator under unbalanced voltage sags," *IEEE Trans. Energy Convers.*, vol. 23, no. 4, pp. 1036–1045, Sep. 2008.

[67] J. Lopez, E. Gubia, E. Olea, J. Ruiz, and L. Marroyo, "Ride through of wind turbines with doubly fed induction generator under symmetrical voltage dips," *IEEE Trans. Ind. Electron.*, vol. 56, no. 10, pp. 4246–4254, Oct. 2009.

[68] J. H. Teng, R. C. Leou, C. Y. Chang, and S. Y. Chan, "Harmonic current predictors for wind turbines," *Energies*, vol. 6, no. 3, pp. 1314–1328, Mar. 2013.

[69] S. Xiao, G. Yang, H. Zhou, and H. Geng, "An LVRT control strategy based on flux linkage tracking for DFIG-based WECS," *IEEE Trans. Ind. Electron.*, vol. 60, no. 7, pp. 4246–4254, Oct. 2013.

[70] A. Banaiemoqadam, A. Hooshyar, and M. A. Azzouz, "A control-based solution for distance protection of lines connected to converter-interfaced sources during asymmetrical faults," *IEEE Trans. Power Del.*, vol. 35, no. 3, pp. 1–1, June 2019.

[71] *Manual: SIPROTEC 5, Distance and Line Differential Protection, Breaker Management for 1-Pole and 3-Pole Tripping, 7SA87, 7SD87, 7SL87, 7VK87-V8.01 and higher*, Siemens, Germany, May 2019. [Online]. Available: https://support.industry.siemens.com/cs/document/109742440/siprotec-5-7sa87-7sd87-7sl87-7vk87-lineprot-1-3-pol-manual?dti=0&pnid=25296&lc=en-WW

[72] *IEEE 9 Bus Systems*. Illinois Center for a Smarter Electric Grid, Aug. 2014, [Online]. Available: https://icseg.iti.illinois.edu/wscc-9-bus-system/.

[73] V. Caliskan, D. J. Perreault, T. M. Jahns, and J. G. Kassakian, "Analysis of three-phase rectifiers with constant-voltage loads," *IEEE Trans. Circuits Syst. I*, vol. 50, no. 9, pp. 1220–1225, Sept. 2003.

[74] Bin He and Minggao Yang, "Robust LPV control of diesel auxiliary power unit for series hybrid electric vehicles," *IEEE Trans. Power Electron.*, vol. 21, no. 3, pp. 791–798, May 2006.

[75] B. Boashash, "Estimating and interpreting the instantaneous frequency of a signal. i. fundamentals," *Proceedings of the IEEE*, vol. 80, no. 4, pp. 520–538, April 1992.

[76] A. Testa *et al.*, "Interharmonics: Theory and modeling," *IEEE Trans. Power Del.*, vol. 22, no. 4, pp. 2335–2348, Oct. 2007.

[77] D. Costello and K. Zimmerman, "Frequency tracking fundamentals, challenges, and solutions," in *68th Annu. Conf. for Protective Relay Eng.*, Apr. 2011, pp. 203–214.

[78] D. F. Howard, T. M. Smith, M. Starke, and R. G. Harley, "Short circuit analysis of induction machines - wind power application," in *2012 IEEE Transmission and Distribution Conference and Exposition*, Orlando, FL, USA, May 2012, pp. 1–8.

[79] A. Hooshyar, M. A. Azzouz, and E. F. El-Saadany, "Distance protection of lines emanating from full-scale converter-interfaced renewable energy power plants–Part II: Solution description and evaluation," *IEEE Trans. Power Del.*, vol. 30, no. 4, pp. 1781–1791, Aug. 2015.